The University Of Sheffield.

Observation of Crystal Formation of Halide Perovskite Thin Films by Wide Angle X-ray Scattering

By:

Noura Eid Alhazmi

A thesis submitted in partial fulfilment of the requirements for the degree of Doctor of Philosophy

The University of Sheffield
Faculty of Engineering
Electronic and Electrical Engineering

August -2018

Acknowledgements

Primarily, I would like to express a considerable gratitude and appreciation to my supervisor Dr Alan Dunbar for giving me the opportunity to undertake this work and all his constructive comments, time and patience. Then I would like to thank Professor Geraint Jewell for his encouragements and support. Thank also goes to all the academic and technical staff in University of Sheffield who didn't hesitate to help me with this project.

The PhD project can't be completed without accesses and the support from the Diamond Light Centre to perform the WAXS experiments. Therefore, their helps and support are appreciated.

I thank my research group including Edwin Pineda De La O, Konstantinos Tsevas, Gabriel E Perez, Francesco Bastianini and Hatice Burak. Furthermore, all my friends from Electronic and Electrical Engineering and the Physics departments deserve my appreciation.

My deep thanks to my beloved husband Dr Anas Alhazmi, awesome sons Malik and Mutaz, lovely daughter Lara for all their patience and support and motivations. Thank also goes to Dr Khaled and his wife for all his advice and assistance. Finally and significantly, I will not forget to thank all my brothers and sisters for their encouragements and help.

Abstract

The perovskite solar cell received much attention due to its high power conversion efficiency (PCE), and its easy and low cost fabrication process when compared to other solar cell devices. However, the device was not commercialized because of perovskite materials limitations related to fast decomposition in air, sensitivity to humidity, and concerns about toxicity of the lead. Therefore, understanding the dynamics of perovskite film forming for different material compositions will assist in overcoming these perovskite materials limitations. This is the main aim of this thesis.

In situ spin coating wide angle X-ray scattering (WAXS) was not only used to investigate $MAPbI_{3-x}Cl_x$ films that were commonly applied, but the different crystallization stages of different perovskite material compositions were also studied in this project. We observed the faster crystallization of the intermediate product $MA_{x+y}PbI_{2+x}Cl_y$ after 2 minutes of processing time.

On the other hand, slower crystallization of intermediate products was observed in $FAPbI_{3-x}Cl_x$ film formation compared to $MAPbI_{3-x}Cl_x$. Noticeably, the most important finding related to $FAPbI_{3-x}Cl_x$ perovskite film is the early forming stage of perovskite phase before annealing.

The WAXS investigation of lead free perovskite groups based on bismuth indicated the fast crystallization of $MA_3Bi_2I_9$, $MA_3Bi_2I_9Cl_X$ and $FA_3Bi_2I_9$ materials during spin coating. However, the surface coverage and optical band gap measurement of $FA_3Bi_2I_9$ films placed it in the best candidate among other lead free materials.

Abbreviation

E_{hv}	Energy of the photon
E_g	Energy of band gap
VB	Valence Band
CB	Conduction Band
PCE	Power Conversion Efficiency
NREL	National Renewable Energy Laboratory
WAXS	Wide angle X ray Scattering
GI-WAXS	Grazing Incidence Wide Angle X-ray Scattering
T-WAXS	Transmission Wide Angle X-ray Scattering
XRD	X-ray Diffraction
SEM	Scanning Electron Microscopy
UV-Vis	Ultraviolet-Visible
MA	Methylamine
FA	Formamidine
MAI	Methylammonium Iodide
FAI	Formamidinium Iodide
DMF	Dimethylformamide
$PbCl_2$	Lead chloride

Contents

Chapter1: Introduction

The thesis objectives are introduced in this chapter in **Section1.1**. A brief discussion of the development of the perovskite solar cell is presented in **Section1.2**. Clarification of some requirements for the photovoltaic materials is given in **Section1.3.**

1.1 Research Objective

With high expectations that nearly a third of the world's electricity will be generated by photovoltaic technology from now to 2030, this technology is becoming a crucial subject of research [1, 2]. Photovoltaic technology is defined as a technology that converts solar energy into electricity and has been in development for over three generations.

The first generation of solar cells mainly based on silicon (Si) wafers dominates the solar cells market [3, 4]. The maximum efficiency of crystalline Si solar cell was 27% (as reported by National Renewable Energy Laboratory (NREL)[5].

The second generation is defined as thin films solar cells that made of n-p type semiconductors including, cadmium telluride (CdTe), and gallium arsenide (GaAs) [6, 7]. This technology recorded the best efficiency among other solar cells types as presented in purple groups including the single solar cell and multi-junction solar cells in **Fig1.1**[6]. However, the thin film solar cell technology requires advanced fabrication processes. These limitations lead to the emergence of the third generation technology that is defined as the thin film solar cell based on a solution process[7].

Presently, particular interest in the photovoltaic research focuses on this third generation solar cells. The third generation solar cell devices are organic photovoltaic, dye sensitized solar cells that are made from organics and organometal halide perovskite [3, 4]. In comparison to organic photovoltaic and dye sensitized solar cells, hybrid perovskite solar cells produce higher efficiency with values more than 20% during a period of less than 10 years reporting in the literature and based on **Fig1.1** [1, 8, 5]. Despite the higher efficiency of perovskite solar cells and the fast improvement compared to the other type of solar cells, the solar cell market progress is limited by perovskite material issues including fast decomposition and high toxicity.

In this thesis, the main aim is to understand the hybrid perovskite better in order to overcome these perovskite solar cells market limitations.

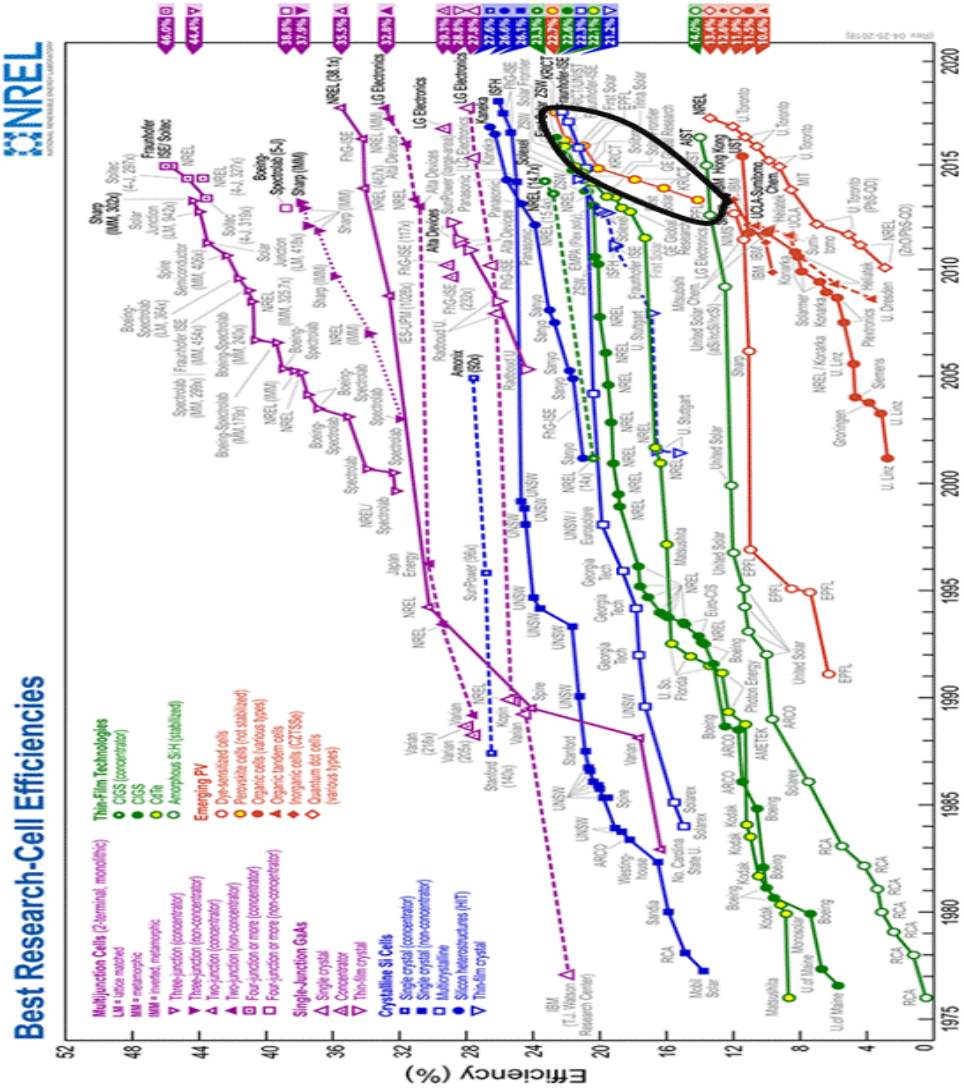

Figure1. 1: Power conversion efficiency of all solar cells based on inorganic and organic materials as a function of the timeline from year 1975 to 2017, the circled data points highlight the rapid growth in efficiency of the perovskite solar cells [5].

1.2 Perovskite Solar Cells

Most of the published reports regarding perovskite solar cells utilize the perovskite materials $MAPbI_3$ or $MAPbI_{3-x}Cl_x$ as absorber materials as shown in **Fig1.2**[9]. However, their large scale production may be limited by the toxicity of lead (Pb) as well as material degradation that limits the lifetime of solar cells, [9]. Therefore, further

investigation to find new perovskite materials is vital to overcome these limitations and improve the efficiency of perovskite solar cells for use in a wide range of industries. The different new components of perovskite need to be sufficiently understood and carefully characterized during the film formation process before use in solar cell devices. The dynamics of the crystallization stages during film forming is one of the important aspects of perovskite films crystallization. The efficiency of the perovskite solar cell can be further increased by forming high quality crystalline films [10]. Therefore, the particular aim of this project is to understand the crystallization stages of perovskite as these stages occur during the film formation.

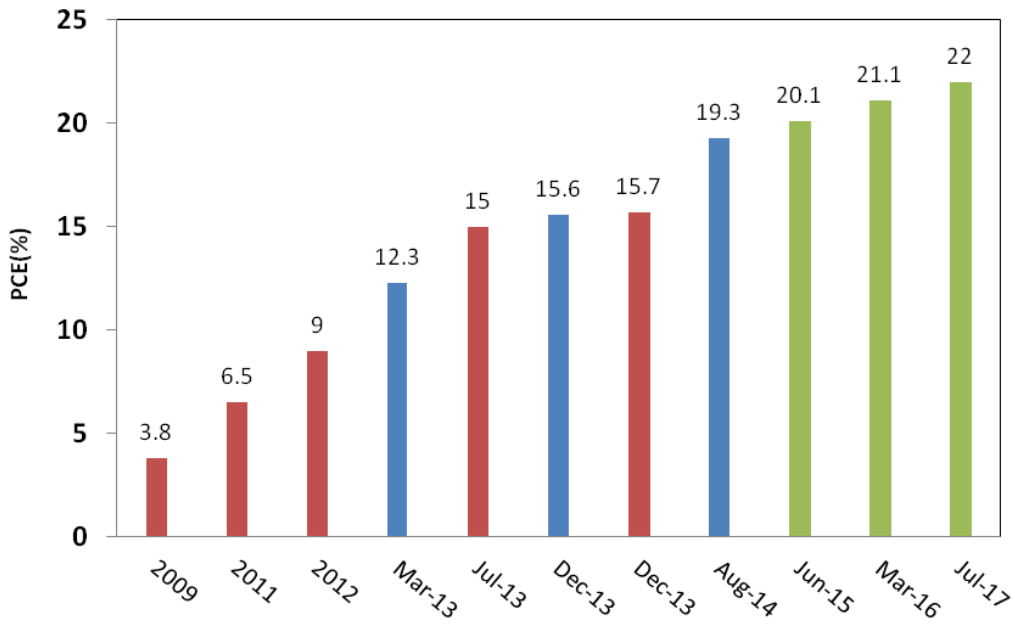

Figure1.2: Power Conversion Efficiency (PCE) of perovskite solar cells as a function of the timeline as reported in [9]. Red bar =$MAPbI_3$, Blue bar =$MAPbI_{3-x}Cl_x$ and Green bar=mixed perovskite.

1.3 Requirements of Photovoltaic Materials

To operate the solar cells, a photon of must be absorbed by an absorber layer. Then, the generated carriers are transported and separated to extract free electrons out of the solar cell into the external circuit [4].

The energy of the absorbed photon and the band gap of the semiconductor should be considered. In the case of the energy of the photon E_{hv} equal to the energy of the band gap E_g of the absorber materials, the electron can be promoted from the valence band (VB) to the conduction band (CB). If the value of $E_{hv} < E_g$, the electron will not gain the sufficient energy to be promoted to the conduction band, and thus, the exciton of an electron-hole pair will not occur. On the other hand, photons with energy more than the band gap energy can give electrons extra energy exciting them above the conduction band edge. These excited electrons then undergo electron relaxation (thermalization) to the edge of the conduction band. Therefore, the energy of the band gap of the photovoltaic materials should be carefully selected to absorb the photon energies within a solar light and then form free carriers that generate electricity.

In organometal halide perovskite, the binding energy of the exciton is low in the range of 20-50meV comparable to thermal energy (25meV at room temperature) [11, 12]. Therefore, this binding energy facilitates breaking the exciton into free carriers.

The correlation between the energy of the band gap of photovoltaic materials and PCE of solar cells was studied, and is shown by Shockley-Queisser (SQ) limit. It can be observed from the SQ limit that maximum power conversion more than 25% of the solar light can

be obtained by semiconductors having band gap 1.4eV such as GaAs[12] [13]. Perovskite having band gap between1.5 to 1.7 eV can yield around 20% PCE.

Another preferable point in favour of GaAs is the direct band gap that increased the ability to absorb solar light.

Fig1.3 illustrates the difference between the direct and indirect band gap. In the direct band gap, the energy of the photon is sufficient enough to promote an electron into the conduction band whereas in indirect band gap materials, an electron requires the momentum of the phonon to move it into the conduction band, and which also reduces absorption effects.

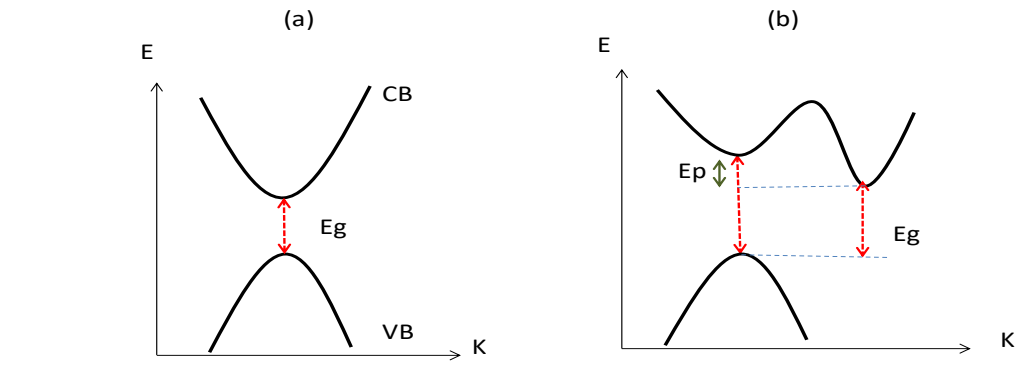

Figure1.3: The band structure of semiconductors illustrates (a) the direct band gap, (b) the indirect band gap.

After light absorption and free carrier formation, the generated carrier should be separated and then collected by the cathode and anode in the external circuit to produce a photocurrent[14]. Carrier separation and transport requires materials with long diffusion length.

In perovskite materials, the diffusion length of the carriers in the active layer (the absorber material) is defined as the distance that carriers (free electron) can diffuse before scattering, becoming trapped or relaxing back to the VB.

Therefore, it must be long to prevent any chance of recombination between the electrons and holes before arriving to the cathode and anode, respectively. In halide perovskite, a long diffusion length was observed at~100nm for lead iodide perovskites whereas in mixed lead chloride halide perovskite it is even longer at ~1μm [15, 16]. In contrast, in the organic semiconductor materials this value is in the range of only 20 nm, limiting the efficiency of the organic solar cells[16].

In solution processed solar cells, it is important to ensure that good surface coverage with the photovoltaic material is achieved. In this thesis, we will study how the surface coverage of perovskite films can be varied based on the thermal annealing conditions.

A brief background of the origin of the perovskite materials and their related attractive properties is presented in **Chapter 2.** Details of the sample preparation and experimental steps are discussed in **Chapter 3.** The conventional material $MAPbI_{3-x}Cl_x$ is characterized in **Chapter 4**, and **Chapter 5** focuses on analysis and characterization of $FAPbI_{3-x}Cl_x$. Lead free materials incorporating MA and FA cations mixed with BiI_3 and $BiCl_3$ are studied in **Chapter 6.**

1.4 References

1. Green, M.A., A. Ho-Baillie, and H.J. Snaith, The emergence of perovskite solar cells. Nature Photonics, 2014. **8**(7): p. 506-514.

2. Turner, G., Global Renewable Energy Market Outlook 2013. Bloomberg New Energy Finance https://www.bnef.com/insightdownload/7526/pdf (11 April 2014 2013.

3. Green, M.A., Third generation photovoltaics: solar cells for 2020 and beyond. Physica E: Low-dimensional Systems and Nanostructures, 2002. **14**(1): p. 65-70.

4. Yan, J. and B.R. Saunders, Third-generation solar cells: a review and comparison of polymer: fullerene, hybrid polymer and perovskite solar cells. RSC Advances, 2014. **4**(82): p. 43286-43314.

5. NERL, https://www.nrel.gov/ncpv/images/efficiency_chart.jpg. 2017.

6. Green, M.A., K. Emery, Y. Hishikawa, W. Warta, and E.D. Dunlop, Solar cell efficiency tables (version 48). Progress in photovoltaics: research and applications, 2016. **24**(7): p. 905-913.

7. Kazim, S., M.K. Nazeeruddin, M. Grätzel, and S. Ahmad, Perovskite as light harvester: a game changer in photovoltaics. Angewandte Chemie International Edition, 2014. **53**(11): p. 2812-2824.

8. Luo, S. and W.A. Daoud, Recent progress in organic-inorganic halide perovskite solar cells: mechanisms and material design. Journal of Materials Chemistry A, 2015. **3**(17): p. 8992-9010.

9. Elumalai, N.K., M.A. Mahmud, D. Wang, and A. Uddin, Perovskite Solar Cells: Progress and Advancements. Energies, 2016. **9**(11): p. 861.

10. Barrows, A.T., S. Lilliu, A.J. Pearson, D. Babonneau, A.D. Dunbar, and D.G. Lidzey, Monitoring the Formation of a CH3NH3PbI3–xClx Perovskite during Thermal

Annealing Using X-Ray Scattering. Advanced Functional Materials, 2016. **26**(27): p. 4934-4942.

11. Niu, G., X. Guo, and L. Wang, Review of recent progress in chemical stability of perovskite solar cells. Journal of Materials Chemistry A, 2015. **3**(17): p. 8970-8980.

12. Polman, A., M. Knight, E.C. Garnett, B. Ehrler, and W.C. Sinke, Photovoltaic materials: Present efficiencies and future challenges. Science, 2016. **352**(6283).

13. Shockley, W. and H.J. Queisser, Detailed balance limit of efficiency of p-n junction solar cells. Journal of applied physics, 1961. **32**(3): p. 510-519.

14. Nelson, J., The physics of solar cells. 2003: World Scientific Publishing Company.

15. Stranks, S.D., G.E. Eperon, G. Grancini, C. Menelaou, M.J. Alcocer, T. Leijtens, L.M. Herz, A. Petrozza, and H.J. Snaith, Electron-hole diffusion lengths exceeding 1 micrometer in an organometal trihalide perovskite absorber. Science, 2013. **342**(6156): p. 341-344.

16. Xing, G., N. Mathews, S. Sun, S.S. Lim, Y.M. Lam, M. Grätzel, S. Mhaisalkar, and T.C. Sum, Long-range balanced electron-and hole-transport lengths in organic-inorganic CH3NH3PbI3. Science, 2013. **342**(6156): p. 344-347.

Chapter 2: Theory and Literature Review

This chapter presents a brief review of theoretical background and some relevant previous work that study organometal halide perovskite films. In **Section 2.1** the structure of origin of the organometal halide perovskite is discussed, whereas **Section 2.2** focuses more on the perovskite solar cell devices. Some perovskite film fabrication techniques are summarized in **Section 2.3.** The perovskite studies of band gap and studies related to WAXS are detailed in **Section 2.4** and finally, a brief discussion of the lead free materials related to perovskite is presented in **Section 2.5.**

2.1 Perovskite Structure

The name is referred to the Russian mineralogist Lev A. Perovskie who characterized the structure of perovskite materials [1, 2]. Perovskite is defined as the large family of crystalline materials with a similar cubic structure to calcium titanium oxide ($CaTiO_3$) that is generally expressed as ABX_3 [3, 4].

The A cation determines whether the perovskite is organic or inorganic. In organometal halide perovskite group, A is organic. The smaller size and non- spherical structure of organic A cation is crucial to form 3D symmetric perovskite [1, 5].

Halide perovskites with halogen anionic components (Fe, Br, Cl and I) have received more attention because of their more suitable band gap which generally does not exceed 2.5eV [6]. In contrast, the oxide perovskite categories with general chemical formula ABO_3 are described as transparent materials with wide band gap 3-5eV, wider than the solar spectrum [7-9].

The ideal cubic unit cell of the halide organic perovskite is depicted in **Fig 2.1.** The B component (of the ABX_3 structure) bonds to the six corners of X forming BX6 octahedra. Each octahedra then forms a corner of a cube where the A organic cation fills the gap between the four octahedrs to form a cubic structure [4, 6, 10].

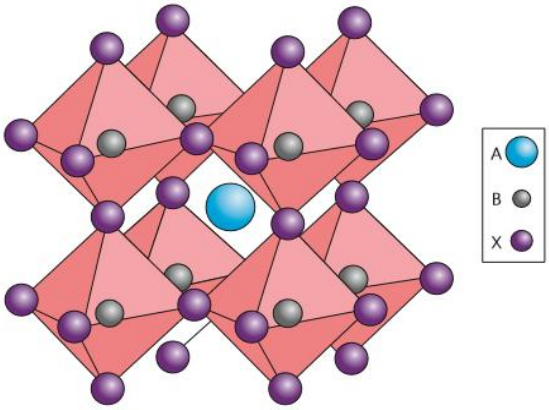

Figure2.1: The cubic symmetry of the organic-inorganic perovskite unit cell [11].

The size of each compound determines the ideal geometry of the unit cell of its organic halide perovskite. Tolerance (t) and octahedra (μ) factors define the correlation between the radii size of A, B and X and the geometry of the unit cell. The tolerance factor is defined based on the radii size of R_A, R_B and R_x, as can be seen in **Eq.2.1**, whereas the value of the octahedral factor is defined by the ratio of the radii size of the metal R_B and halide cation R_x, as shown in **Eq.2.2**[12].

A cubic structure that is crystallographically stable is formed if the tolerance value is in the range $0.81<t<1.11$ [11]. Values smaller than 0.81 form a structure with lower symmetry than the cubic structure such as tetragonal or orthorhombic structures [11]. A tolerance factor greater than 1.11 will destroy the 3D framework of the unit cell [1]. The

octahedra factor is related to the shape of the BX_6 octahedral. Preferable values of $0.44<\mu<0.90$ express the halide perovskite structure.

$$t = \frac{(R_A + R_B)}{[\sqrt{2}\,(R_B + R_x)]} \qquad \text{Eq2.1}$$

$$\mu = \frac{R_B}{R_X} \qquad \text{Eq2.2}$$

The tolerance and octahedra factors of some perovskite materials were calculated based on the radii size of A, B and X of perovskite materials in literature, see **Table 2.1** [1]. The study compares several perovskite materials based on four cations; cesium (Cs), methylammonium (MA), formamidinium (FA) and ethylammonium (EA) mixed with Pb and Sn as metal cations and I, Cl and Br as halide anions. In this thesis, the halide perovskites are discussed composed of MA and FA cations and Pb and Bi as metals where the halide anion I and I_xCl_{3-x}.

The larger A cation forms a structure closer (t) to the unit such as FA and EA, and a lower symmetry structure is more likely to be obtained by smaller cations MA and Cs as illustrated in **Fig 2.2**. A large cation A is most likely to result in a cubic structure. However, a high tolerance factor alone as it is the case for ethylammonium (EA) is still not a sufficient factor to be used widely in solar cells due to the wider band gap than the optimum range [13]. Solar cells based on EA perovskite materials produce a PCE of only 2.2%[14]. Therefore, the FA cation is more suitable than MA and EA to form a cubic perovskite.

Ions	Materials	R(nm)
A (Organic cation)	**MA**	**0.18**
	EA	**0.23**
	FA	**0.19~0.22**
B (Metal cation)	**Pb**	**0.119**
	Sn	**0.11**
X (Halogen anion)	**I**	**0.22**
	Cl	**0.196**
	Br	**0.18**

Table 2.1: The ionic radii size of the A, B and X as shown in [1] based on the values reported in [15-18].

In addition to the importance of selecting the suitable compounds during the synthesis of organic–halide perovskite to form a structural stability, there are several other factors can change the structure of the materials prepared from the same components. For example, $MAPbI_3$ exhibits a tetragonal structure at room temperature, but annealing the film at 100^oC can change the structure from tetragonal to cubic where the lower temperature causes opposite effect, see **Fig. 2.3** [19].

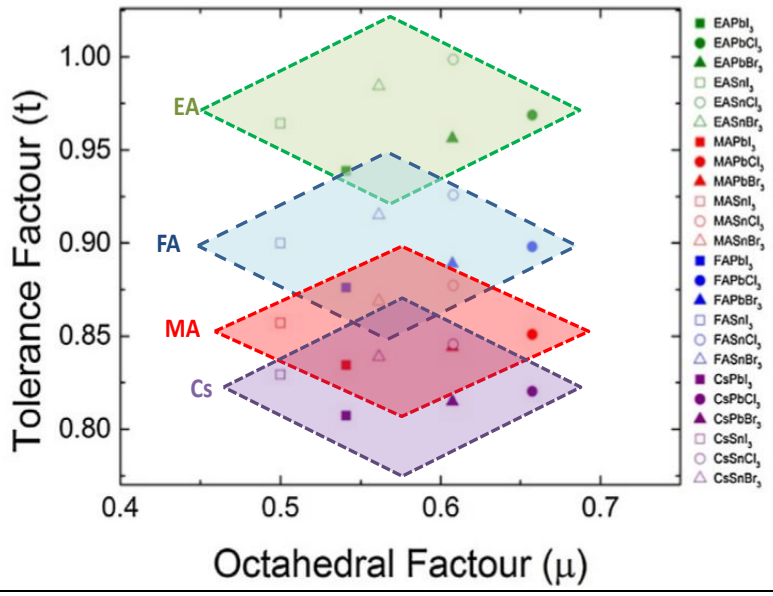

Figure 2.2:The calculated tolerance factor and octahedral factors for some organic –inorganic perovskite components [1].

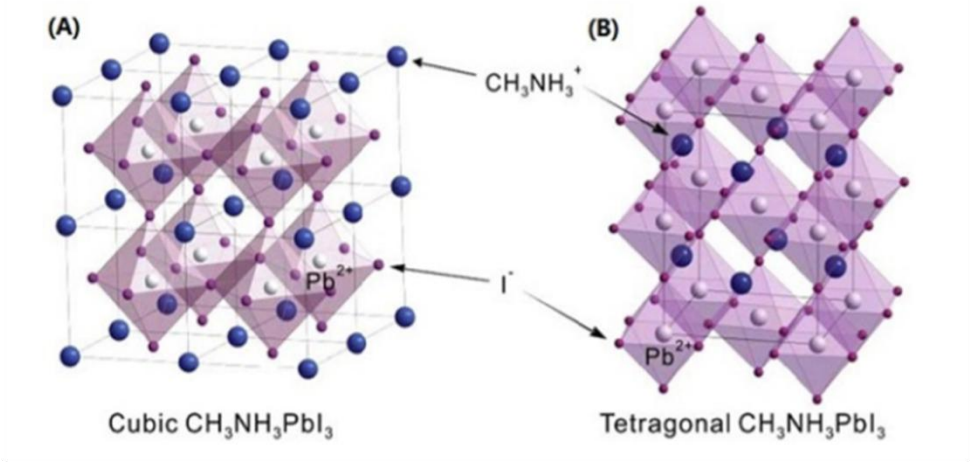

Figure 2.3: Crystal structure of $MAPbI_3$ that exhibits cubic and tetragonal symmetry as reported in[19].

2.2 Perovskite Solar Cell Devices

The first emergence of organic inorganic halide perovskite as a photovoltaic material was in a dye sensitized solar cells (DSSC) as a replacement of the organic dye and showed a

PCE of only 2.2% in 2006[20]. The same group (Kojima, A. and co-workers) in 2009 optimized the halogen in the halide organic perovskite materials by replacing iodine (I) with bromide (Br). This yielded an enhancement in the PCE from 2.2% to 3.8% due to the change in the band gap [17]. However, besides the low performance of DSSC perovskite solar cells, the main issue is the short life time, caused by dissolving the perovskite in the liquid electrolyte. In addition, further enhancement to perovskite solar cells was carried out in 2012 by replacing the liquid electrolyte with solid state hole transporting materials HTM, which caused an increase in PCE to 9.7% and improved the stability of the solar cell [21].

In 2013, a striking increase in PCE from 4.2% to 12.2% was recorded when the perovskite based on mixed halide perovskite was used as an absorber layer in planer heterjunction[22]. The main advantage of mixed halide perovskite is the longer diffusion length, which minimizes the risk of the electron-hole recombination. Another important contribution reported by the same group involved using a two evaporation source to deposit the perovskite layer, which provides higher film surface coverage, as detailed in the next section, and therefore higher PCE was recorded at 15.4%[23].

Using a DMSO solvent in perovskite preparation instead of the common solvent DMF led to further increases in the PCE to more than 16% in 2014 [24].

For the perovskite materials, mixing the organic cations FA and MA, caused preferable performance of the perovskite solar cell to reach 18.4% [25]. Similar research was carried out on mixed materials using $FAPbI_3$ and $MAPbBr_3$ perovskite materials, and the intermolecular exchanges method enhanced PCE to greater than 20%[26]. Several

optimisations were reported after that, resulting in very high performance of perovskite solar cell devices, with more than 21% efficiency recorded in 2016 [27].

Principle of the operation of perovskite solar cells varies from architecture to another; our discussion will be restricted to simple planar architecture. As with any solar cell, perovskite solar cells aim to convert sunlight into electrical energy. This can be achieved by light absorption, charge separation, and charge collection that are considered the three fundamental processes of the solar cell devices.

Under sunlight conditions, the light is absorbed by the perovskite layer. The thin flat layer of perovskite works as a light absorber and because of the low binding energy of the exciton (20-50meV), electron and hole separate immediately into free charges as was introduced in **Section 1.3** in **Chapter 1.**

Since the conduction band level in the electron transporting materials (ETM) is very close to the one in the perovskite layer (e.g $MAPbI_3$, -3.9eV), the electron will be injected into ETM.

The hole transporting the materials (HTM) had high hole mobility and the valence band matched with the valence band of the perovskite (e.g $MAPbI_3$, -5.5eV) to work to transport the hole collected by the anode.

Fig2.4 illustrates the structure of the perovskite solar cells and the band diagram where the materials were selected based on the band diagram

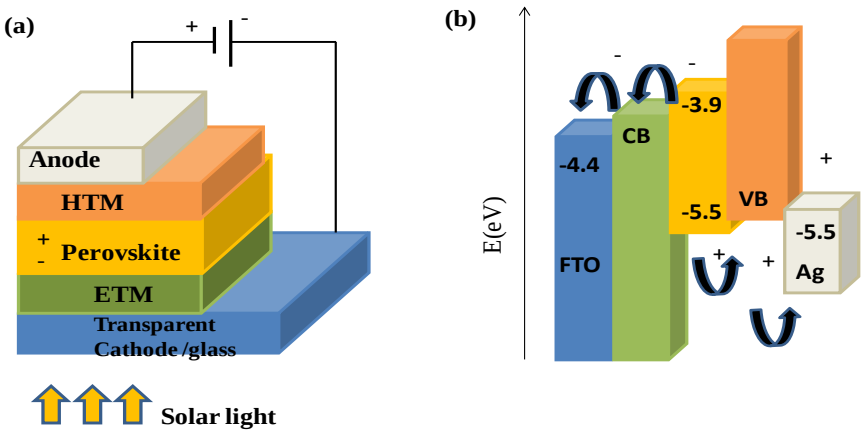

Figure 2.4: Architecture of a planar perovskite solar cells device **(a),** and **(b)** the band diagram of the same materials showing where electrons travel through the conduction band (CB) of the electron transporting materials and the holes travel via the valence band (VB) of the hole transporting materials, and charges may be collected by the selective contacts.

Despite the optimisation in the structure of the device and the layers of the carriers transporting materials, still the perovskite solar cell market progress of perovskite solar cells can be limited by perovskite material issues [11].

Main issues are the toxicity of the lead in perovskite and the fast degradation of perovskite that cause short solar cells lifetime. Therefore, material optimisation with complete understanding of perovskite film formation will be important aspects of the research related to the perovskite solar cells.

2.3 Fabrication processes of Perovskite Films

Perovskite films can be prepared by several methods. The most commonly used is spin coating [28, 29]. In a single step, a suitable solvent is used to prepare a well dissolved solution that contains A, B, and X. This can be prepared in one step, and then deposited onto a substrate as shown in **Fig 2.5 (a).** It can also be done in two steps where the

solution contains PbI_2 or $PbCl_2$ (solution 1) deposited first, then another solution containing MAI (solution 2) deposited next, followed by spin coating [13]. Dipping techniques were also reported where, after depositing the solution 1, the film was dipped into solution 2 to form the perovskite film, **Fig 2.5(b).**

Pinhole free perovskite films have been prepared with more advanced techniques such as vacuum deposition using dual sources where both MAI and PbI or PbICl are evaporated onto the substrate **Fig 2.5(c)** or, alternately, using a single source system where only MAI is evaporated onto a PbI layer **Fig. 2.5(d)**. The morphology of the perovskite films prepared by vapor deposition and the solution were researched, with the results shown in **Fig. 2.6**[30]

Although the techniques yield high morphology, it is difficult to apply for large-scale industrial needs, and the vacuum evaporation source is relatively expensive compared to spin coating [31].

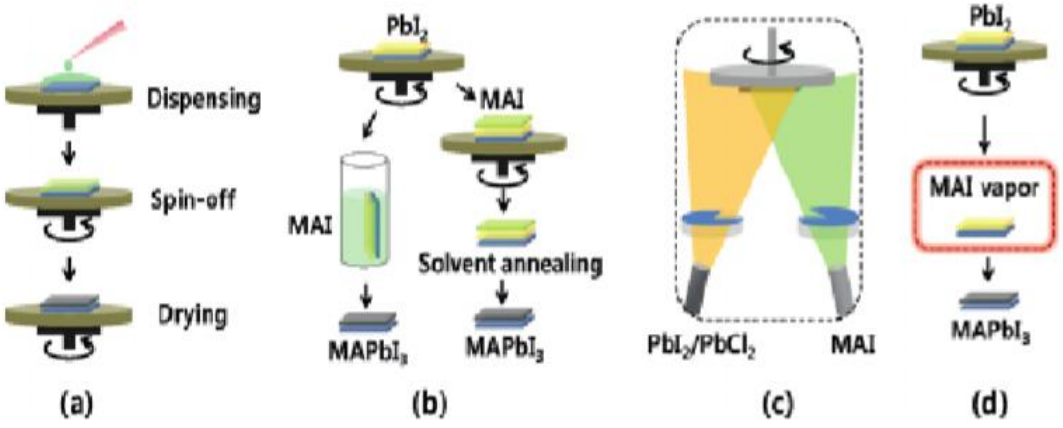

Figure 2.5: Several methods used to make perovskite films, including (a) spin coating single step (b) two steps and vacuum evaporation (c) with dual source, and (d) with single source[32]

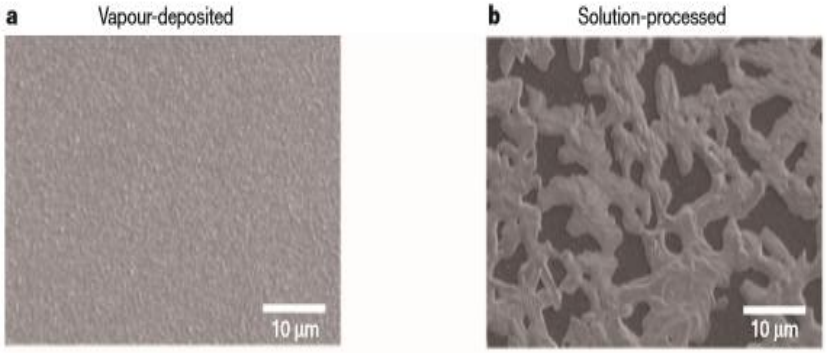

Figure 2.6: The surface of perovskite film prepared (a) by vapour deposition using dual source and (b) solution processes illustrated in [30].

2.4 The properties of the Perovskite layers

The discussion is restricted on band gap of the perovskite film and the high crystallization properties that influence on the performance of the solar cell device.

2.4.1 Bandgap of Perovskite

The band gap is formed between the conduction band formed by Pb 6p orbital and the valence band formed from Pb 6s–I 5p [33, 34]. The transition between the lower point of conduction band and the highest point of the valence band should, ideally, be a direct band gap with strong optical absorption[13], as is the case in GaAs (introduced in **Section 1.3)**.

Changing the halide anion from I to Br causes some alteration in the optical absorption spectra and diffusion length. It was observed, for example, that one could tune the optical band gap and absorption spectra of $MAPb(I_{1-x}Br_x)_3$ when the amount of Br changed as shown in **Fig. 2.7**[35].

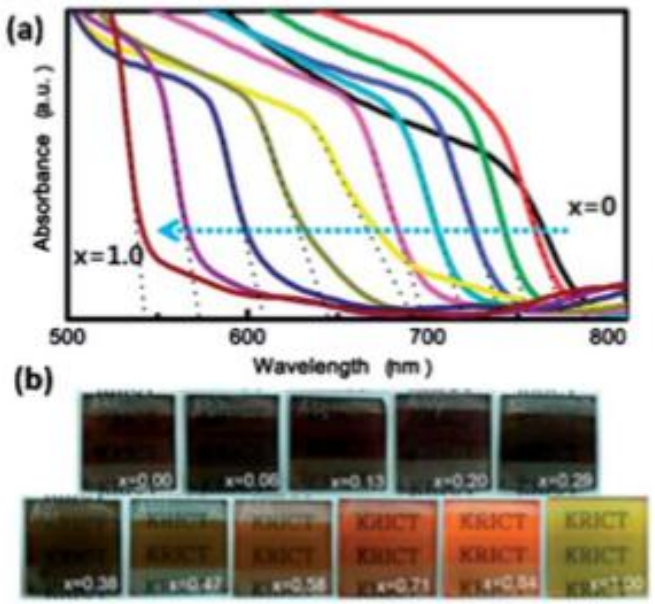

Figure 2.7: Optical absorption of $MAPb(I_{1-x}Br_x)_3$ films when x changes from 0 to 1in (a), and the photographs of the same films (b) [35].

2.4.2 Wide Angle X-ray Scattering (WAXS) of Perovskite Films

Previously Wide angle X-ray Scattering (WAXS) has been used to investigate different aspects of the perovskite films. Ex-situ WAXS with grazing incident angle was used in order to compare between the one-step and tow-step process solution of spin coating[36]. In one step solution, the lead salt and the organic cation dissolve together in one solution and deposit on the surface of the substrate whereas in the tow steps the lead and organic cation dissolved individually to deposit the mixture of the lead salt with solvent then at the next step, the solution of the organic cation with solvent. The experimental study concluded no significant difference was observed. However, the high crystallization of the perovskite film prepared by the two step process relies on the uniformity of the Pb layer that is formed first, as was detailed previously.

$MAPbI_{3-x}Cl_x$ perovskite solar cells were thermally annealed in situ to investigate the phase transition from the precursor phase into the perovskite phase and its degradation products [37, 38]. In both reports cited, annealing at 80°C for 120 minutes is defined as being sufficient to obtain the perovskite phase, while more than 2hr causes decomposition of the perovskite and at temperature lower than these conditions only the precursor phase to be formed. In one report, perovskite solar cells were made using a range of thermal annealing conditions and higher efficiency was obtained when the perovskite film was annealed for 120 min, (PCE12%) whereas only 7.8% PCE recorded from 80min annealing time [37]. This suggests that forming a good quality crystalline perovskite film is one of the essential criteria to obtaining the high solar cell efficiency. **Fig 2.8** shows the results of GI-WAXS and the morphology of perovskite films.

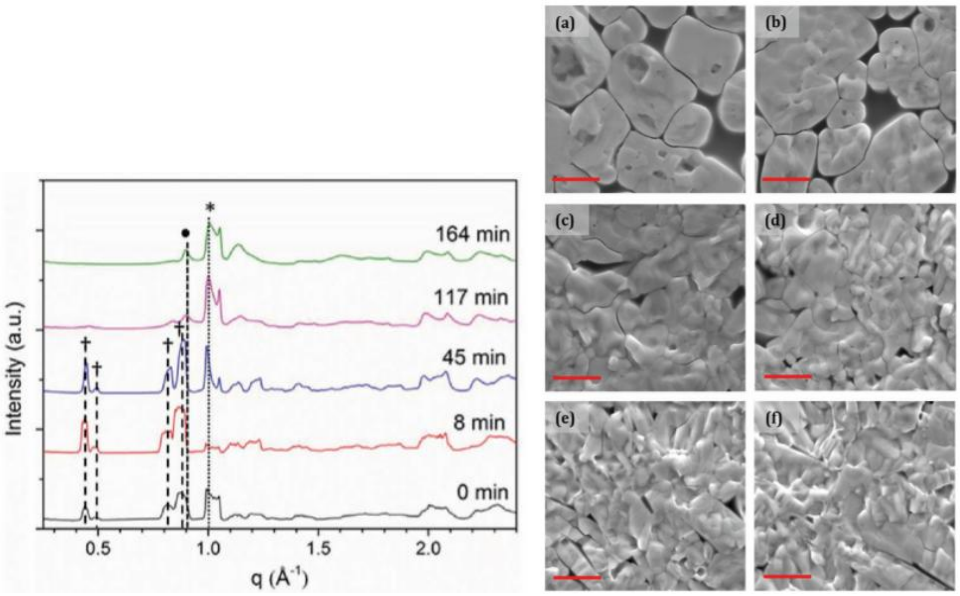

Figure 2.8 The result of the GI-WAXS of Scanning electron microscopy (SEM) images of films annealed for time periods, the surface of the films investigated by SEM a) 60min b) 80 min, c) 100 min, d) 120 min, e) 140 min, and f) 180 min where scale bars correspond to 1 μm as was reported in [37] .

The finding of this study are in agreement with a similar study which reported that MAI: $PbCl_3$ perovskite films have three crystallization dynamics stages[39]. The first stage observed is the precursor stage at the early thermal annealing after 5 min at 35 C. Only intermediate products formed at this stage. The perovskite phase formed after 100 min when the chemical reaction was complete. During the final stage decomposition of perovskite into lead salt was observed, and the intermediate phase, was recorded after 150min as illustrated in **Fig 2.9**.

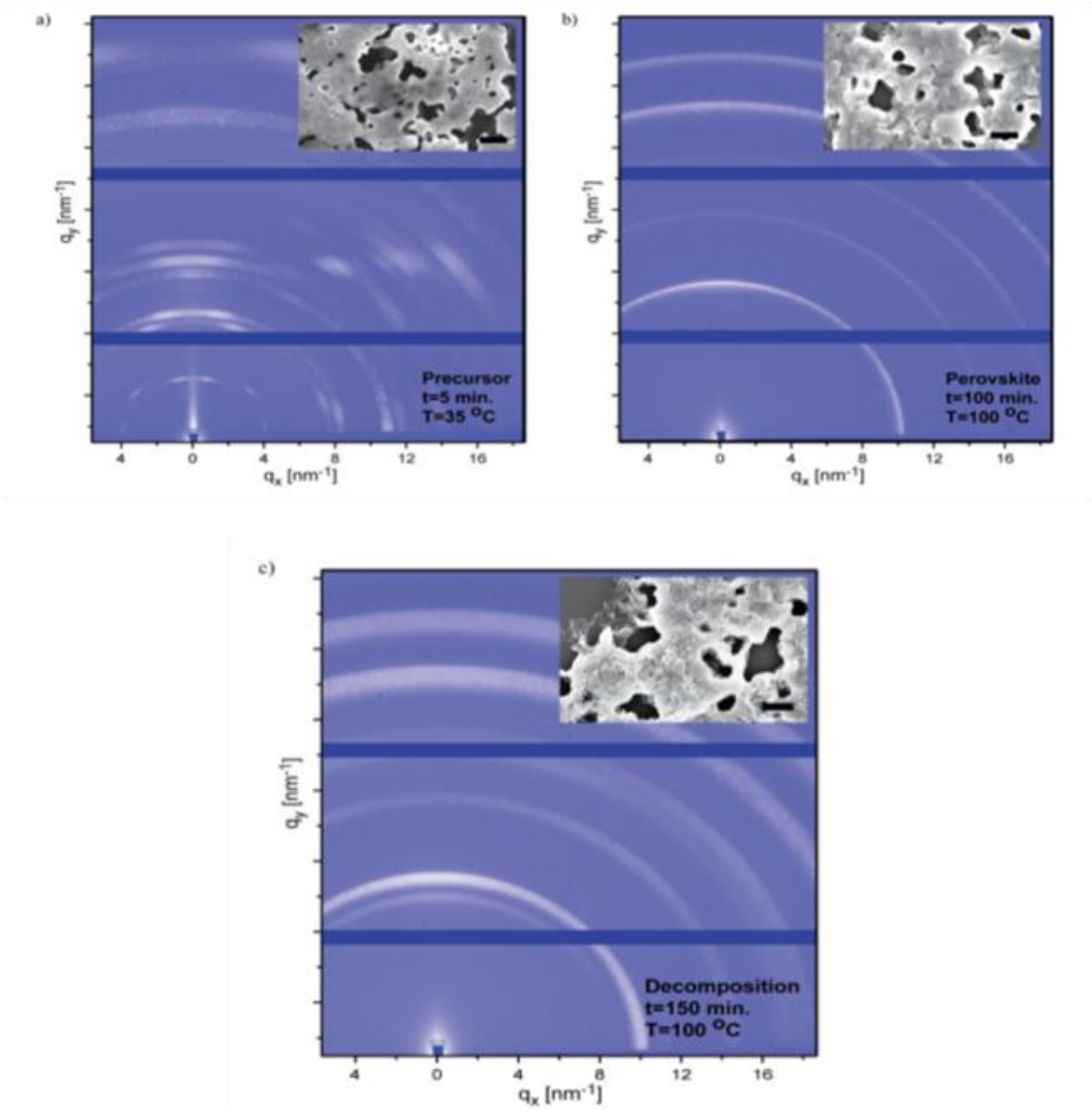

Figure 2.9: the three crystallization stages of the perovskite a) the precursor stage where the intermediate products are formed, b) the perovskite stage and c) the decomposition where the perovskite is decomposed into the lead salt and intermediate

However, the dynamic crystallization during spin coating of perovskite film has not yet been investigated and reported, which would further understanding of the crystal formation in perovskite films unclear at this stage.

2.5 Toxicity of lead and alternative materials to lead

The most common perovskite materials investigated in the literature includes Pb^{2+}, which yields very high PCEs exceeding 20%[40]. However, the mass production of such materials in the future may well be limited by the toxicity of the lead Pb^{2+} ion, which is highly soluble in water [41]. Therefore, it is important that a research solution to this issue is found. This could be achieved by suitable encapsulation and disposal at the end of life devices, but preferably further research in the organometal halide perovskite field will make it possible to replace it.

Bismuth (Bi) can be used to substitute Lead (Pb) due to its similar electronic configuration and better stability than Tin (Sn) that was also used [42, 43]. **Fig. 2.10 (a)** shows the colour of the different films of MBI films that were prepared from Bi and MAI and conventional films of $MAPbI_3$ during 26 days. The colour of the Bi-perovskite films was unchanged after 13 days and turned into the brighter colour film only after 26 days that indicates a high air stability as compared to the $MAPbI_3$, which changed from the dark brown to yellow after 13 days[44].

The XRD pattern of MBI films measured in the same study within 26 days is shown in **Fig 2.10(b)**[44]. A very slight change in the structure of the film was observed after 26 days as indicated by the structure stability in air and humidity condition 61%.

The optical absorption of Bi mixed with Cs materials (investigated over the course of 30 days in a different study) showed almost the same spectra, **Fig 2.10(e)** [45].

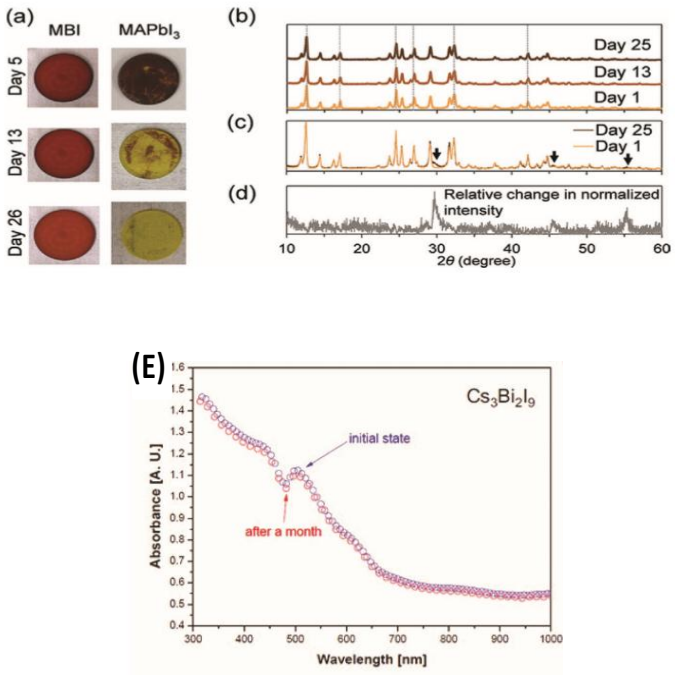

Figure 2.10: The crystal structure in XRD of MBI in (a-d) and colour of film in (c) as reported in [44] the optical absorption of BiI mixed with Cs materials in(e) [45].

The chemical structure of Bi halide perovskite is quite different than the ideal halide perovskite structure ABX_3. In the organometal halide perovskite a metal halide BX_6 layer is formed as octahedral and A cation fills the space in the middle of cubic of formed from octahedral shape. Replacing Pb^{2+} to Bi^{3+} causes the change in the B-X bond and metal halide octahedral PbI_6 can be replaced by Bi-octahedral $(Bi_2\ I_9)^{-3}$surronding by the A cation as illustrated in **Fig. 2.11**[46, 43].

The progress of Bi perovskite solar cell still materials is not at a competitive level with the halide lead perovskite solar cells, where the maximum efficiency reported is 2.15% PCE [43].Therefore, this part of the study still needs further research and understanding before the materials can help modify the perovskite solar cell efficiency.

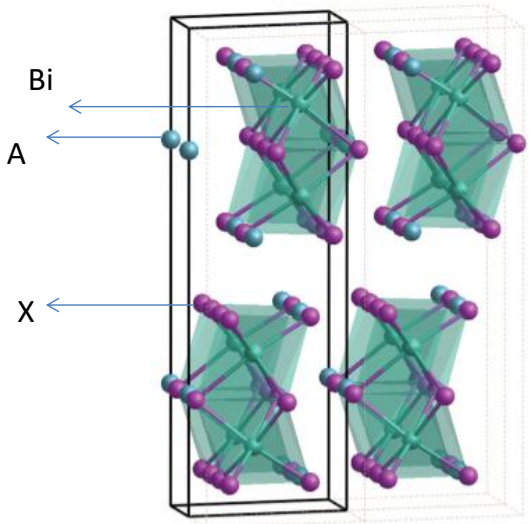

Figure 2.11: Structure of $A_3Bi_2X_9$ as reported in [43].

In summary, the chapter includes brief relative research work related to perovskite materials, which can be instructive in highlighting some points. The preferable structure of the cubic organometal halide perovskite is related to the size of the A, B and X and FA cation can be considered as a more suitable candidate than MA and EA.

The performance of the perovskite solar cell can be further enhanced by using a highly pure crystallised perovskite film as the absorber layer. This was shown by assessment after in situ thermal annealing; however, in situ WAXS of spin coating has not yet been investigated for comparison. Therefore, the current project will focus on in situ WAXS analysis of spin coated perovskite films.

The final discussed point is the stability of perovskite solar cell based on Bi instead of Pb as its attractive aspects suggest that Bi can be used to make less toxic material and also allow operate the solar cell for a longer life time. However, materials based on Bi also

need to be studied to more fully understand them, and in order to bring them a level competitive with the lead perovskite solar cell.

2.6 References

1. Chen, Q., N. De Marco, Y. Yang, T.-B. Song, C.-C. Chen, H. Zhao, Z. Hong, and H. Zhou, Under the spotlight: The organic–inorganic hybrid halide perovskite for optoelectronic applications. Nano Today, 2015. **10**(3): p. 355-396.
2. Gao, P., M. Grätzel, and M.K. Nazeeruddin, Organohalide lead perovskites for photovoltaic applications. Energy & Environmental Science, 2014. **7**(8): p. 2448-2463.
3. Hsiao, Y.-C., T. Wu, M. Li, Q. Liu, W. Qin, and B. Hu, Fundamental physics behind high-efficiency organo-metal halide perovskite solar cells. Journal of Materials Chemistry A, 2015. **3**(30): p. 15372-15385.
4. Luo, S. and W.A. Daoud, Recent progress in organic-inorganic halide perovskite solar cells: mechanisms and material design. Journal of Materials Chemistry A, 2015. **3**(17): p. 8992-9010.
5. Kazim, S., M.K. Nazeeruddin, M. Grätzel, and S. Ahmad, Perovskite as light harvester: a game changer in photovoltaics. Angewandte Chemie International Edition, 2014. **53**(11): p. 2812-2824.
6. Niu, G., X. Guo, and L. Wang, Review of recent progress in chemical stability of perovskite solar cells. Journal of Materials Chemistry A, 2015. **3**(17): p. 8970-8980.

7. Bhatnagar, A., A.R. Chaudhuri, Y.H. Kim, D. Hesse, and M. Alexe, Role of domain walls in the abnormal photovoltaic effect in BiFeO3. Nature Communications, 2013. **4**.

8. Choi, T., S. Lee, Y. Choi, V. Kiryukhin, and S.-W. Cheong, Switchable ferroelectric diode and photovoltaic effect in BiFeO3. Science, 2009. **324**(5923): p. 63-66.

9. Ji, W., K. Yao, and Y.C. Liang, Bulk photovoltaic effect at visible wavelength in epitaxial ferroelectric BiFeO3 thin films. Advanced Materials, 2010. **22**(15): p. 1763-1766.

10. Sum, T.C. and N. Mathews, Advancements in perovskite solar cells: photophysics behind the photovoltaics. Energy & Environmental Science, 2014. **7**(8): p. 2518-2534.

11. Green, M.A., A. Ho-Baillie, and H.J. Snaith, The emergence of perovskite solar cells. Nature Photonics, 2014. **8**(7): p. 506-514.

12. Li, C., X. Lu, W. Ding, L. Feng, Y. Gao, and Z. Guo, Formability of ABX_3 (X= F, Cl, Br, I) Halide Perovskites. Acta Crystallographica Section B: Structural Science, 2008. **64**(6): p. 702-707.

13. Elumalai, N.K., M.A. Mahmud, D. Wang, and A. Uddin, Perovskite Solar Cells: Progress and Advancements. Energies, 2016. **9**(11): p. 861.

14. Im, J.-H., J. Chung, S.-J. Kim, and N.-G. Park, Synthesis, structure, and photovoltaic property of a nanocrystalline 2H perovskite-type novel sensitizer (CH3CH2NH3) PbI3. Nanoscale Research Letters, 2012. **7**(1): p. 353.

15. Baikie, T., Y. Fang, J.M. Kadro, M. Schreyer, F. Wei, S.G. Mhaisalkar, M. Graetzel, and T.J. White, Synthesis and crystal chemistry of the hybrid perovskite (CH 3 NH 3) PbI 3 for solid-state sensitised solar cell applications. Journal of Materials Chemistry A, 2013. **1**(18): p. 5628-5641.

16. Fan, Z., K. Sun, and J. Wang, Perovskites for photovoltaics: a combined review of organic-inorganic halide perovskites and ferroelectric oxide perovskites. Journal of Materials Chemistry A, 2015. **3**(37): p. 18809-18828.

17. Kojima, A., K. Teshima, Y. Shirai, and T. Miyasaka, Organometal Halide Perovskites as Visible-Light Sensitizers for Photovoltaic Cells. Journal of the American Chemical Society, 2009. **131**(17): p. 6050-6051.

18. McKinnon, N.K., D.C. Reeves, and M.H. Akabas, 5-HT3 receptor ion size selectivity is a property of the transmembrane channel, not the cytoplasmic vestibule portals. The Journal of General Physiology, 2011. **138**(4): p. 453-466.

19. Luo, S. and W.A. Daoud, Crystal Structure Formation of CH3NH3PbI3-xClx Perovskite. Materials, 2016. **9**(3): p. 123.

20. Kojima, A., Teshima, K., Miyasaka, T. & Shirai, Y. , Novel photoelectrochemical cell with mesoscopic electrodes sensitized by lead-halide compounds (2). 210th ECS Meeting (ECS, 2006). , 2006.

21. Kim, H.-S., C.-R. Lee, J.-H. Im, K.-B. Lee, T. Moehl, A. Marchioro, S.-J. Moon, R. Humphry-Baker, J.-H. Yum, and J.E. Moser, Lead iodide perovskite sensitized all-solid-state submicron thin film mesoscopic solar cell with efficiency exceeding 9%. Scientific reports, 2012. **2**: p. 591.

22. Stranks, S.D., G.E. Eperon, G. Grancini, C. Menelaou, M.J. Alcocer, T. Leijtens, L.M. Herz, A. Petrozza, and H.J. Snaith, Electron-hole diffusion lengths exceeding 1 micrometer in an organometal trihalide perovskite absorber. Science, 2013. **342**(6156): p. 341-344.

23. Liu, M., M.B. Johnston, and H.J. Snaith, Efficient planar heterojunction perovskite solar cells by vapour deposition. Nature, 2013. **501**(7467): p. 395.

24. Jeon, N.J., J.H. Noh, Y.C. Kim, W.S. Yang, S. Ryu, and S.I. Seok, Solvent engineering for high-performance inorganic–organic hybrid perovskite solar cells. Nature materials, 2014. **13**(9): p. 897-903.

25. Jeon, N.J., J.H. Noh, W.S. Yang, Y.C. Kim, S. Ryu, J. Seo, and S.I. Seok, Compositional engineering of perovskite materials for high-performance solar cells. Nature, 2015. **517**(7535): p. 476.

26. Yang, W.S., J.H. Noh, N.J. Jeon, Y.C. Kim, S. Ryu, J. Seo, and S.I. Seok, High-performance photovoltaic perovskite layers fabricated through intramolecular exchange. Science, 2015. **348**(6240): p. 1234-1237.

27. Saliba, M., T. Matsui, J.-Y. Seo, K. Domanski, J.-P. Correa-Baena, M.K. Nazeeruddin, S.M. Zakeeruddin, W. Tress, A. Abate, A. Hagfeldt, and M. Gratzel, Cesium-containing triple cation perovskite solar cells: improved stability, reproducibility and high efficiency. Energy & Environmental Science, 2016. **9**(6): p. 1989-1997.

28. Jeon, N.J., J.H. Noh, W.S. Yang, Y.C. Kim, S. Ryu, J. Seo, and S.I. Seok, Compositional engineering of perovskite materials for high-performance solar cells. Nature, 2015. **517**(7535): p. 476-480.

29. Zhou, H., Q. Chen, G. Li, S. Luo, T.-b. Song, H.-S. Duan, Z. Hong, J. You, Y. Liu, and Y. Yang, Interface engineering of highly efficient perovskite solar cells. Science, 2014. **345**(6196): p. 542-546.

30. Liu, M., M.B. Johnston, and H.J. Snaith, Efficient planar heterojunction perovskite solar cells by vapour deposition. Nature, 2013. **501**(7467): p. 395-398.

31. Bai, S., Z. Wu, X. Wu, Y. Jin, N. Zhao, Z. Chen, Q. Mei, X. Wang, Z. Ye, T. Song, R. Liu, S.-t. Lee, and B. Sun, High-performance planar heterojunction perovskite solar cells: Preserving long charge carrier diffusion lengths and interfacial engineering. Nano Research, 2014. **7**(12): p. 1749-1758.

32. Heo, J.H., D.H. Song, B.R. Patil, and S.H. Im, Recent progress of innovative perovskite hybrid solar cells. Israel Journal of Chemistry, 2015. **55**(9): p. 966-977.

33. Koutselas, I., L. Ducasse, and G.C. Papavassiliou, Electronic properties of three- and low-dimensional semiconducting materials with Pb halide and Sn halide units. Journal of Physics: Condensed Matter, 1996. **8**(9): p. 1217.

34. Stoumpos, C.C. and M.G. Kanatzidis, The renaissance of halide perovskites and their evolution as emerging semiconductors. Accounts of chemical research, 2015. **48**(10): p. 2791-2802.

35. Noh, J.H., S.H. Im, J.H. Heo, T.N. Mandal, and S.I. Seok, Chemical management for colorful, efficient, and stable inorganic–organic hybrid nanostructured solar cells. Nano letters, 2013. **13**(4): p. 1764-1769.

36. Schlipf, J., P. Docampo, C.J. Schaffer, V. Körstgens, L. Bießmann, F. Hanusch, N. Giesbrecht, S. Bernstorff, T. Bein, and P. Müller-Buschbaum, A Closer Look

into Two-Step Perovskite Conversion with X-ray Scattering. The journal of physical chemistry letters, 2015. **6**(7): p. 1265-1269.

37. Barrows, A.T., S. Lilliu, A.J. Pearson, D. Babonneau, A.D. Dunbar, and D.G. Lidzey, Monitoring the Formation of a CH3NH3PbI3–xClx Perovskite during Thermal Annealing Using X-Ray Scattering. Advanced Functional Materials, 2016. **26**(27): p. 4934-4942.

38. Tan, K.W., D.T. Moore, M. Saliba, H. Sai, L.A. Estroff, T. Hanrath, H.J. Snaith, and U. Wiesner, Thermally induced structural evolution and performance of mesoporous block copolymer-directed alumina perovskite solar cells. Acs Nano, 2014.

39. Moore, D.T., H. Sai, K.W. Tan, D.-M. Smilgies, W. Zhang, H.J. Snaith, U. Wiesner, and L.A. Estroff, Crystallization kinetics of organic–inorganic trihalide perovskites and the role of the lead anion in crystal growth. Journal of the American Chemical Society, 2015. **137**(6): p. 2350-2358.

40. Bi, D., W. Tress, M.I. Dar, P. Gao, J. Luo, C. Renevier, K. Schenk, A. Abate, F. Giordano, and J.-P.C. Baena, Efficient luminescent solar cells based on tailored mixed-cation perovskites. Science advances, 2016. **2**(1): p. e1501170.

41. Noel, N.K., S.D. Stranks, A. Abate, C. Wehrenfennig, S. Guarnera, A.-A. Haghighirad, A. Sadhanala, G.E. Eperon, S.K. Pathak, and M.B. Johnston, Lead-free organic–inorganic tin halide perovskites for photovoltaic applications. Energy & Environmental Science, 2014. **7**(9): p. 3061-3068.

42. Kwak, C.K., A.T. Barrows, A.J. Pearson, D.G. Lidzey, and A.D. Dunbar, An X-ray scattering and electron microscopy study of methylammonium bismuth

perovskites for solar cell applications. Journal of Materials Research, 2017. **32**(10): p. 1888-1898.

43. Park, B.W., B. Philippe, X. Zhang, H. Rensmo, G. Boschloo, and E.M. Johansson, Bismuth based hybrid perovskites A3Bi2I9 (A: methylammonium or cesium) for solar cell application. Advanced Materials, 2015. **27**(43): p. 6806-6813.

44. Hoye, R.L., R.E. Brandt, A. Osherov, V. Stevanović, S.D. Stranks, M.W. Wilson, H. Kim, A.J. Akey, J.D. Perkins, and R.C. Kurchin, Methylammonium bismuth iodide as a lead-free, stable hybrid organic–inorganic solar absorber. Chemistry-A European Journal, 2016. **22**(8): p. 2605-2610.

45. Eckhardt, K., V. Bon, J. Getzschmann, J. Grothe, F.M. Wisser, and S. Kaskel, Crystallographic insights into (CH 3 NH 3) 3 (Bi 2 I 9): a new lead-free hybrid organic–inorganic material as a potential absorber for photovoltaics. Chemical Communications, 2016. **52**(14): p. 3058-3060.

46. Lyu, M., J.-H. Yun, M. Cai, Y. Jiao, P.V. Bernhardt, M. Zhang, Q. Wang, A. Du, H. Wang, G. Liu, and L. Wang, Organic–inorganic bismuth (III)-based material: A lead-free, air-stable and solution-processable light-absorber beyond organolead perovskites. Nano Research, 2016. **9**(3): p. 692-702.

Chapter 3: Experimental Methods

As was stated in **Chapter 1**, this thesis aims to investigate the dynamic crystallisation of different categories of organic halide perovskite materials used in solar cell devices. In order to achieve this aim, several experimental methods were used to characterize the materials.

The materials preparation methods are discussed in **Section 3.1** and the characterization tools involve the interaction of matter with X-rays, electrons and Ultraviolet-visible light.

Section 3.2 presents the work of X-ray scattering and diffraction physics to identify the formation mechanism of the crystalline products in perovskite film during the spin coating processes using *in situ* spin coating wide angle X-ray scattering WAXS experiments.

In **Chapter 5**, grazing incidence wide angle X-ray scattering (GI-WAXS) is applied to study the effects of the thermal annealing on the crystalline structure of $FAPbI_{3-x}Cl_x$ perovskite films. Therefore, the GI-WAXS procedure will be discussed in **Section 3.2-2.**

The surface morphology and crystallization of perovskite films were investigated using scanning electron microscopy (SEM), which will be described in **Section 3.3**. **Section 3.4** will explain how light absorption and the optical band gap were measured using UV-Vis spectroscopy.

3.1 Sample Preparation

3.1.1 Perovskite Solution Preparation

In this thesis, three categories of perovskite materials were investigated. The first category is perovskite based on methylammonium lead iodide chloride ($MAPbI_{3-x}Cl_x$). The formamidinium lead iodide chloride ($FAPbI_{3-x}Cl_x$) perovskite is the second category which both categories detailed in **Chapter 4** and **Chapter 5**. The third group is the lead-free materials related to perovskite category that was also investigated, including $MA_3Bi_2I_{9-x}Cl_x$ and the composition of bismuth iodide with FA and MA, which form $FA_3Bi_2I_9$ and $MA_3Bi_2I_9$ perovskite, respectively. The FA and MA cations are abbreviations of $NH_2CH{=}NH_2$ and CH_3NH_3, respectively. Lead-free perovskite will be discussed in **Chapter 6.**

The simple one-step solution preparation mechanism that was detailed in **Chapter 2** was applied to prepare all perovskite solutions as was described in the literature [1, 2].

To prepare the perovskite $MAPbI_{3-x}Cl_x$ solution, methylammonium iodide (MAI) and lead chloride ($PbCl_2$) were mixed in a 3:1 molar ratio. The MAI and $PbCl_2$ were purchased from Sigma-Aldrich. The 3:1 molar ratio was selected because in the literature it obtained high quality perovskite materials [3, 4]. The mixture was dissolved in anhydrous dimethylformamide (DMF) that were purchased from Sigma-Aldrich to form a 3.2 M solution.

Similarly, the $FAPbI_{3-x}Cl_x$ ink was prepared by mixing formamidinium iodide (FAI), which was purchased from Ossila Ltd, and lead chloride ($PbCl_2$), purchased from Sigma-

Aldrich, in a 3:1 molar ratio. The mixture was then dissolved in anhydrous DMF to form a 3.2 M solution. To avoid the toxicity associated with lead in the perovskite materials, bismuth chloride ($BiCl_3$) and bismuth iodide (BiI_3) were applied instead of lead chloride ($PbCl_2$). $BiCl_3$ supplied by Acros Organics was mixed with MAI using the same 3:1 molar ratio and the same DMF solvent to form a 3.2 M solution of $MA_3Bi_2I_9Cl_x$.

$FA_3Bi_2I_9$ and $MA_3Bi_2I_9$ solutions were prepared by mixing bismuth iodide (BiI_2), which was supplied by Sigma-Aldrich Company Ltd, with FAI and MAI in a 1:1 molar ratio with BiI_2, respectively. The mixture was then dissolved in a DMF solvent to form the same solution concentration. All the solutions were prepared under ambient conditions where the humidity in the labs was between 35% and 40%. Before using any of the precursor inks, they were heated to 70^{o}C and stirred for at least 30 minutes.

3.1.2 Perovskite Film Preparation

After dissolving materials in the solvent to from the perovskite precursor ink, these solutions were deposited by the spin coating process. Spin coating is a commonly used method because it is cost-effective, simple and a sufficiently uniform perovskite film can be obtained. A small amount of each solution was deposited in the substrate's rotating centre, causing an equal distribution of solution in all directions. Flat, thin, uniform films then can be obtained, as shown in **Fig 3.1**. Decrease the speed of substrate can result in a higher film thickness to be formed [5, 6]. Solution concentration and viscosity, on the other hand, have a positive correlation with the film thickness.

For perovskite film preparation for wide angle X-ray scattering experiments, two types of substrates were used. Transparent 1×1 cm^2 mica substrates were used, after being cleaned

using nitrogen to remove all dust and particles, in the wide angle X-ray scattering experiments in transmission geometry (T-WAXS). In the grazing incidence wide angle X-ray scattering (GI-WAXS) experiments, Si wafer with a native oxide cleaved into 1×1 cm^2 section were used and each was cleaned in acetone and isopropanol for 15 min. Each substrate was then dried using a nitrogen gas stream. For SEM and UV-Vis spectroscopy measurements, glass substrates were used microscopes slide were cleaved into 1×1 cm^2 pieces and cleaned by the same solvents as used previously.

A conventional horizontal, referring to the plane of the rotation, spin coater, supplied by Ossila Ltd, was used for the spin coating. Perovskite solutions were spin coated on a substrate at 3000 rpm for 30s.

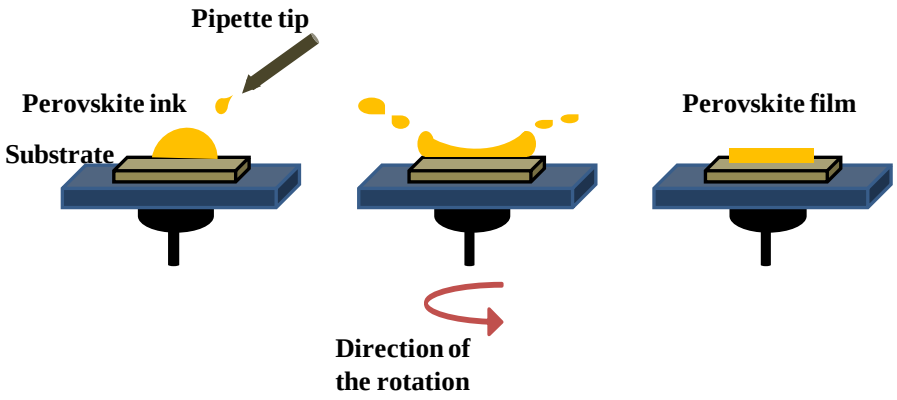

Figure 3.1: The spin coating processes using a horizontal spin coater that used to formed a perovskite film.

For the thermal annealing of all samples in this thesis, the temperature is referring to of the hotplate reading. The $MAPbI_{3-x}Cl_x$, perovskite films were thermally annealed for 2 h at 90^{o}C, as was described in the literature [7], while the thermal annealing of $FAPbI_{3-x}Cl_x$

was 1 h at 190^{o}C. The study of different annealing temperatures and times for the $FAPbI_{3-x}Cl_x$ perovskite films and application of GI-WAXS measurements will be detailed in **Chapter 5**.

For the lead-free materials annealing conditions were applied according to the organic cation. Therefore, compositions of FA organic cation with bismuth chloride and bismuth iodide were annealed at 190^{o}C for 60 min, whereas the compositions of MAI with bismuth chloride and bismuth iodide were annealed for 120 min at 90^{o}C.

The temperature of the hotplate reading has been used here in the thesis. For more accurate temperature measurement, the temperature of the hotplate was measured using a thermocouple before and after the substrates. The data is listed in Table 3.1, where approximately ten degrees less than the hotplate reading was noted before placing the substrate, and ten degrees more was recorded after placing the substrate. For example, a sample that was heated to 190^{o}C on the hotplate showed 180^{o}C on average using an electronic thermometer before placing the substrate, and 170^{o}C after the glass substrate was added.

Hotplate reading(^{o}C)	Temperature recorded at the hotplate top surface (^{o}C)	Temperature recorded on the sample top surface(^{o}C)	ΔT(^{o}C)
90	81.5	72	9.5
	80.5	71.5	9
	81.2	70.2	11
130	121.5	115.3	6.2
	122.3	112.2	10.1
	122.5	115.5	7
170	158.5	152.2	6.3
	160.2	152.3	7.9
	159.2	151.8	7.4
190	180	169	11
	178.9	168.3	10.6
	180	170.3	9.7

Table 3.2: The recording of temperature measured by an electronic thermometer before and after using the substrate

3.2 Wide Angle X-ray Scattering WAXS

The high flux of X-ray synchrotron radiation available at the Diamond Light Source (Didcot, England) 107 beamline was applied to investigate the crystal structure of perovskite using wide angle X-ray scattering (WAXS).

Theoretically, the incident X-ray beam is elastically scattered by the atoms in a sample and is reflected if the structure is periodically arranged, such as the arrangement of the lattice plane. Our case study is of the crystalline structure of organic–halide perovskites. The conditions for the diffraction of the X-ray beam by the crystalline structure are governed by the well-known Bragg law, Equation 3.1. As shown in **Fig 3.2,** the incident X-ray beam goes through the sample at an incidence angle **θ,** and is reflected by the crystal planes that are arranged in a parallel structure with a separation distance between the lattice planes **d**. If the parallel reflected waves are in phase, then constructive interference arises and, thus, an intense reflection signal can be recorded. Therefore, the more intense and sharper diffracted intensity means the higher the degree of the structure's periodicity. The destructive interference occurred from the out of the phase waves, and no intensity signal can be collected in this case.

$$n\lambda = 2dsin(\theta) \qquad \text{(Eq. 3.1)}$$

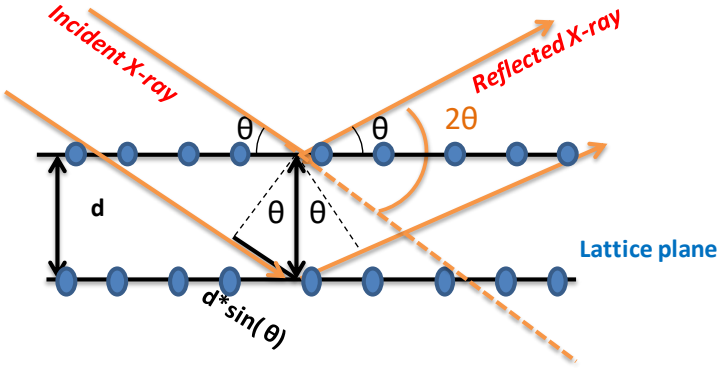

Figure 3.2: Presentation of the Bragg diffraction conditions.

Fig. 3.3 presents illustrations of the X-ray scattering processes, considering the reciprocal space of the sample. The incident X-ray beam is scattered at 2θ angle after hitting the sample (**Fig 3.3, 1)**. The scattering vector, q, is defined as the difference between the scattered wave and the incident wave vectors K_s , K_i, as is expressed in equation 3.2 and (**Fig 3.3, 2)**. The intersection between the reciprocal lattice of the sample and the Ewald sphere can be recorded by detector as scattering signal (**Fig 3.3, 3).** The Ewald sphere is the sphere that illustrates the relationship between the incident and scattered vectors and the sample and is named after the crystallographer Peter Ewald[7].

The advantages of using WAXS experiments over one-dimensional X-ray diffraction experiments is the ability to obtain 2D WAXS data, which provides more information about the crystalline structure orientation.

$$q = K_s - K_i = \left(\frac{2\pi}{d}\right) = \left(\frac{4\pi sin\theta}{\lambda}\right) \qquad \text{(Eq. 3.2)}$$

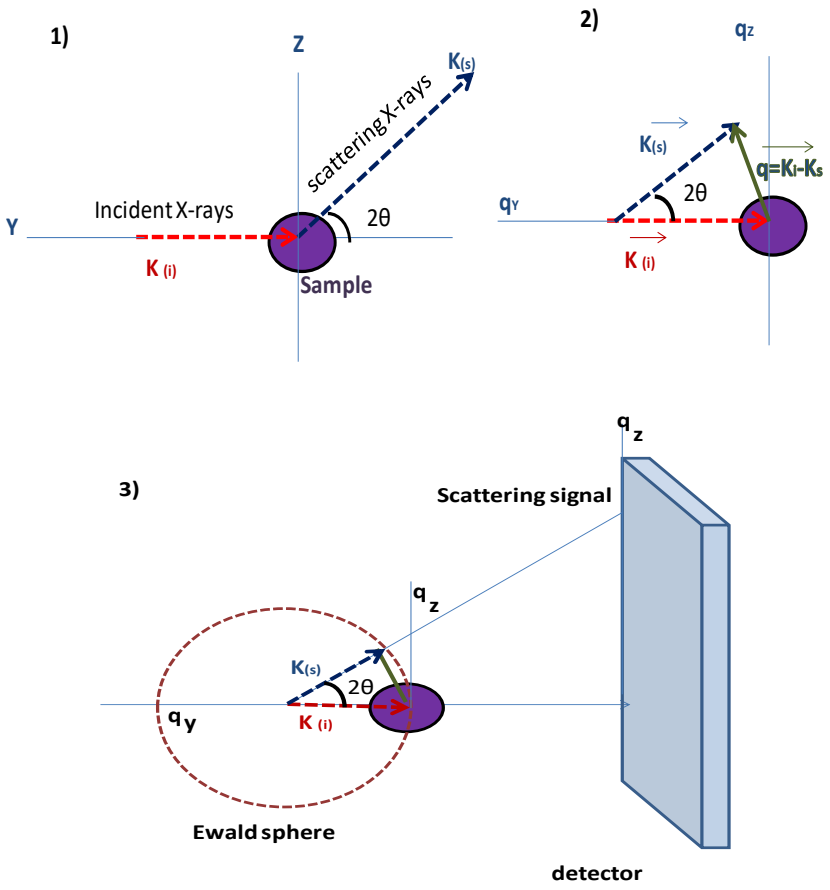

Figure 3.3: The geometrical constructive of the X-ray scattering processes.

Two types of WAXS geometries have been utilized in this thesis. WAXS in transmission geometry was performed to observe the crystalline structure of perovskite materials during *in situ* spin coating. In the second section, the wide angle X-ray scattering applied at grazing incidence (GI). One advantage of GI-WAXS over WAXS is that high surface sensitivity in Grazing incidence can be observed, thus minimising substrate effects. However, in GI-WAXS the need for the carful alignment, between the X-ray and the sample, is required which consumes more time and effort.

Peter Müller-Buschbaum reported a basic explanation of the different sample orientations and the corresponding 2D GI-WAXS images [8]. A summary of the explanation is

sketched in **Fig 3.4**, where four samples corresponding to high to low crystalline orientations.

Sample 1 was formed from the horizontal lattice planes, and sample 2 presented the horizontal and vertical planes. No orientation was observed in both samples, so the scattering signals are presented as spots in the out-of-planes and in-plane. The orientation becomes stronger as the scattering rings are completed, as seen in sample 3 and sample 4. Sample 3 is an example of a weaker oriented sample, whereas sample 4 is a high oriented sample so the scattering rings can be seen clearly.

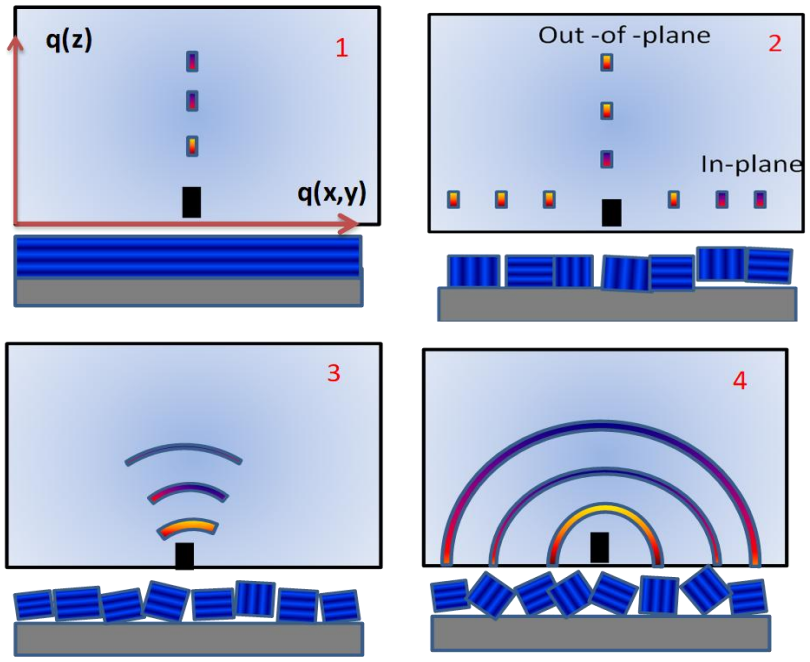

Figure 3.4: Different crystal samples and the corresponding 2D GI-WAXS data, sample that contains only one level of orientation for out-of-plane in **1**, and the horizontal and vertical orientations can be seen in **2**, where **3** and **4** of the sample with different levels of orientation so the high orientation level can form the full WAXS rings.

3.2-1 *In situ* Spin Coating T-WAXS Experiments

To allow for the *in situ* measurement to be performed, a vertical spin coater was developed placed in a sample chamber, as illustrated in **Fig. 3.5**. Using a vertical spin coater in transmission-WAXS mode avoided complication due to sample misalignment due to the transmission geometry and the ease of data collection during the solution deposition. 100 µl of perovskite solution was loaded into the pipette tip using a remote by controlled syringe pump. The solution was then deposited into a mica substrate mounted on the hollow shaft motor to rotate the solution and form a perovskite film. The rotation of the spin casting speed was controlled by changing the supply voltage. Calibration of the spin coater rotation speed was done by Dr Alan Dunbar using a bright LED. A light-dependent resistor was connected to an oscilloscope to determine the frequency of flashes from a reflective patch that was stuck on the side of the rotating motor. The lower supply voltage used was 10 V giving a 26.2 Hz or 780 RPM. Faster rotations were tested by changing the supply voltage to 20 V.

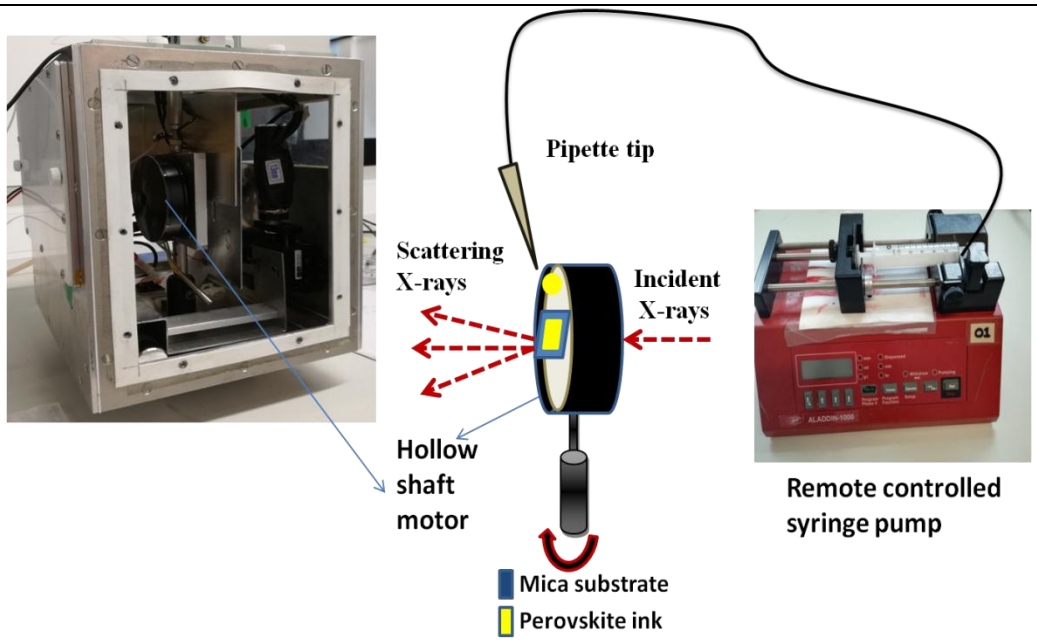

Figure 3.5: The spin coater was placed inside the sample chamber where the perovskite liquid was deposited by a remote controlled syringe pump.

The sample chamber was flooded by helium to minimise the air scattering effects. The X-ray beam energy was 10.5KeV and had a wavelength of 1.18 Å where the beam centre was located at pixel (1235, 1651). The T-WAXS beam was detected by a Pilatus 2M detector at a distance of 42.1cm from the sample.

Fig. 3.6 shows an overall illustration of the T-WAXS experiments. The schematic view of the transmission geometry is illustrated in **Fig. 3.6a**, while the actual alignment of the X-ray synchrotron, a sample chamber with a 2D Pilates 2M detector, can be seen in the photograph in **Fig. 3.6b.** The calibration was performed by measuring well defined a structure silver behenate sample that is frequently used for calibration [9-11].

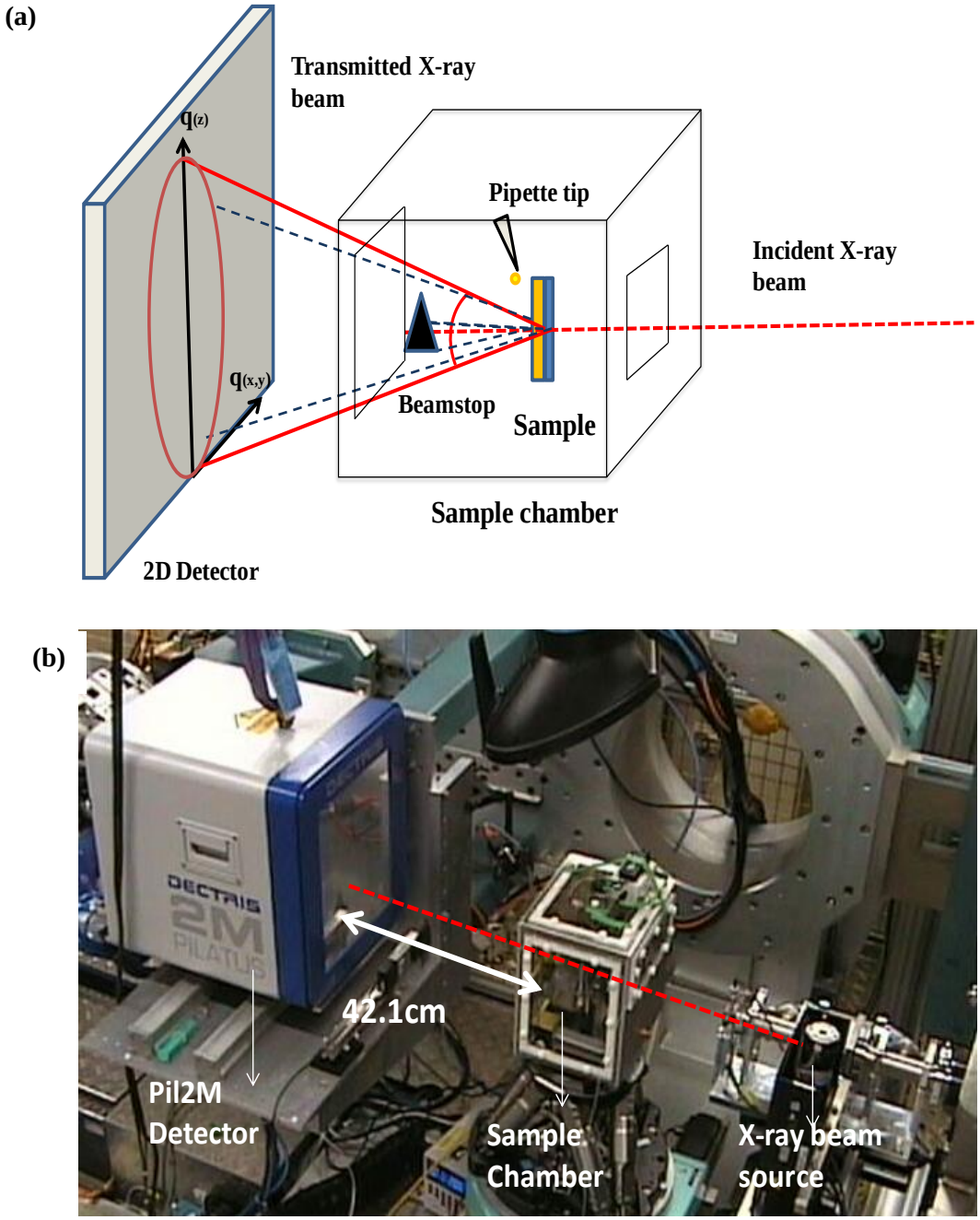

Figure 3.6: Summary of the T-WAXS experiment, a schematic view of the geometry of T-WAXS (a) and an image of the T- WAXS setup, which depicts the position of the X-ray beam using a red line (b).

3.2-2 Grazing incidence Wide Angle Scattering GI-WAXS

In order to investigate the crystal structure of the perovskite films annealed for different annealing times and temperatures, as will be detailed in **Chapter 5,** GI-WAXS was applied. The X-ray beam energy used was 10.5 keV and the wavelength was 1.18 Å. The incident angle ranged from 0.1^{o} to 0.6^{o} with scan rate 0.02^{o} where applied.

The scattered X-rays were collected by a Pilatus 2M Detector at a sample-detector distance of 29 cm. Here, the reflected and transmitted beams were blocked by a beam stop that is located inside the sample chamber. The same calibration method used in T-WAXS was applied, where the silver behenate sample was scanned.

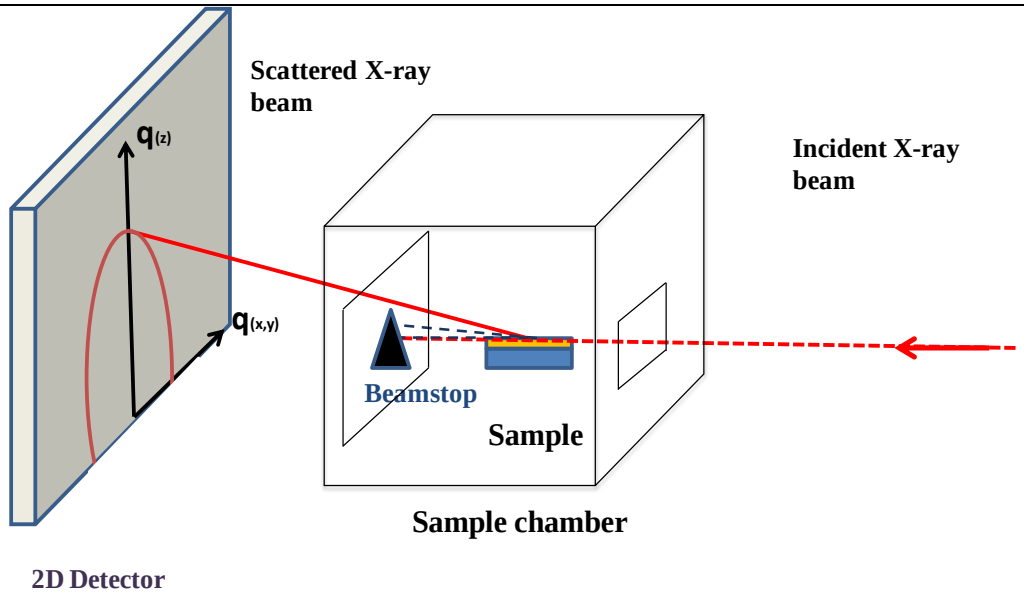

Figure 3. 7: The geometry of the Grazing incidence wide angle X-ray scattering.

3.2-3 The graphical presentation of WAXS Data

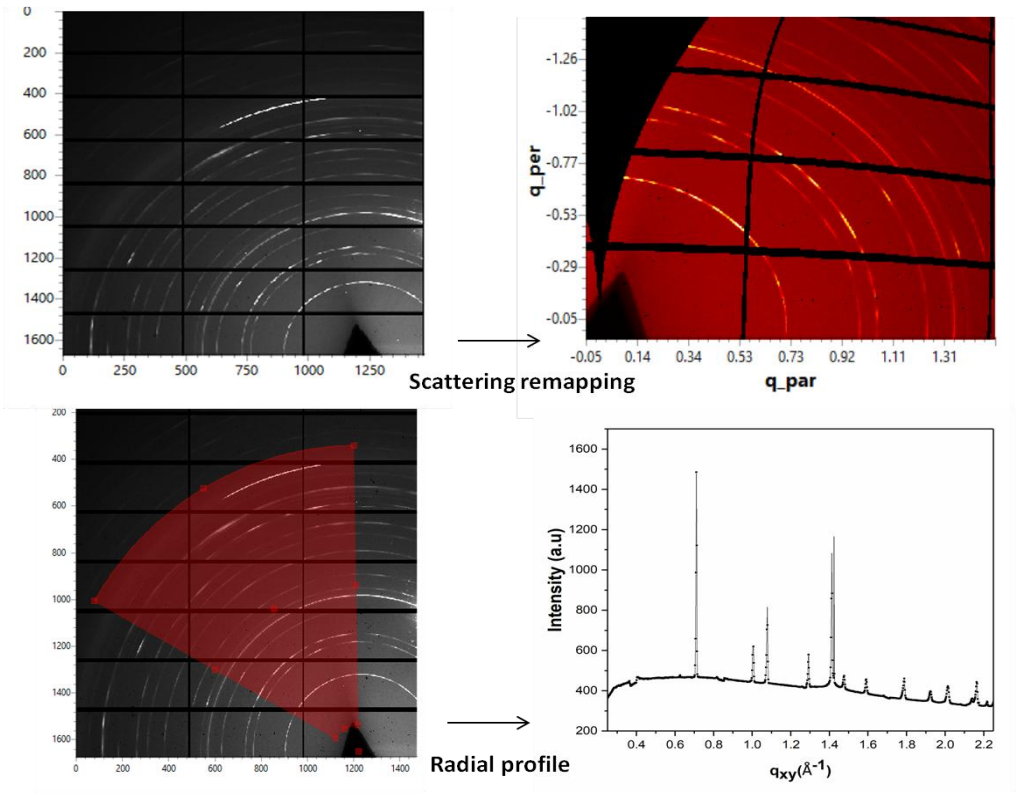

Figure 3.8: The image processing in DAWN software to create the intensity plot against q.

First, the WAXS images are collected and analyzed by DAWN software in the pixel and using the processing image the pixel is remapping into (q) units. The curved line that presented Ewald sphere it should be considered. To plot the intensity of WAXS signal against q, the radial profile is scanned where the selected area should be covered all the interesting q. For perovskite, the interesting q values from q=0.35 Å^{-1} to 2.25 Å^{-1}. Further illustration is presented in **Fig3.8.**

3.3 Scanning Electron Microscopy (SEM)

SEM used electron beam that provide a higher resolution image than the optical microscopy that is based on visible light since electrons have a shorter wavelength [12].

A schematic presentation for a SEM system is shown in **Fig.3.9** and contains the electron gun, lens and detector, where all are kept under the vacuum. The vacuum chamber prevents any interaction of air molecules with the electron beam that could cause sample damage, reduce the quality of the image, and scatter the e-beam.

The electron beam can is generated using a thermionic emission of an electron gun, where sufficient heating of the filament causes electrons be to released, or by extracting electrons from a tungsten crystal that is done by a high electric field. Therefore, this type of SEM is called Field Emission Gun Scanning Electron Spectroscopy (FEGSEM). In this thesis, the electron beam was generated using thermionic emission from a filament.

After accelerating the emitted electrons with a positive anode, the electron beam travels inside the vacuum chamber under the effects of the electromagnetic field. The spot size of the electron beam on the sample is controlled using a condenser lens and the aperture.

The secondary electron signal SEs, the backscattering electron signals BES and an X-ray signal can be collected. All signals are generated as result of the electrum beam interaction with sample and are emitted according to the depth of the electron beam penetration inside the sample.

SEM data in this thesis was collected using JEOL JSM6010LA, where the detector is a multi-segment secondary electron detector with applied electron energy of 10 kV.

The surface coverage percentage of each sample we calculated using Image-J software.

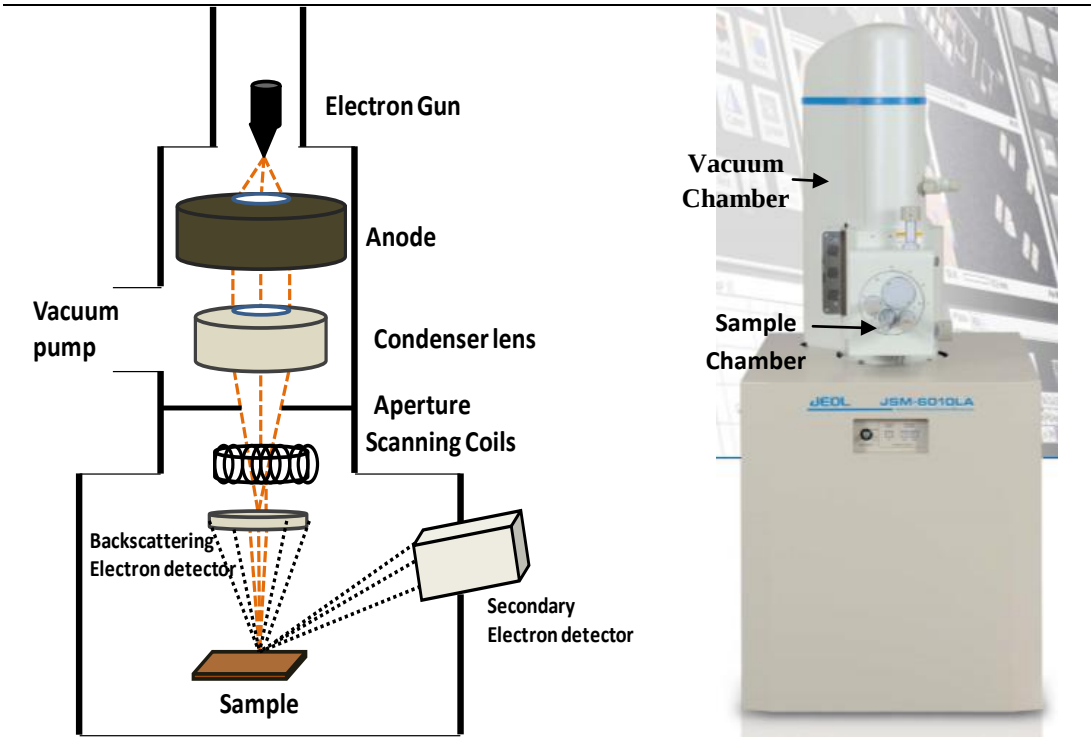

Figure 3.9: Schematic presentation of the Scanning Electron Microscopy (SEM) system.

3.4 UV-Vis spectroscopy

Ultraviolet-visible absorption spectra of perovskite materials were obtained using an Ocean Optics USB2000+ spectrometer, and a DT-MINI-2-GS Deuterium-Halogen light source. As shown in **Fig. 3.10,** light from deuterium halogen source travels through a optical fibre. Inside the spectrometer, the amount of light is adjusted and the resolution was controlled by the slit. The directed light from the slit hits the collimator mirror that focused the light onto an angled grating. The main function of the grating is to split the received light according to its wavelength and direct it to the focusing mirrors, which focus the first order spectra of the diffracted light onto the detector. The spectra of light

were collected by the detector and the light signal was converted to a numerical value as a function of wavelength.

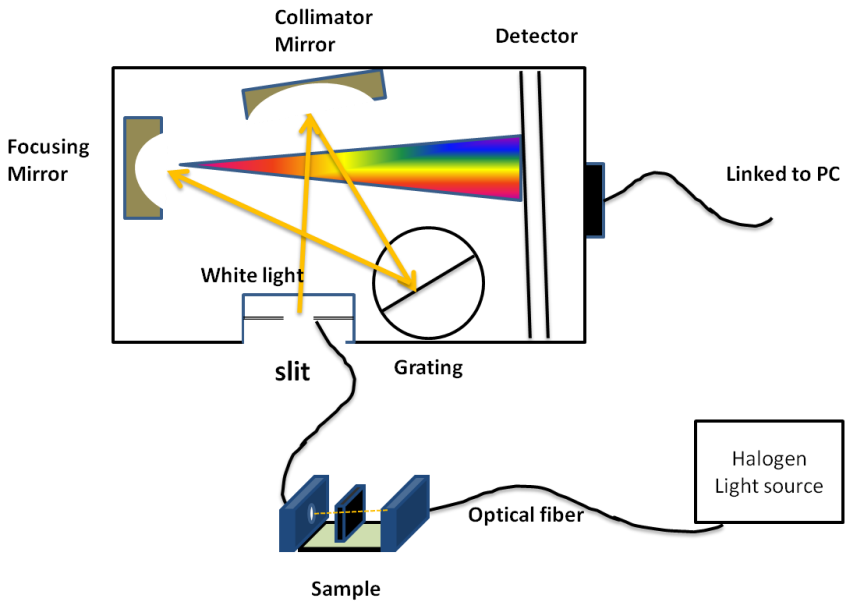

Figure3.10: The main components of USB spectroscopy to measure the absorption spectra.

Light absorption was qualified by the absorption coefficient that can be defined by Beer's law, Equation 3.3. Assuming the optical beam is propagating a sample thickness of $\boldsymbol{dz}$, in z direction and with an optical power per area unit that is defined as intensity $\boldsymbol{I(z)}$, a decrease in the intensity of the light due to absorption within the thickness that can be numerically expressed using in Equation 3.3 [13].

$$\int \frac{I}{I(z)} d(I) = \alpha dz \qquad (Eq.3.3)$$

The transmission $T(\lambda)$ can be defined as the ratio of the intensity of incident light and intensity of the remaining light. The absorption is plotted as a wavelength function.

$$A = -ln\frac{I}{I_o} = -lnT(\lambda) \qquad (\text{Eq.}3.4)$$

Using the Tauc plot that governs the relation between the absorption coefficient α and the incident photon energy, the optical band gap can be determined [14, 15]. This relation can be mathematically expressed as shown in Equation 3.5.

$$\alpha = \frac{\beta}{h\nu}\left(h\nu - E_g\right)^n \qquad \text{(Eq. 3.5)}$$

That can be arranged to be in this well-known Tauc formula:

$$(\alpha\, h\nu)^{1/n} = \left(h\nu - E_g\right)\beta \qquad \text{(Eq. 3.6)}$$

Here, E_g is the optical band gap, and parameter β is constant related to the variation in the semiconductor band and, finally, n presents the order of the transition.

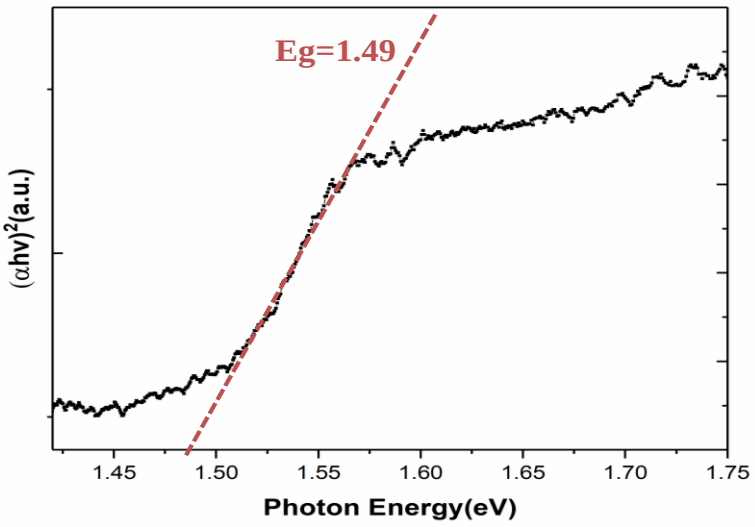

Figure 3.11: Example of Tauc plot in red to determine the bandgap of semiconductor.

3.5 References

1. Gao, P., M. Gratzel, and M.K. Nazeeruddin, Organohalide lead perovskites for photovoltaic applications. Energy & Environmental Science, 2014. **7**(8): p. 2448-2463.
2. Lv, S., S. Pang, Y. Zhou, N.P. Padture, H. Hu, L. Wang, X. Zhou, H. Zhu, L. Zhang, and C. Huang, One-step, solution-processed formamidinium lead trihalide ($FAPbI_{(3-x)}Cl_x$) for mesoscopic perovskite–polymer solar cells. Physical Chemistry Chemical Physics, 2014. **16**(36): p. 19206-19211.
3. Park, B.-w., B. Philippe, T.r. Gustafsson, K.r. Sveinbjörnsson, A. Hagfeldt, E.M. Johansson, and G. Boschloo, Enhanced crystallinity in organic–inorganic lead halide perovskites on mesoporous TiO_2 via disorder–order phase transition. Chemistry of Materials, 2014. **26**(15): p. 4466-4471.
4. Yu, H., F. Wang, F. Xie, W. Li, J. Chen, and N. Zhao, The Role of Chlorine in the Formation Process of "$CH_3NH_3PbI_{3-x}Cl_x$" Perovskite. Advanced Functional Materials, 2014. **24**(45): p. 7102-7108.
5. Boix, P.P., K. Nonomura, N. Mathews, and S.G. Mhaisalkar, Current progress and future perspectives for organic/inorganic perovskite solar cells. Materials Today, 2014. **17**(1): p. 16-23.
6. Luo, S. and W.A. Daoud, Recent progress in organic-inorganic halide perovskite solar cells: mechanisms and material design. Journal of Materials Chemistry A, 2015. **3**(17): p. 8992-9010.
7. Liang, P.W., C.Y. Liao, C.C. Chueh, F. Zuo, S.T. Williams, X.K. Xin, J. Lin, and A.K.Y. Jen, Additive enhanced crystallization of solution-processed perovskite

for highly efficient planar-heterojunction solar cells. Advanced Materials, 2014. **26**(22): p. 3748-3754.

8. Müller-Buschbaum, P., The active layer morphology of organic solar cells probed with grazing incidence scattering techniques. Advanced Materials, 2014. **26**(46): p. 7692-7709.

9. Barrows, A.T., S. Lilliu, A.J. Pearson, D. Babonneau, A.D. Dunbar, and D.G. Lidzey, Monitoring the Formation of a CH3NH3PbI3–xClx Perovskite during Thermal Annealing Using X-Ray Scattering. Advanced Functional Materials, 2016. **26**(27): p. 4934-4942.

10. Kwak, C.K., A.T. Barrows, A.J. Pearson, D.G. Lidzey, and A.D. Dunbar, An X-ray scattering and electron microscopy study of methylammonium bismuth perovskites for solar cell applications. Journal of Materials Research, 2017: p. 1-11.

11. Lilliu, S., T. Agostinelli, E. Pires, M. Hampton, J. Nelson, and J.E. Macdonald, Dynamics of crystallization and disorder during annealing of P3HT/PCBM bulk heterojunctions. Macromolecules, 2011. **44**(8): p. 2725-2734.

12. Kelsall, R., I.W. Hamley, and M. Geoghegan, Nanoscale science and technology. 2005: John Wiley & Sons.

13. Fox, M., Optical properties of solids. 2002, AAPT.

14. Aly, K., A.A. Elnaeim, N. Afify, and A. Abousehly, Improvement of the electrical properties of Se 3 Te 1 thin films by In additions. Journal of Non-Crystalline Solids, 2012. **358**(20): p. 2759-2763.

15. Tauc, J., Amorphous and liquid semiconductors. 2012: Springer Science & Business Media.

Chapter 4: Dynamics of $MAPbI_{3-x}Cl_x$ Perovskite Film Crystallization

The aim of the chapter is to understand the dynamics of crystal formation $MAPbI_{3-x}Cl_x$ films. The formation of crystals from the solution during spin coating and after thermal annealing is studied using wide angle X-ray scattering in **Sections 4.1 and 4.2**. The impact of thermal annealing on the morphology of the film is investigated by scanning electron microscopy SEM in **Section 4.3**. The subsequent differences in the UV-Vis spectra of the $MAPbI_{3-x}Cl_x$ film and the extracted optical band gap are discussed in **Section 4.4**. After the film is spin coated and annealed the storage conditions also need to be considered. Therefore, the final part of the chapter will discuss the air exposure to the annealed film in **Section 4.5**.

4.1 *In situ* spin-coating of $MAPbI_{3-x}Cl_x$ film

The crystallization mechanism of the most commonly used perovskite material in solar cell applications, $MAPbI_{3-x}Cl_x$, was studies using wide angle X-ray scattering.

The time dependent *in situ* spin-coating techniques of T-WAXS were used to probe the early stages of the crystalline structure of the perovskite materials. These early stages observations at room temperature during the spin-coating we used assist to understand the mechanisms of the intermediate phase before converting into the final perovskite phase.

First, the substrate mica was measured before perovskite deposition to identify which WAXS features are associated with substrate and therefore can be ignored in our analysis of the perovskite materials that are illustrated in **Fig 4.1**.

The $MAPbI_{3-x}Cl_x$ perovskite was prepared using a one-step technique. After that, it was deposited on the mica substrate and using a vertical spin coater. The solution coated the film as was detailed in **Chapter 3** in **Section 3.2-1**.

Two spin coating speeds, fast and slow, were tested by setting the supply voltage for the rotating motor to 20V that yields 3120 RPM or 10V that yields 1560 RPM, respectively. The WAXS data collected at both spin-coating speeds are plotted in **Fig 4.1** in conjunction with the substrate data. Significant substrate X-ray scattering peaks can be observed at 1.4 $Å^{-1}$and at 2.16$Å^{-1}$ and are labelled by (#). Scattering peaks related to perovskite material on the surface of the mica can be distinguished at 0.85 $Å^{-1}$, 1.1 $Å^{-1}$and 1.2 Å-,which were observed of both the fast and the slow spin-coating velocities. However, the stronger intensity of WAXS and the additional scattering peaks can be obtained from the slower speed. The variation in spin-coating velocity directly affects the thickness of the forming films. Faster spin-coating leads materials distributed the edge of the sample, and a thinner film is formed. Consequently, additional scattering peaks and the stronger WAXS intensity are obtained because of the thicker perovskite film forming when we use the slower speed with a supply voltage of 10 V. Subsequently, all data of *in-situ* WAXS experiments in this project are collected by the same speed at 1560 RPM.

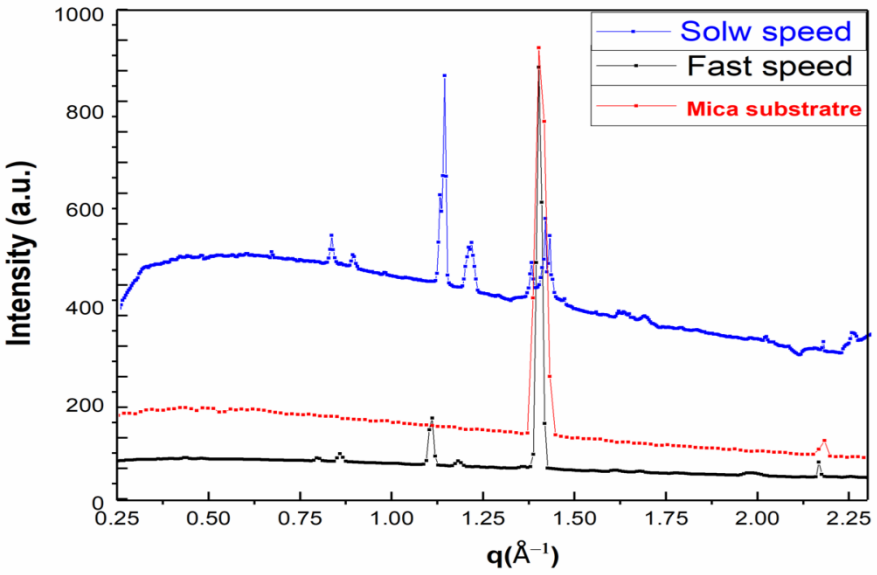

Figure 4.1: T-WAXS patterns of mica substrate before perovskite deposition shown as the red line where the main scattering peaks are labelled (#), and the sample deposited at the slow speed as the blue line, and the sample deposited at the fast spin-coating speed as the black line.

The scattering peak at q=1.1 $Å^{-1}$ is generally assigned to the precursor phase of the mixture of MAI and $PbCl_2$, as was previously defined by wide angle X-ray scattering studies [1, 2]. In both these previously published reports, the scattering peaks at q=1.1 $Å^{-1}$ were observed after the short thermal annealing time of 1 to 5 minutes. The same peak was detected and defined precisely as an intermediate product, $MAPbCl_3$, by Unger et al. [3], Chun-Yu Chang et al. [4], and Hui Yu et al. [5] in XRD measurements. Their studies highlighted strong diffraction peak at a Bragg diffraction angle of 15.7°, which is the converted to the scattering vector value of q=1.1 $Å^{-1}$ using Eq. 3.2 where the X-ray wavelength is assumed to be λ=1.54 Å.

As was proposed by Hui Yu et al, the chemical reaction of 3:1 MAI with $PbCl_2$ produces several intermediate products, involving two reaction steps [5]. In the initial step, PbI_2, MAI, and MACl react together to produce $MA_{x+y}PbI_{2+x}Cl_y$. Subsequently, upon heating,

the decomposition of intermediate product can yield the full perovskite phase as well as MACl that is sublimated into gas. The chemical reactions of 3:1 MAI with $PbCl_2$ are illustrated in **Rect. 4.1** and **Rect. 4.2.**

It was assumed for simplicity the $MA_{x+y}PbI_{2+x}Cl_y$ materials can be defined as $MAPbCl_3$ [6].

$$3MAI + PbCl_2 \rightarrow PbI_2 + xMAI + yMACl \qquad \text{Reaction 4.1}$$

$$PbI_2 + xMAI + yMACl \rightarrow \mathbf{MA_{x+y}PbI_{2+x}Cl_y} \rightarrow MAPbI_3 + MACl(g) \uparrow \qquad \text{Reaction 4.2}$$

Fig. 4.2a shows the radial profiles of the *in situ* spin coating of T-WAXS for the $MAPbI_{3-x}Cl_x$ solution for duration of 10 minutes of processing times per second. The T-WAXS is referring to the transmission geometry of wide angle X-ray scattering.

During the first minute, the mica peaks at 1.4 $Å^{-1}$and 2.16 $Å^{-1}$ were observed besides the broad background scatter as expected from the solvent. By increasing the processing time, a growth of crystallization of intermediate products was recognized. A gradual increase in WAXS intensity around q=1.1 $Å^{-1}$ was detected that corresponded to the intermediate phase of $MA_{x+y}PbI_{2+x}Cl_y$. The increase in the WAXS intensity at this scattering vector was due to the rotating sample causing the solvent to dry by evaporation after the initial liquid loss. This results in forming a higher content of intermediate product $MA_{x+y}PbI_{2+x}Cl_y$ during the spin-coating stage.

In addition to the peak at q=1.1 $Å^{-1}$, the weaker scattering of X-ray peaks recorded at q=1.18 $Å^{-1}$q=1.6 $Å^{-1}$ and q=2 $Å^{-1}$ are assigned to the $MA_{x+y}PbI_{2+x}Cl_y$ intermediate phase. The positions of these scattering peaks are in agreement with experimental studies of the

X-ray diffraction analysis [7, 8] and with the modelling work reported in [9]. In these reports, the intermediate phase was described as an unstable cubic alpha phase. With emphasize that in this thesis we present the dynamic measurements during the spin coating whereas in the previous studies the measurements were taken only at the end of the casting processes.

The X-ray scattering peaks between q=0.6 $Å^{-1}$ to 0.8 $Å^{-1}$ relate to the background scatting from the solvent and the crystalline complex involving the solvent that was analyzed by recent similar in-situ annealing X-ray scattering [10, 6].

The features at q=0.62$Å^{-1}$, q=1.4$Å^{-1}$ and around q=2.15$Å^{-1}$ are attributed to the content of MAI, in agreement the investigation of the crystal structure of MAI, as reported previously[11].

To visually present the degree of WAXS intensity during the WAXS exposure time, a T-WAXS intensity colour map is shown in **Fig. 4.2b.** Weaker WAXS intensity is represented by different colour, the stronger WAXS intensity is at the end of the measurements. This representation makes it easier to determine the intensity and ignoring the background scattering from the solvent.

Initially, the highest intensity T-WAX area corresponds to the broad background scattering band from 0.4 $Å^{-1}$ to 0.8 $Å^{-1}$which dominates the first minute of deposition times. As the time increased the colour change from the dark red to the yellow and eventually to light green indicates a changes in the WAXS intensity level that was witnessed in the solvent evaporation and the forming of the crystalline film.

The strong intermediate phase $MA_{x+y}PbI_{2+x}Cl_y$ intensity at 1.1 $Å^{-1}$ that is associated with the weaker T-WAXS intensity of the background scattering from the solvent that becomes evident at t=100 s. This indicates the rapid crystallization of $MA_{x+y}PbI_{2+x}Cl_y$ at room temperature after the solvent evaporates. After rapid initial growth the strong intensity at q=1.1 $Å^{-1}$ remains constant to the end of the T-WAXS measurement.

The feature labelled by (♯) at 1.4 $Å^{-1}$ is defined as the mica substrate with a combination of the green line at 2.16 $Å^{-1}$ that changes to the light blue line at the end of the T-WAXS measurements. The same features are attributed to the presence of MAI. The X-ray scattering area recorded at 1.7$Å^{-1}$ is as attributed to the scattering signature of the intermediate product $MA_{x+y}PbI_{2+x}Cl_y$ [12, 4].

The changes in the width of important scattering peaks that refer to the intermediate product $MA_{x+y}PbI_{2+x}Cl_y$ and MAI during the proceeding time were plotted and are shown in **Fig 4.3.** The width of the WAXS peaks gives an estimated value of the crystal size. The wider the peaks, the smaller the size of the crystals[13]. In the measurements presented, the crystal size of the MAI and $MA_{x+y}PbI_{2+x}Cl_y$ was changed inversely, as indicated by the change in FWHM. The crystal size of the MAI started smaller and after 200s changes to bigger size which indicate converted into $MA_{x+y}PbI_{2+x}Cl_{y.}$ The bigger MAI crystals can also be attributed to MAI impurity. After 250s, the crystal size of MAI and $MA_{x+y}PbI_{2+x}Cl_y$ remains unchanged. This indicates that the conversion processes between the MAI and $MA_{x+y}PbI_{2+x}Cl_y$ occur fast during the first 3 minutes.

The dynamic formation of $MAPbI_{3-x}Cl_x$ perovskite film during the spin coating data suggested that two stages of crystal formation. The plot of the scattering intensity of the

main features related to the solvent at the centre at q=0.55 $Å^{-1}$, intermediate product $MA_{x+y}PbI_{2+x}Cl_y$ at q=1.1 $Å^{-1}$ and the scattering of MAI and mica at 1.4 $Å^{-1}$ as a function of the time is shown in **Fig 4.4.** The first stage is the solvent loss during the first min whereas after that the crystallisation stage of the intermediate product $MA_{x+y}PbI_{2+x}Cl_y$ is occurred.

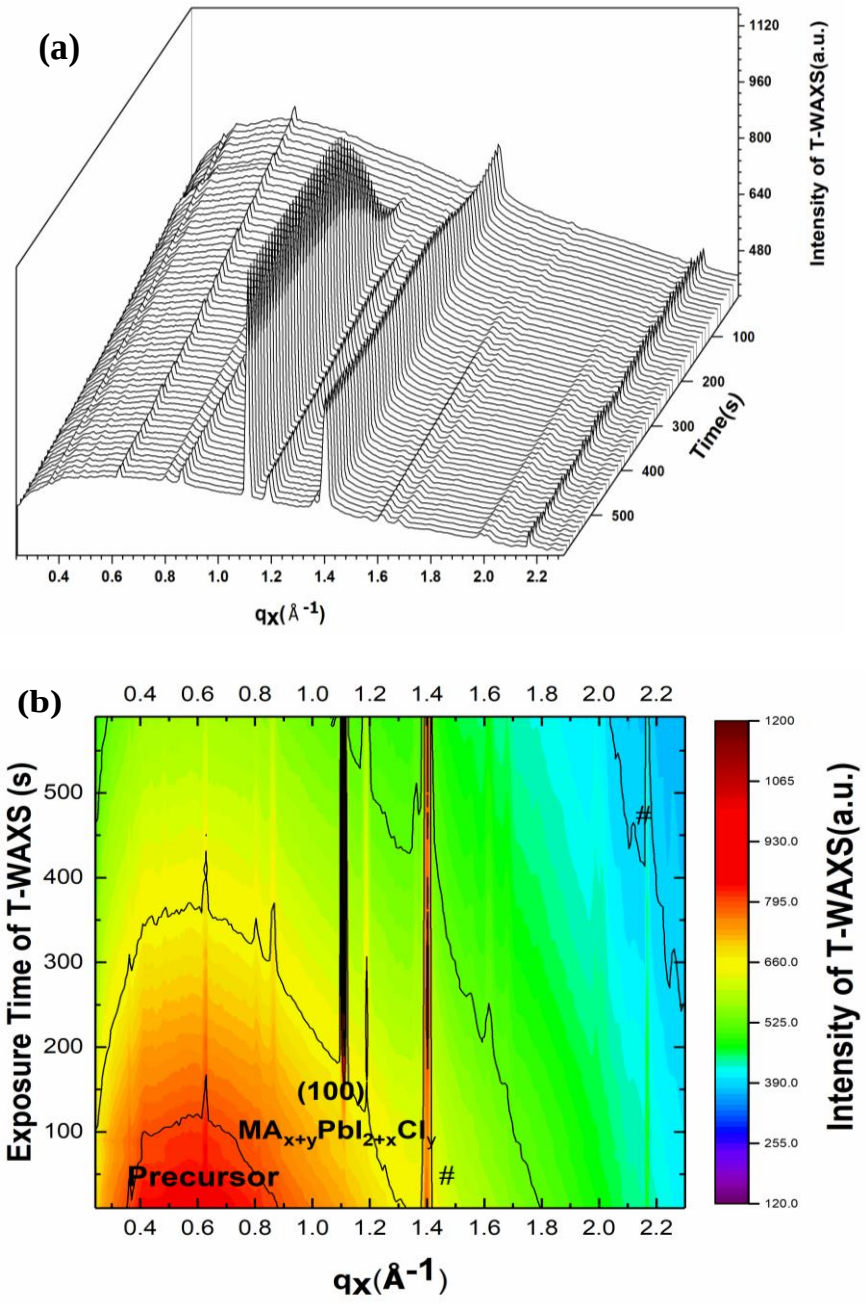

Figure 4.2 Summary of 1D of line profiles of T-WAXS of $MAPbI_{3-x}Cl_x$ precursor recorded during spin coating. (a) T-WAXS profiles as a function of exposure time of X-ray. (b) The growth evolution of the precursor during 10 min presented in a contour plot of T-WAXS intensity.

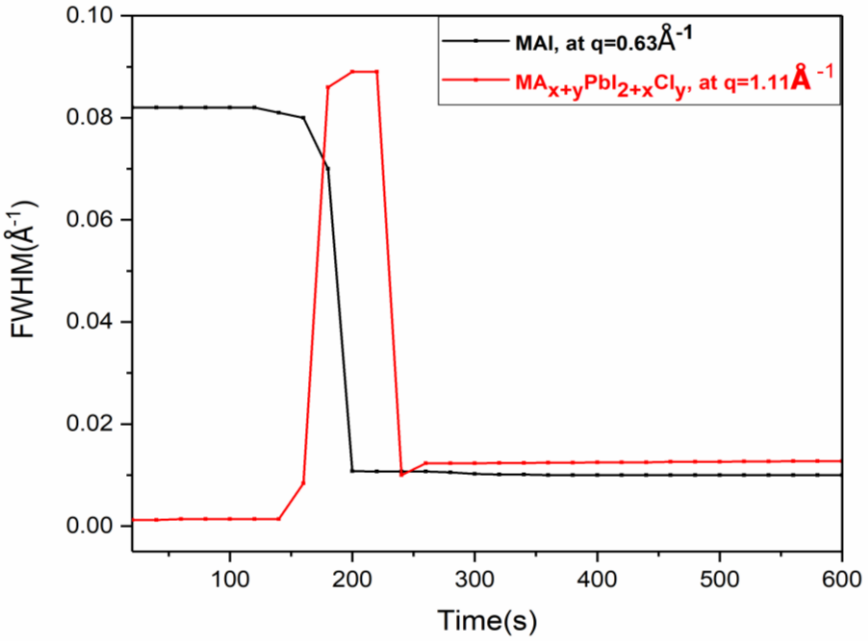

Figure 4.3: The change in FWHM of the scatterings peaks at MAI, and intermediate product $MA_{x+y}PbI_{2+x}Cl_y$ during the processing time of in situ spin coating.

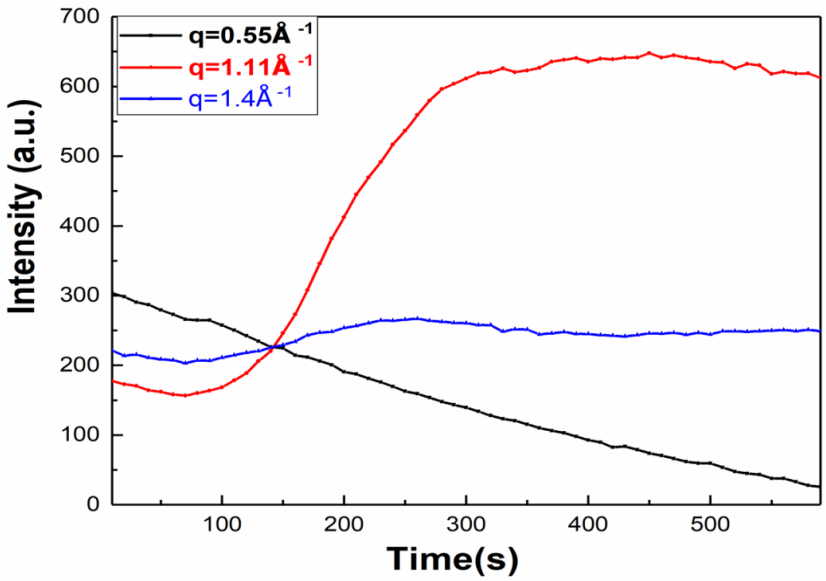

Figure 4.4: Intensity of the main features of T-WAXS of $MAPbI_{3-x}Cl_x$ perovskite film as a function of the time.

Fig 4.5 displays 2D WAXS image of the $MAPbI_{3-x}Cl_x$ film that was taken once the spinning had stopped. Some X-ray scattering spots are arranged in rings that are observed in the area between q=0.6 $Å^{-1}$ and q=1.1 $Å^{-1}$.

The multiple scattering spots observed are distributed along rings. The spots are caused by X-ray scatting from several individual crystallites at 1.1$Å^{-1}$ at (100) after solvent evaporation. If enough individual crystallites are present a continuous ring would be observed as occurs in a powder diffraction experiment. In **Fig 4.5** the spots are not preferentially distributed in any particular section of the ring. There is an equal spread around the out of plane direction, the in plane direction and all angular directions in between indicating random orientation of crystallites present. As was explained in **Chapter 3**, the full ring indicates that the crystals are orientated in random directions, including vertical and horizontal or angular directions. Based on the direction of the orientation, the combinations of X-ray group scattering signals are arranged to form scattering rings. The room temperature observation presented here is in agreement with the initial observations made in a recent *in situ* grazing incidence WAXS study, where the perovskite films were first deposited by spray coating and then dynamics measurements were taken during the annealing process [14]. Here, we observed that the high order intermediate crystallites can be formed with random orientations without any heat assistance. The X-ray scattering of completed perovskite phase, therefore, can be seen if the substrates or the perovskite ink are preheating, as was observed in [10, 14].

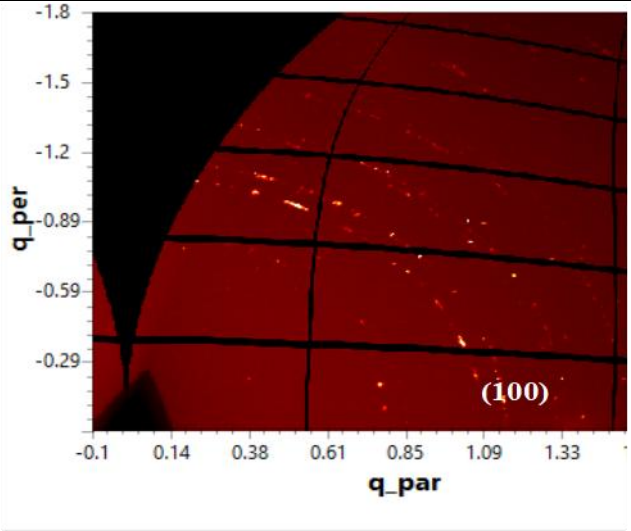

Figure 4.5: 2D T-WAXS patterns of $MAPbI_{3-x}Cl_x$ ink after the spin coating.

4.2 Crystalline Structure of Annealed $MAPbI_{3-x}Cl_x$ Film Investigated by WAXS

In **Section 4.1** it was shown that solvent evaporation assists the crystallization and formation of the intermediate product $MA_{x+y}PbI_{2+x}Cl_y$ which resulted in a WAXS signal detected at q=1.1 $Å^{-1}$. This unstable cubic structure of the intermediate phase was observed during the dynamic spin coating process at room temperature. In this section, the role of the high (90^oC) temperature in forming the full perovskite phase will be explored. Perovskite ink from the MAI and $PbCl_2$ prepared in the same method as described in **Section 3.2-1** and was deposited on mica substrates and after spin coating, the sample moved into a hot plate then was annealed at 90^o C for 2 hours and measured using WAXS techniques.

Fig. 4.6 compares the one-dimensional T-WAXS pattern of the dry film formed after spin coating and the T-WAXS pattern of the annealed film. The scattering peak correspond

into the as cast intermediate perovskite structure that was detected at 1.1 $Å^{-1}$ mostly disappears after annealing the film. This indicates instability of the intermediate perovskite structure that forms during the spin coating processes.

On the other hand, the scattering peaks are clearly visible at q=1 $Å^{-1}$ and 2 $Å^{-1}$ and did not exist after the spin coating processes. As in the previous section features at scattering vectors q = 1.4 $Å^{-1}$and 2.16 $Å^{-1}$ correspond to scattering from the mica substrate and MAI that are labelled (#) were observed.

The peaks at q=1$Å^{-1}$ and 2$Å^{-1}$ are assigned to the (110) and (220) crystal planes of the tetragonal structure in the complete $MAPbI_{3-x}Cl_x$ perovskite phase. Similar peaks have previously been observed at $2\theta = 14.1^o$ and 28.42^o which using Eq. 3.2 converted to q values of 1 $Å^{-1}$ and 2 $Å^{-1}$, as was reported in the wide angle X-ray scattering studies in the literature [15-17].

The changes observed during annealing the perovskite are attributed to a phase change occurring during thermal annealing. This process indicates a complete chemical reaction, as was explained in **Rect. 4.2**, through a conversion from the intermediate cubic structure to a more stable tetragonal structure.

In the 1D T-WAXS spectra of the annealed perovskite film shown in **Fig 4.6** weak scattering peak at q=1 $Å^{-1}$ and some weak evidence of the intermediate scattering peak remaining at q=1.1 $Å^{-1}$ were observed, which indicates the existence of a small amount of residual intermediate product and some of the precursor materials that contribute to the impurity of the perovskite films.

Fig. 4.7 illustrates a full scattering ring at q=1 $Å^{-1}$. The full rings of the X-ray scattering are apparent due to probing many smaller crystals with more random orientations so probing more orientations of crystal planes as was illustrated in **Fig. 3.2** [18]. The SEM data are confirmed this in next section.

Based on this concept, the annealed $MAPbI_{3-x}Cl_x$ film can be described as thicker films with randomly orientated crystals at q=1 $Å^{-1}$. In contrast, only some degree of orientation presented lower content of materials can be extracted from the 2D WAXS data from the dry film that formed before the thermal annealing as seen in **Fig. 4.7**. The observation of random orientations of the $MAPbI_{3-x}Cl_x$ annealed film is similar to what was highlighted previously [10, 14, 16].

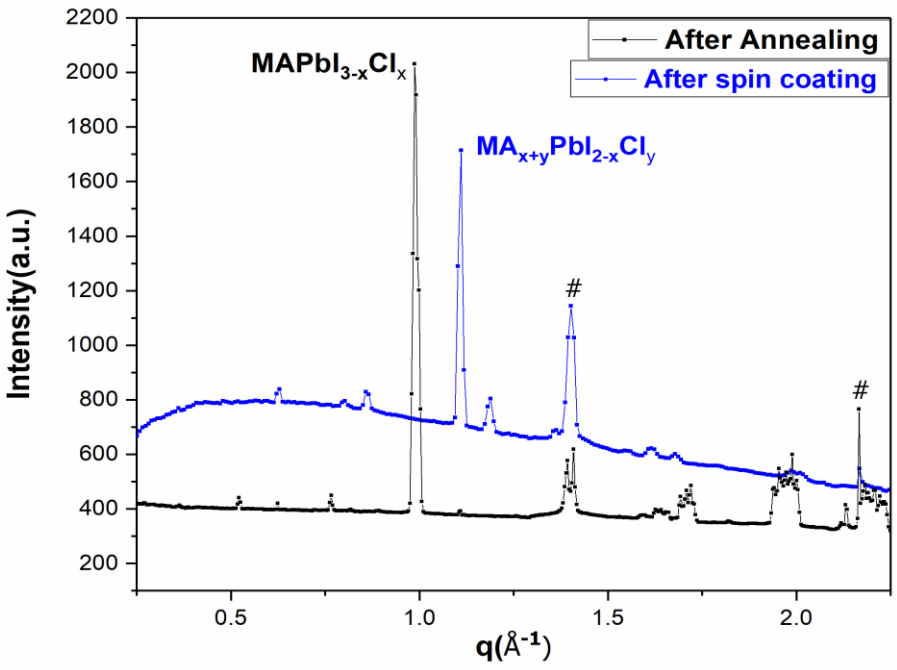

Figure 4.6: Comparison between the T-WAXS patterns of $MAPbI_{3-x}Cl_x$ after spin coating and after thermal annealing.

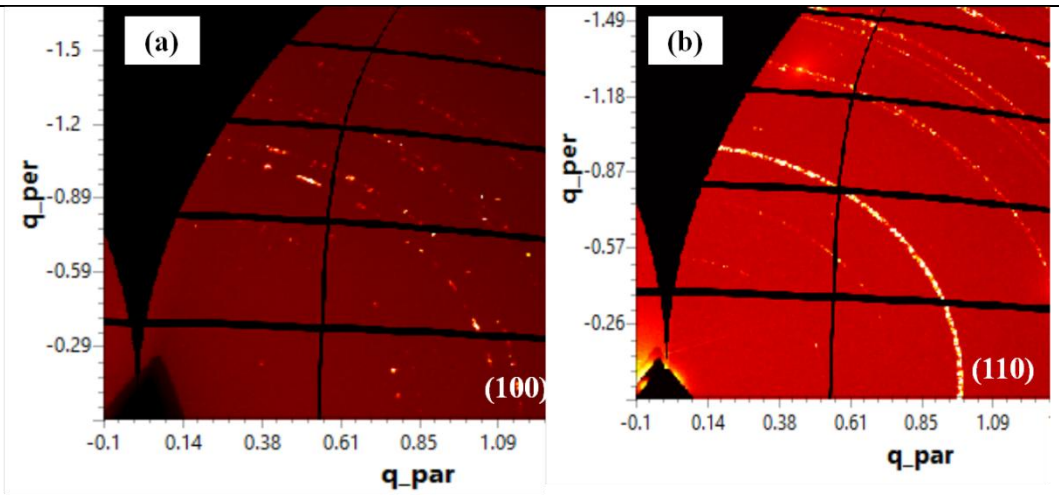

Figure 4.7: 2D T-WAXS data of $MAPbI_{3-x}Cl_x$ recorded (a) before and (b) after the thermal annealing.

4.3 Morphological Study of $MAPbI_{3-x}Cl_x$ Film

Scanning electron microscopy (SEM) was used to conduct a morphological study of the $MAPbI_{3-x}Cl_x$ perovskite film to further explore the effects of the thermal annealing. The surfaces of the $MAPbI_{3-x}Cl_x$ perovskite films before and after the thermal annealing for different annealing times were studied. **Fig. 4.8** shows images of the surface of the $MAPbI_{3-x}Cl_x$ perovskite film as a function of the annealing time in the range of 0–120 min (at 90^{o} C).

Before thermal annealing (**Fig. 4.8a)**, the surface appears cross shape crystals that most likely corresponding to the intermediate perovskite $MA_{x+y}PbI_{2+x}Cl_y$. After heating the film at 90^{o}C for half an hour (**Fig. 4.8b)** there is a subtle morphological change; the large cross shape crystals turn into a single continuous film.

As the annealing time increases from 30 min to 60 min (**Fig. 4.8c)**, the surface coverage of the film is more complete and the gaps between the crystals domains are further

reduced. The increase in the film coverage and reduction in the pinhole with the increase of film heating time is attributed to evaporating the MACl product into a gas and the initial formation of the final perovskite phase $MAPbI_3$. In other words, the chemical reaction of MAI and $PbCl_2$ is completed after 60 min of annealing as was proposed [5].

An increase in surface coverage can be seen clearly after 2 hours of annealing (**Fig. 4.8d)**, which is the recommended annealing time to form a perovskite film in air [19, 20]. The existence of a few pin holes at this annealing time is possibly due to the continued presence of a low content of un-reacted amorphous material or the intermediate phase $MA_{x+y}PbI_{2+x}Cl_y$, which was not fully converted into the final perovskite phase, thus yielding a slightly impure film containing un-reacted materials, as was also indicated in the 1D-WAXS data in **Fig. 4. 6.**

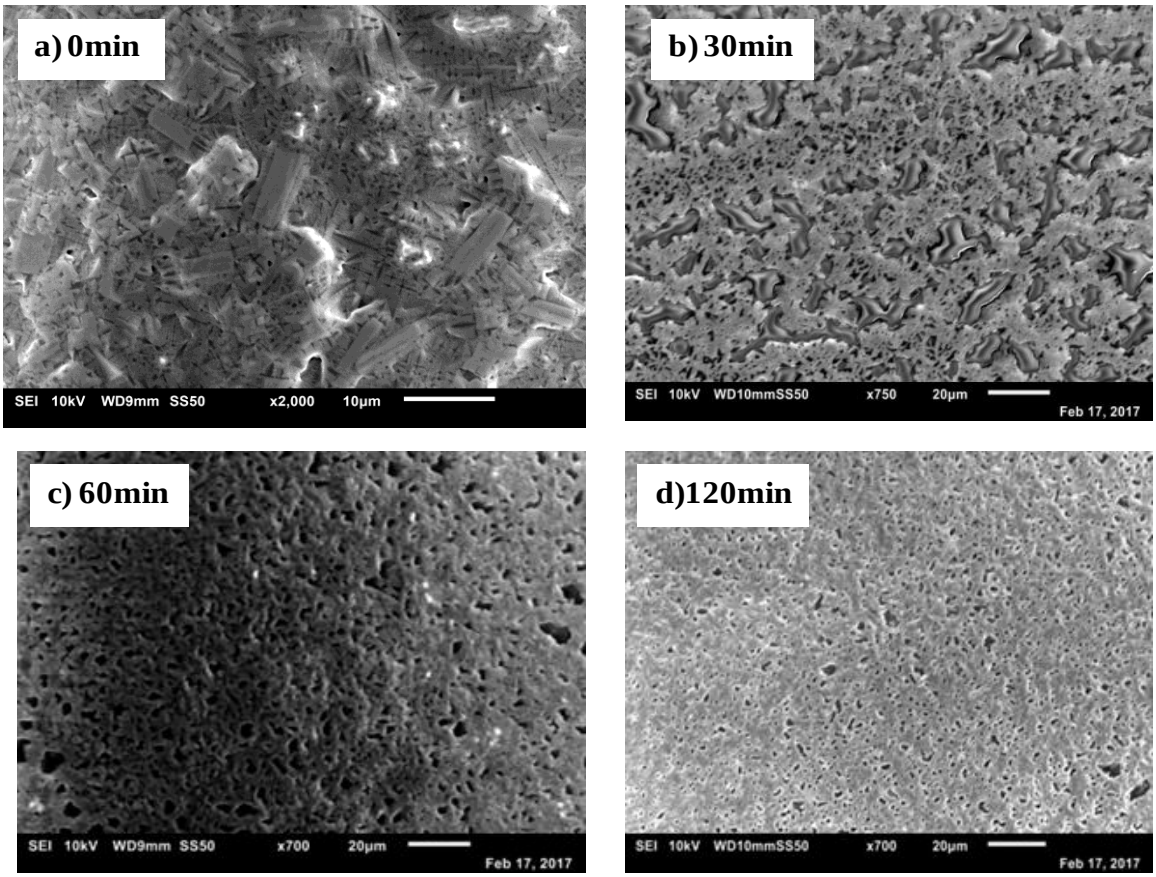

Figure 4.7: (a) Surface morphology of $MAPbI_{3-x}Cl_x$, observed by SEM directly after spin coating, (b) annealed film for 30 min, (c) 60 min, and (d) 120 min.

4.4 UV-Vis spectra of $MAPbI_{3-x}Cl_x$ Film

The optoelectronic behavior of the $MAPb_{3-x}Cl_x$ films was investigated by measuring their absorption spectra using a UV-Vis spectrometer. The inks containing MAI and $PbCl_2$ were prepared as described in **Section 3.1-1**. The ink was then deposited onto glass substrates. Three of the samples were heated to 90^o C for 30 min, 60 min and 120 min, respectively, whereas the fourth sample was measured as cast without any annealing.

The results of the light absorption spectra for the four $MAPb_{3-x}Cl_x$ samples are presented in **Fig. 4.9(a-d).** Samples (a-c) exhibit different gradients in the spectra over the visible and near IR ranges between 750 nm to 800 nm. In contrast, an almost flat absorbance line was observed in the film without any annealing in sample (d). This behaviour of the light absorption spectra is similar to what was reported from $MAPbI_{3-x}Cl_x$ previously [21, 22]. The light absorption spectra are also in the agreement with what was observed in the $MAPI_3$ perovskite film [23, 24].

The absence of the absorption edge in the perovskite sample that was prepared without annealing is due to the absence of the final perovskite crystalline phase at this stage. The surface coverage and T-WAXS data of the film as cast presented separated crystals of intermediate product $MA_{x+y}PbI_{2+x}Cl_y$ as identified in **Fig 4.8** and **Fig 4.2.**

The poor solar light absorption at these materials that would mean a lower PCE for solar cell devices made without thermal annealing.

The optical band gap for the material in the film annealed for 2 hours at 90^o C was calculated from the UV-Vis spectra by fitting a straight line to a Tauc plot and was found to be 1.55 eV (**Fig. 4.9**). This optical band gap for the $MAPbI_{3-X}Cl_X$ perovskite

semiconductor is in the range of the theoretical optimum band gap of solar cell devices that can deliver a current density of 27 mA/cm^2, as was discussed in **Chapter 2** [25, 26].

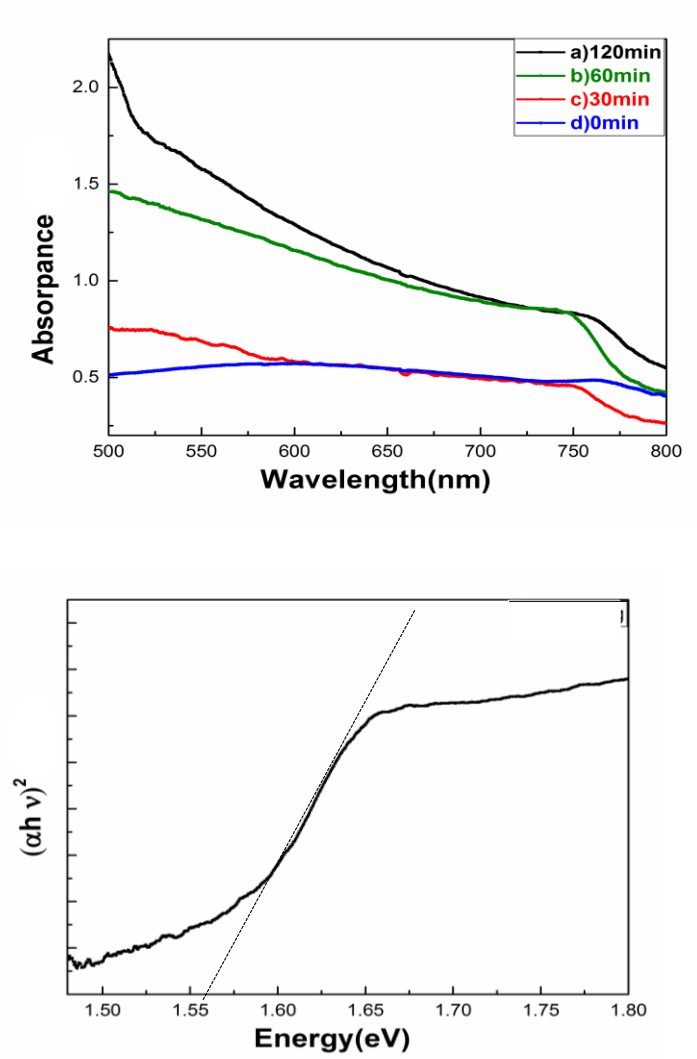

Figure 4.9: UV-Vis spectra of MAPb3-xClx perovskite annealed for (a) 2 hours, (b) 60 min, (c) 30 min, (d) annealed film, and the extracted band gap in the Tauc plot.

4.5 Air exposure effects on Annealed Film

After a perovskite ink is prepared and deposited onto the substrate and spin coated to form a film that is subsequently thermally annealed, it should be stored/used in such a

way as to prevent any damage. The storage conditions of perovskite as a film or as a photoactive layer within solar cell devices are crucial factors in determining the lifetime of perovskite solar cells.

Encapsulation is the most common way to protect the perovskite film in a solar cell to slow down its degradation. An undesirable short lifetime of the $MAPbI_{3-x}Cl_x$ perovskite materials has been reported [27, 28]. This short lifetime results from degradation of the perovskite into other chemical materials in the presence of oxygen and high humidity (more than 60%) [29].

To investigate the effect of air exposure on the crystal structure of the annealed $MAPbI_{3-x}Cl_x$ perovskite film, WAXS characterisation was used. The WAXS ring of the film before and after air exposure was obtained and is illustrated in **Fig. 4.10b, c**. The perovskite WAXS ring shows bright scattering ring of a full completed phase of $MAPbI_{3-x}Cl_x$ at q=1 $Å^{-1}$after air exposure which indicated the material degradation. This degradation can be better observed by WAXS scattering before 0.75$Å^{-1}$, which is related to the precursor materials. However, 2D WAXS data reveals the slight appearance of a visual ring at q=0.9 $Å^{-1}$ that corresponds to PbI_2.

Fig 4.10 shows the WAXS profiles of the $MAPbI_{3-x}Cl_x$ film stored in an evacuated dissector and of another nominally identical film that was exposed to air for approximately 5 hours. Radial sector integration profiles from the 2D T-WAXS scattering patterns from the $MAPbI_{3-x}Cl_x$ film after air exposure shows a relatively weaker peak intensity at the original final perovskite features associated with scattering from(110) and (220) planes at q=1 $Å^{-1}$and q=2 $Å^{-1}$, respectively (**Fig. 4.10)**. Moreover,

new features in the WAXS profiles appear as peaks at q=0.45 $Å^{-1}$, q=0.7 $Å^{-1}$ and q=0.9 $Å^{-1}$. The pre-annealing intermediate phase that is characterized by a peak at 1.1$Å^{-1}$ can be seen to have reappeared (**Fig. 4.10)**.

The reduction of WAXS intensity at q=1 $Å^{-1}$ after air exposure originates from the loss of the $MAPbI_{3-x}Cl_x$ material, which may decompose into PbI_2 that is responsible for showing the WAXS peak at q=0.9 $Å^{-1}$, as was defined previously [30]. The existence of some peaks related to the MAI content at q=0.45 $Å^{-1}$ and q=0.7 $Å^{-1}$ indicates the reverse direction of the chemical reaction between MAI and $PbCl_2$ in the presence of air.

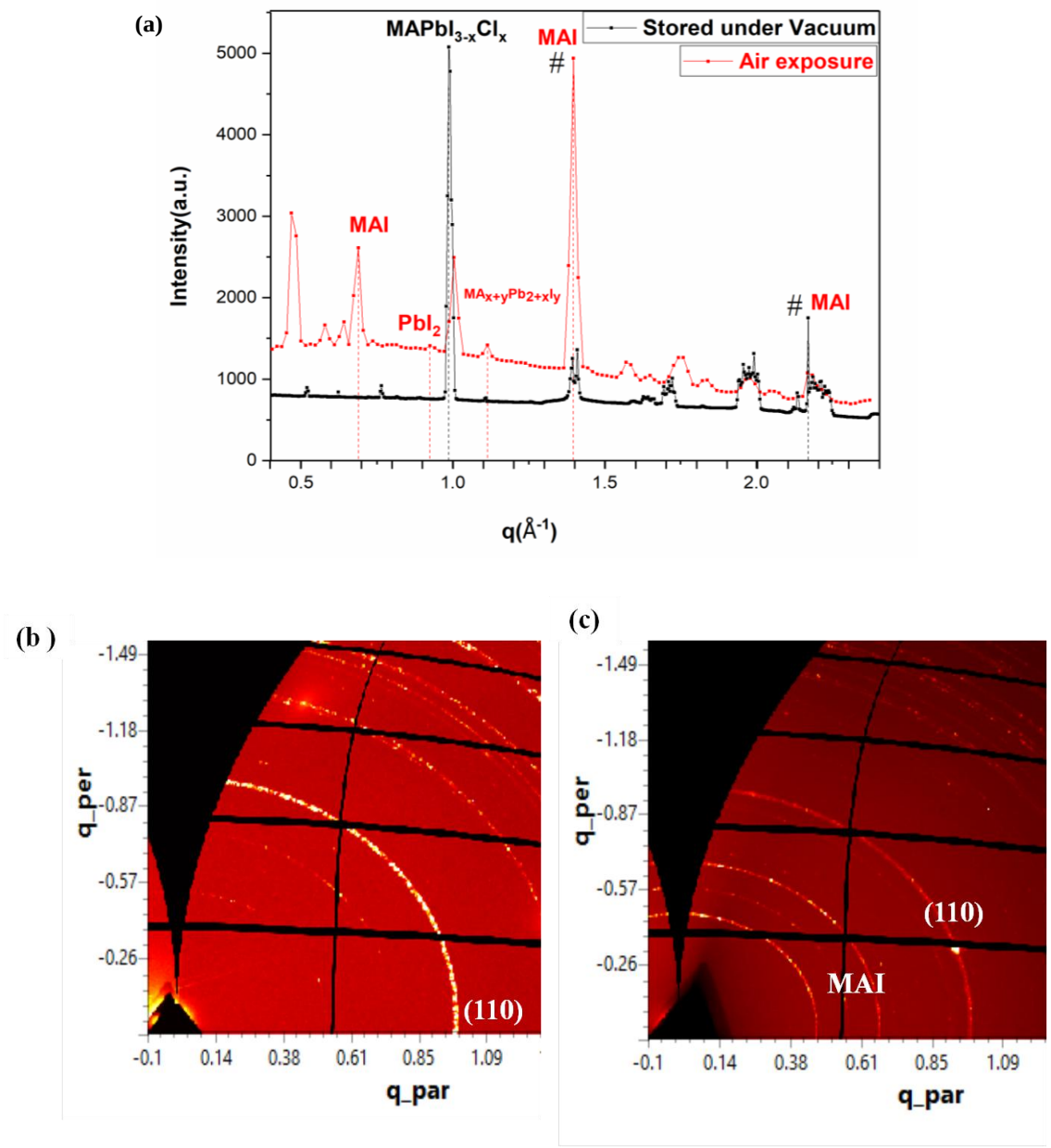

Figure 4.10: profiles of T-WAXS of annealed $MAPbI_{3-x}Cl_x$ film stored in a vacuum and in the air (a); and 2D WAXS of the same films that are stored in a (b) vacuum and in the air (c).

To better understand the change in the crystal structure of $MAPbI_{3-x}Cl_x$ film after air exposure, these observations in the crystalline structure of the $MAPbI_{3-x}Cl_x$ that was prepared under ambient conditions suggest that the $MAPbI_{3-x}Cl_x$ film should be stored under vacuum conditions to prevent any rapid degradation.

4.6 Summary

In this chapter, perovskite materials prepared by mixing MAI and $PbCl_2$ in a 3:1 molar ratio and dissolved in a DMF solvent were investigated.

The final perovskite phase desirable for solar cell applications was achieved after annealing at 90^o C. Forming this phase that was observed by X-ray scatter at the (110) and (220) and crystal formed slowly. Therefore, a longer time for annealing was required, exceeding 2 hours. Annealing for a longer time can also assist in forming better coverage and fewer pinholes that are reflected in the performance of perovskite solar devices. In terms of solar light absorption, an enhancement was observed in the UV-Vis spectra resulting from the complete reaction after annealing the film for 2 hours.

This chapter also discusses the impact of the storage method of the film on the crystal structure of $MAPbI_{3-x}Cl_x$ and its orientation. The remarkable degradation into the precursor materials was observed in the film that was stored in humid air for 5 hours, and a change in the crystal orientation was observed as well. Therefore, after preparing the $MAPbI_{3-x}Cl_x$ materials in air, the material should be stored under vacuum conditions or at least with minimal exposure time to the air to guarantee a prolonged lifetime of the $MAPbI_{3-x}Cl_x$ films which will enhance the lifetime of perovskite solar cell devices.

4.7 References

1. Huang, Y.-C., C.-S. Tsao, Y.-J. Cho, K.-C. Chen, K.-M. Chiang, S.-Y. Hsiao, C.-W. Chen, C.-J. Su, U.-S. Jeng, and H.-W. Lin, Insight into Evolution, Processing and Performance of Multi-length-scale Structures in Planar Heterojunction Perovskite Solar Cells. Scientific reports, 2015. **5**: p. 13657.

2. Tan, K.W., D.T. Moore, M. Saliba, H. Sai, L.A. Estroff, T. Hanrath, H.J. Snaith, and U. Wiesner, Thermally induced structural evolution and performance of mesoporous block copolymer-directed alumina perovskite solar cells. Acs Nano, 2014.

3. Unger, E.L., A.R. Bowring, C.J. Tassone, V.L. Pool, A. Gold-Parker, R. Cheacharoen, K.H. Stone, E.T. Hoke, M.F. Toney, and M.D. McGehee, Chloride in lead chloride-derived organo-metal halides for perovskite-absorber solar cells. Chemistry of Materials, 2014. **26**(24): p. 7158-7165.

4. Zhou, H., Q. Chen, G. Li, S. Luo, T.-b. Song, H.-S. Duan, Z. Hong, J. You, Y. Liu, and Y. Yang, Interface engineering of highly efficient perovskite solar cells. Science, 2014. **345**(6196): p. 542-546.

5. Yu, H., F. Wang, F. Xie, W. Li, J. Chen, and N. Zhao, The Role of Chlorine in the Formation Process of “CH3NH3PbI3-xClx” Perovskite. Advanced Functional Materials, 2014. **24**(45): p. 7102-7108.

6. Chang, C.-Y., Y.-C. Huang, C.-S. Tsao, and W.-F. Su, Formation Mechanism and Control of Perovskite Films from Solution to Crystalline Phase Studied by in Situ Synchrotron Scattering. ACS applied materials & interfaces, 2016. **8**(40): p. 26712-26721.

7. Colella, S., E. Mosconi, P. Fedeli, A. Listorti, A. Rizzo, F. Gazza, F. Orlandi, P. Ferro, T. Besagni, and G. Calestani, MAPbI 3-x Cl x mixed halide perovskite for hybrid solar cells: the role of chloride as dopant on the transport and structural properties. MRS Online Proceedings Library Archive, 2014. **1667**.

8. Poglitsch, A. and D. Weber, Dynamic disorder in methylammoniumtrihalogenoplumbates (II) observed by millimeter-wave spectroscopy. The Journal of chemical physics, 1987. **87**(11): p. 6373-6378.

9. Mosconi, E., A. Amat, M.K. Nazeeruddin, M. Grätzel, and F. De Angelis, First-Principles Modeling of Mixed Halide Organometal Perovskites for Photovoltaic Applications. The Journal of Physical Chemistry C, 2013. **117**(27): p. 13902-13913.

10. Barrows, A.T., S. Lilliu, A.J. Pearson, D. Babonneau, A.D. Dunbar, and D.G. Lidzey, Monitoring the Formation of a CH3NH3PbI3–xClx Perovskite during Thermal Annealing Using X-Ray Scattering. Advanced Functional Materials, 2016. **26**(27): p. 4934-4942.

11. Jeon, N.J., J.H. Noh, Y.C. Kim, W.S. Yang, S. Ryu, and S.I. Seok, Solvent engineering for high-performance inorganic–organic hybrid perovskite solar cells. Nature materials, 2014. **13**(9): p. 897-903.

12. Liu, J., C. Gao, X. He, Q. Ye, L. Ouyang, D. Zhuang, C. Liao, J. Mei, and W. Lau, Improved crystallization of perovskite films by optimized solvent annealing for high efficiency solar cell. ACS applied materials & interfaces, 2015. **7**(43): p. 24008-24015.

13. Scherrer, P., Estimation of the size and internal structure of colloidal particles by means of röntgen. Nachr. Ges. Wiss. Göttingen, 1918. **2**: p. 96-100.

14. Lilliu, S., J. Griffin, A. Barrows, M. Alsari, B. Curzadd, T. Dane, O. Bikondoa, J.E. Macdonald, and D. Lidzey, Grain rotation and lattice deformation during

perovskite spray coating and annealing probed in situ by GI-WAXS. CrystEngComm, 2016. **18**(29): p. 5448-5455.

15. Liu, M., M.B. Johnston, and H.J. Snaith, Efficient planar heterojunction perovskite solar cells by vapour deposition. Nature, 2013. **501**(7467): p. 395-398.
16. Miyadera, T., Y. Shibata, T. Koganezawa, T.N. Murakami, T. Sugita, N. Tanigaki, and M. Chikamatsu, Crystallization Dynamics of Organolead Halide Perovskite by Real-Time X-ray Diffraction. Nano letters, 2015. **15**(8): p. 5630-5634.
17. Wang, Z.K., M. Li, Y.G. Yang, Y. Hu, H. Ma, X.Y. Gao, and L.S. Liao, High Efficiency Pb–In Binary Metal Perovskite Solar Cells. Advanced Materials, 2016. **28**(31): p. 6695-6703.
18. Müller-Buschbaum, P., The active layer morphology of organic solar cells probed with grazing incidence scattering techniques. Advanced Materials, 2014. **26**(46): p. 7692-7709.
19. Ahmadian-Yazdi, M.R., F. Zabihi, M. Habibi, and M. Eslamian, Effects of Process Parameters on the Characteristics of Mixed-Halide Perovskite Solar Cells Fabricated by One-Step and Two-Step Sequential Coating. Nanoscale Research Letters, 2016. **11**(1): p. 408.
20. Kim, J.H., S.T. Williams, N. Cho, C.C. Chueh, and A.K.Y. Jen, Enhanced Environmental Stability of Planar Heterojunction Perovskite Solar Cells Based on Blade-Coating. Advanced Energy Materials, 2015. **5**(4).

21. D'innocenzo, V., G. Grancini, M.J. Alcocer, A.R.S. Kandada, S.D. Stranks, M.M. Lee, G. Lanzani, H.J. Snaith, and A. Petrozza, Excitons versus free charges in organo-lead tri-halide perovskites. Nature communications, 2014. **5**: p. 3586.

22. Lee, M.M., J. Teuscher, T. Miyasaka, T.N. Murakami, and H.J. Snaith, Efficient Hybrid Solar Cells Based on Meso-Superstructured Organometal Halide Perovskites. Science, 2012. **338**(6107): p. 643-647.

23. Kazim, S., M.K. Nazeeruddin, M. Grätzel, and S. Ahmad, Perovskite as light harvester: a game changer in photovoltaics. Angewandte Chemie International Edition, 2014. **53**(11): p. 2812-2824.

24. Sakai, N., S. Pathak, H.-W. Chen, A.A. Haghighirad, S.D. Stranks, T. Miyasaka, and H.J. Snaith, The mechanism of toluene-assisted crystallization of organic–inorganic perovskites for highly efficient solar cells. Journal of Materials Chemistry A, 2016. **4**(12): p. 4464-4471.

25. Green, M.A., A. Ho-Baillie, and H.J. Snaith, The emergence of perovskite solar cells. Nature Photonics, 2014. **8**(7): p. 506-514.

26. Shockley, W. and H.J. Queisser, Detailed balance limit of efficiency of p-n junction solar cells. Journal of applied physics, 1961. **32**(3): p. 510-519.

27. Luo, S. and W.A. Daoud, Recent progress in organic-inorganic halide perovskite solar cells: mechanisms and material design. Journal of Materials Chemistry A, 2015. **3**(17): p. 8992-9010.

28. Niu, G., X. Guo, and L. Wang, Review of recent progress in chemical stability of perovskite solar cells. Journal of Materials Chemistry A, 2015. **3**(17): p. 8970-8980.

29. Niu, G., W. Li, F. Meng, L. Wang, H. Dong, and Y. Qiu, Study on the stability of CH 3 NH 3 PbI 3 films and the effect of post-modification by aluminum oxide in all-solid-state hybrid solar cells. Journal of Materials Chemistry A, 2014. **2**(3): p. 705-710.

30. Guo, X., C. McCleese, C. Kolodziej, A.C. Samia, Y. Zhao, and C. Burda, Identification and characterization of the intermediate phase in hybrid organic–inorganic MAPbI 3 perovskite. Dalton Transactions, 2016. **45**(9): p. 3806-3813.

Chapter 5: The Dynamics of $FAPbI_{3-x}Cl_x$ Perovskite Films Crystallization

In the previous chapter the crystal structure of the most widely used perovskite material $MAPbI_{3-x}Cl_x$ was investigated during *in situ* spin coating by T-WAXS and *ex situ* after thermal annealing. Using the same technique, $FAPbI_{3-x}Cl_x$ perovskite film will be investigated in this chapter.

The results of the T-WAXS collected during spin coating are detailed in **Section 5.1.** In **Section 5.2-1** the effects of different annealing temperatures and times on the quality of crystalline film $FAPbI_{3-x}Cl_x$ will be demonstrated. The morphology study of these different annealing conditions of $FAPbI_{3-x}Cl_x$ films will be illustrated in **Section 5.2-2** .The main difference between T-WAXS features of the annealed film and the just coated film is highlighted in **Section 5.2-3**. Measurement of changes to the T-WAXS profiles for a long time (9h) after deposition is explored to study the degradation of $FAPbI_{3-x}Cl_x$ perovskite film in **Section 5.2.4.**

Measurements of UV-Vis spectra and the optical band gap are discussed in **Section 5.3**. Finally, the main findings will be highlighted in the chapter's conclusion in **Section 5.4.**

5.1 T-WAXS experiments during *in-situ* spin coating of the solution to produce $FAPbI_{3-x}Cl_x$ perovskite films

The perovskite ink prepared by mixing FAI and lead chloride as described in **Chapter 3** in **Section 3.1** was investigated during spin coating to understand the formation mechanisms of the crystalline products. **Fig 5.1** presents the T-WAXS data of the

solutions used to produce perovskite during the first ten minutes of the spin casting process. **Fig 5.1(a)** shows the time dependent measurement of T-WAXS radial profiles of perovskite ink. During the first six minutes of the T-WAXS collection, The broad solvent related feature is present initially and slowly disappears and the dominant feature that can be detected is a peak around q=1.4 $Å^{-1}$. This T-WAXS peak, as was discussed in **Chapter 4**, is attributed to scattering from the mica substrates on which the perovskite inks were deposited. As the processing time increased, some features eventually form in the T-WAXS profiles at 330 s indicating the initial stage of formation of the intermediate products of $FAPbI_{3-x}Cl_x$.

T-WAXS peaks at q=1.4 $Å^{-1}$is also attributed the present of $PbCl_2$ in agreement with the XRD data of the individual measurements of $PbCl_2$ [1, 2]. The clear and gradual enhancement in the T-WAXS intensity of X-ray scattering signals at 0.7 $Å^{-1}$ and 1.1 $Å^{-1}$ and several other weak peaks over time indicates that these peaks are related to materials that crystalize on the surface of the substrate as the solvent evaporates over time.

The T-WAXS peaks at 0.7 $Å^{-1}$, 1.3 $Å^{-1}$, 1.6 $Å^{-1}$, 1.8 $Å^{-1}$and 2.3 $Å^{-1}$are attributed to the presence of the hexagonal structure of yellow-perovskite phase of δ-$FAPbI_3$, as was reported in X-ray diffraction results using a Cu Kα X-ray radiation source with λ=1.54 Å in [2, 3].

The T-WAXS signal at 1.1 $Å^{-1}$ is equivalent to the X-ray diffraction angle of 15.3^o (for Cu K_α) that was reported and is attributed to FACl[4]. Therefore, the X-ray scattering peak at 1.1 $Å^{-1}$ is defined as scattering caused by the intermediate product FACl.

To determine the formation time and the degree of T-WAXS intensity of each phase or product, the colour intensity map plot of T-WAXS profiles of perovskite ink during the spin coating is provided in **Fig5.1 (b)**. A higher intensity degree of X-ray scattering is represented early at 330 s at q=0.7 $Å^{-1}$, where the slower crystallization of FACl is represented by the weaker line at q=1.1 $Å^{-1}$.

The intensity map of T-WAXS profiles of perovskite ink drying shows several features of X-ray scattering and the lines may be divided into different materials. The first area shows a noticeable background X-ray scattering detected between 0.4 $Å^{-1}$and0.8 $Å^{-1}$which is attributed to the background scattering from the solvent within the mixture of $PbCl_2$ and FAI. This area exhibits a gradual decrease in the T-WAXS intensity during the spin coating time and was less pronounced after t=330 s when the solvent will have nearly finished evaporating.

As the exposure time of T-WAXS increased after 330 s, the yellow $FAPbI_3$ phase formed, as revealed by the dark red line and labelled by (δ) centred at q=0.7 $Å^{-1}$. The weaker X-ray scattering detected at 1.3 $Å^{-1}$, 1.6 $Å^{-1}$,1.8 $Å^{-1}$ and 2.3 $Å^{-1}$ are also attributed to δ-$FAPbI_3$ [5].

The intermediate phase, labelled by (♦), is associated with FACl as was reported before [4] . This intermediate product is defined by strong X-ray scattering, but not as strong as the yellow phase δ-$FAPbI_3$. A slower crystallization mechanism for FACl as compared to δ-$FAPbI_3$ is observed, it took 420 s for it to appear compared to 330 s.

At the end of the drying time of solvent, the initial stage of perovskite phase of $FAPbI_{3-x}Cl_x$ are detected at q=1 $Å^{-1}$ and q=2 $Å^{-1}$. These features agreed with the values for Bragg diffraction angle of 14.5^o and 28^o previously reported [4, 2].

A summary of the most important T-WAXS features during the spin coating and the appearance's times are provided in **Table 5.1**.

In **Fig 5.2**, the FMHW of the X-ray scattering peaks that are defined in Fig 5.1 is plotted as a function of the time. The crystals start to grow after 250s which is the slower crystallisation compared to perovskite ink containing MAI and PbCl2. Wider peaks of the complete perovskite crystal mean a smaller size compared to the discontinuous phase and hexagonal yellow perovskite crystals. In contrast, the intermediate perovskite including FACl and δ-FAPbI3 records larger size. Despite that direct growth of the FAPbI3 crystal at the spin coating, the larger intermediate crystals are not decomposed. This could indicate the need for the high temperature to complete the chemical reaction to produce the larger perovskite crystals and decompose the larger intermediate crystals.

Overall, based on the *in situ* T-WAXS profiles collected during the spin coating and crystallization of the perovskite ink containing FAI and $PbCl_2$ can be divided into three stages. The first stage involves background scattering of the solvent with the mixture of $PbCl_2$ and FAI that is lost gradually. The next stage of crystallization is associated with the dry film and is dominated primarily by yellow phase δ-$FAPbI_3$ forming at 330 s. The intermediate product of FACl appears in the third stage after 420 s. Simultaneously, the forming of a lower content (compared to the δ-$FAPbI_3$) of tetragonal perovskite crystals at q=1Å is noted. The three stage of crystals formation are illustrated in **Fig 5.3,** where

the intensity of these scattering products is plotted against the processing time. The converting from the intermediate phase FACl to the perovskite phase $FAPbI_{3-x}Cl_x$ is defined between 420 s and 440 s.

The direct forming of $FAPbI_{3-x}Cl_x$ perovskite phase during the spin coating is the distinguishing feature in this measurement whereas, in the observation of *in situ* spin coating of $MAPbI_{3-x}Cl_x$ film, only crystals of intermediate products were formed indicated two stages of crystal formations.

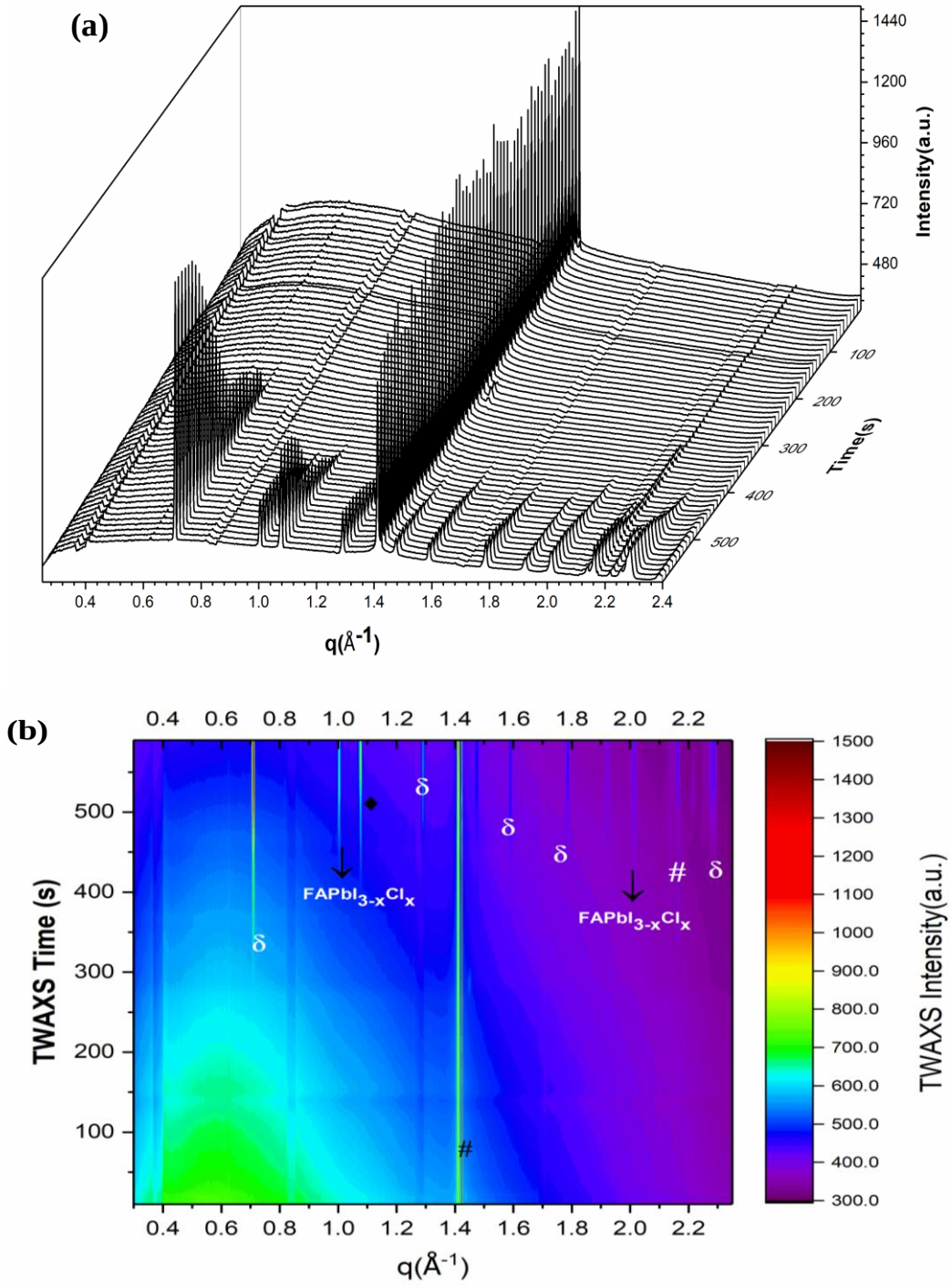

Figure 5.1: Summary of profiles of T-WAXS of $FAPbI_{3-x}Cl_x$ precursor recorded during spin coating. (a) T-WAXS profiles as a function of processing time. (b) The growth evolution of the precursor over duration of 10 min., presented in colour map of T-WAXS intensity.

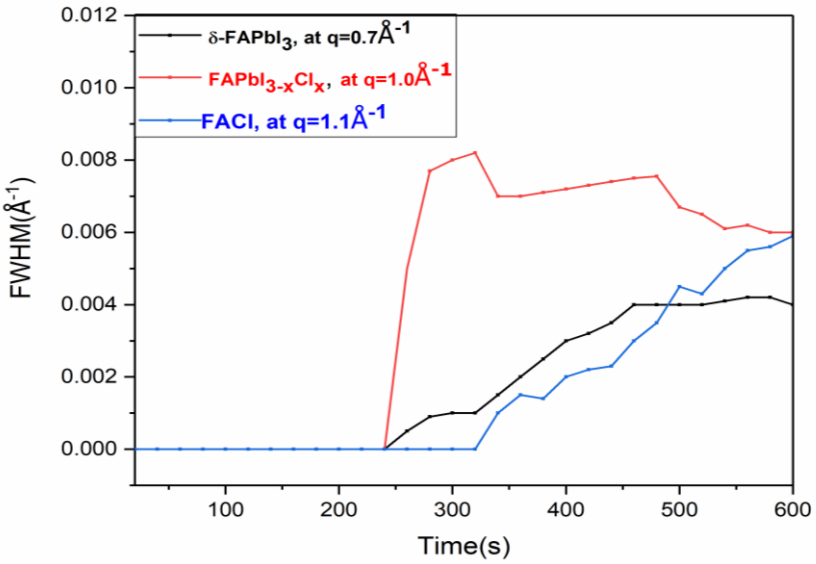

Figure 5.2: Variation in FWHM of intermediate phase δ-$FAPbI_3$, FACl at q=1.1Å^{-1} peaks and the scattering peak of perovskite crystal at FAPbI3-xCl_x as a function of the time.

Presented Materials	**X-ray scattering vectors (Å^{-1})**	**Forming Time (s)**
Solvent+($PbCl_2$ +FAI)	0.6	From t=0 to t=330
δ–$FAPbI_3$	0.7, 1.3,1.6,1.8,2.3	From 330s to the end
FACl	1.1	After 420s
$FAPbI_{3-x}Cl_x$	1.0	After420s

Table5.3 Summary of the X-ray scattering areas and the estimated starting time for formation, during the spin coating of perovskite ink of (DMF solvent with $PbCl_2$+FAI)

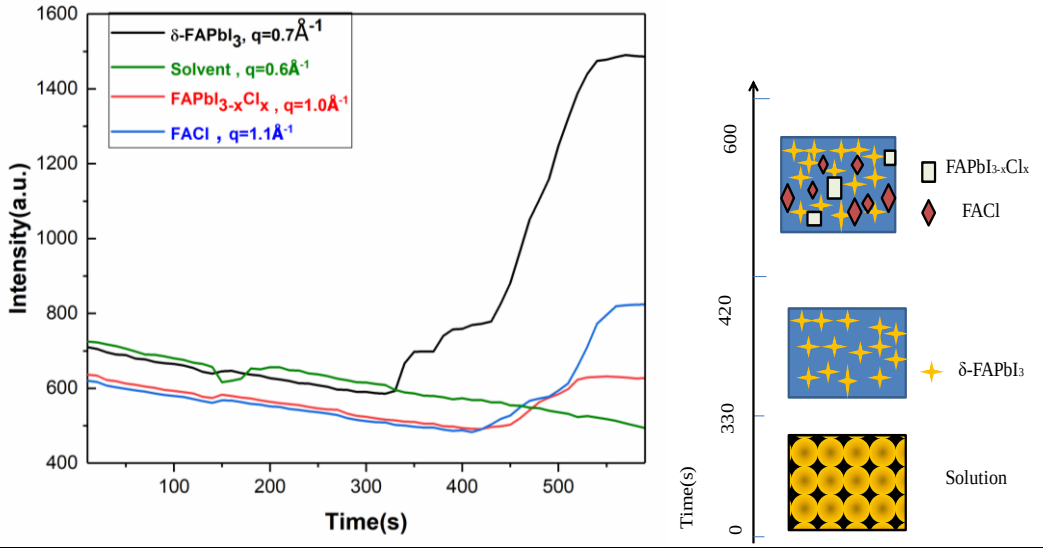

Figure 5.3: Intensity of the solvent background scattering at q=0.6 $Å^{-1}$, the δ-phase at q=0.7$Å^{-1}$, intermediate product of FACl at q=1.1 $Å^{-1}$ and perovskite phase $FAPbI_{3-x}Cl_x$ at 1 $Å^{-1}$ with sketch illustrate the forming stages.

5.2The Effects of Thermal Annealing on Crystallization of $FAPbI_{3-x}Cl_x$ Perovskite films

Several X-ray scatting peaks were observed during spin coating that are associated with the yellow perovskite δ-$FAPbI_3$ with hexagonal structure, the chloride doping owing to the presence of FACl, and lower content of $FAPbI_{3-x}Cl_x$ perovskite crystals that all appeared before any annealing. The next section will discuss the crystalline structure of perovskite after thermal annealing.

5.2-1 Thermal Annealing Conditions of $FAPbI_{3-x}Cl_x$ Film

The effects of different annealing temperatures and times on the crystalline structure of $FAPbI_{3-x}Cl_x$ film were investigated by grazing incidence wide angle X-ray scattering GI-WAXS. The geometry of the X-ray scattering experiments used here are quite different to the T-WAXS experiments already presented in **Chapter3**, further details are available in

the methods **Section 3.3-2**. Samples of $FAPbI_{3-x}Cl_x$ were spin coated and annealed inside a nitrogen filled glove box to minimize affects of moisture and humidity exposure. The most crucial difference in the GI-WAXS experiment is the ability to use very small incident X-ray angles that detect only the surface of the film. Therefore, transparent substrates are not long required; in this work Si substrates (with a native oxide) were used. As was detailed in the experimental methods in **Chapter 3**, the ranges of the incident angles (α_i) used were from 0.1^o to 0.6^o, with a step size of 0.02^o.

The intensity of the collected X-ray signals varied based on the incident angles (α_i). In order to evaluate the angle used to detect the higher intensity signals that is called the critical angle, we plotted the intensity of the significant features at q=1 $Å^{-1}$ and q=2 $Å^{-1}$ of the film against the incident angles (α_i) in **Fig 5.4.** The maximum intensity collected at $\alpha_i=0.26^o$ and this curve is similar to what was reported before in GI-WAXS experiments [6, 7]. However, there are some similar features at 1.5^o and near 3^o that are likely due to the roughness of the surface. The surface of the $FAPbI_{3-x}Cl_x$ perovskite films is not flat as is illustrated by the SEM measurements in the next section. This roughness makes it difficult to define the precise grazing incidence angle in the GI-WAXS experiments. **Fig 5.5** compares an ideal flat sample and our perovskite sample. However, the maximum intensity collected was on average at 0.26^o which was defined as the critical angle. GI-WAXS data collected at angles below this angle are assumed to be mostly from the higher layer of the surface where most of the beam is reflected. Above this angle, the beam propagates the whole depth of the film.

GIWAXS profiles at X-ray incident angle of 0.26^o for the $FAPbI_{3-x}Cl_x$ films annealed at 130^oC, 170°C and 190^oC and one without annealing are plotted in **Fig 5.6** for

comparison. The sample annealed at 130^{o}C has similar features as the sample that was not annealed, but with lower scattering intensity. The extra peak shown **Fig 5.6(b)** at q ≈ 0.9 Å^{-1} is most likely due to the presence of PbI_2 [2]. This feature is implying the initial thermal stage needs to intermediate forming to the final stage of perovskite phase.

Fig 5.6 (a) and **(b)** provide profiles that are mostly defined by presence of the yellow phase of δ-$FAPbI_3$ at scattering vectors 0.7 Å^{-1}, 1.3 Å^{-1}, 1.5 Å^{-1}, 1.8 Å^{-1}, 2.3 Å^{-1}. The intermediate products FACl at scattering vectors 1.1 Å^{-1} and 2.2 Å^{-1}, and this was also confirmed by room temperature *in-situ* T-WAXS data, as shown in **Fig 5.1**. However, the higher intensity of FACl indicates the higher content of FACl that observed in **Fig 5.6** could depend on the sample preparation conditions.

Fig 5.6(c, d) shows the GI-WAXS profiles related to higher temperature annealing at 170^{o}C and 190^{o}C degrees, at which the film is distinguished by the preferable complete perovskite phase having scattering peaks at q=1.0 Å^{-1}and q=2.0 Å^{-1}. This indicates the need of an annealing temperature higher than 130^{o}C to form the desired tetragonal crystalline structure of perovskite. Despite the similarity in GI-WAXS profiles in **Fig5.5(c, d)**, some weaker GI-WAXS peaks observed at 0.9 Å^{-1} that could originate from the PbI_2 or δ-$FAPbI_3$. These completely disappear at 190^{o}C.

All the characterised $FAPbI_{3-x}Cl_x$ films in **Fig 5.5** were annealed for 30 minutes. Longer or shorter annealing times could make a difference in film formation so to further investigate the significance of different annealing times we annealed films of $FAPbI_{3-x}Cl_x$ to 170^{o}C for 15, 30, and 60 min. The GI-WAXS profiles of these films and an un-annealed sample profile are presented in **Fig 5.6.**

After annealing for only 15 minutes, the X-ray scattering pattern of the $FAPbI_{3-x}Cl_x$ film changes. Clearly, this time was sufficient to remove the thermally decompose the FACl, as indicated by the absence of the scattering peaks at 1.1 $Å^{-1}$ and 2.2 $Å^{-1}$ in **Fig 5.6 (b).** The visible weak scattering signals recorded at 0.99$Å^{-1}$ and 2.0$Å^{-1}$ indicates the initial forming stage of tetragonal perovskite $FAPbI_{3-x}Cl_x$ crystals. In connection with T-WAXS data shown in **Fig 5.1** at room temperature for ten minutes processing time, we can observe the fast crystallisation of the perovskite phase of $FAPbI_{3-x}Cl_x$. Beside the weaker feature that relates to the perovskite phase, there is also peaks at0.86 $Å^{-1}$ and 1.9 $Å^{-1}$ that is most likely are most attributed to the lead existence in the sample.

The longer annealing times of 30 and 60 min enhance the perovskite crystallisation leading to X-ray scattering at q=1.0 $Å^{-1}$ and q=2.0 $Å^{-1}$as is illustrated in **Fig 5.7(c,d).**

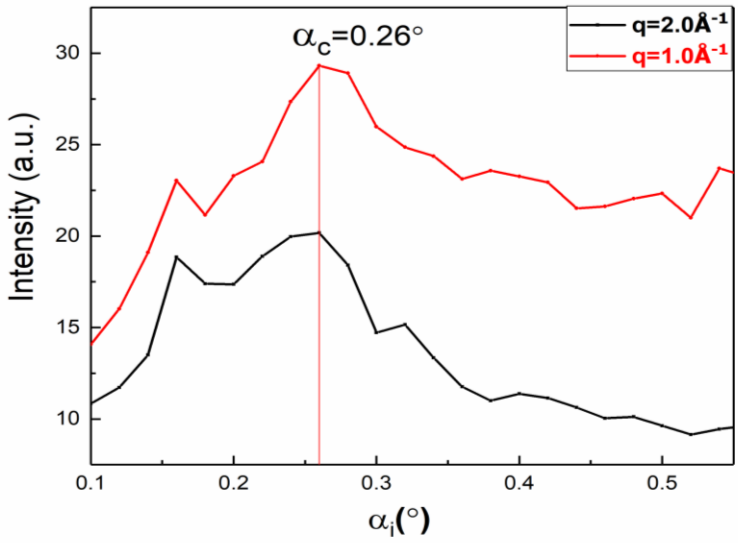

Figure 5.4: The intensity of the perovskite related features in the GI-WAXS data at q=1$Å^{-1}$ and q=2$Å^{-1}$ plotted as a function of the grazing incidence angle. The maxima intensity reflected of GI-WAXS at 0.26º.

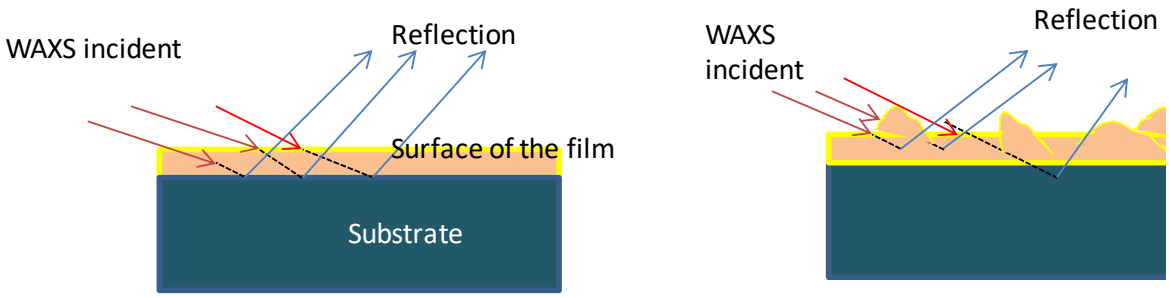

Figure 5.5: The effect the roughness of the film surface on the WAXS intensity where the directions of the reflected beam can be seen in the rough sample.

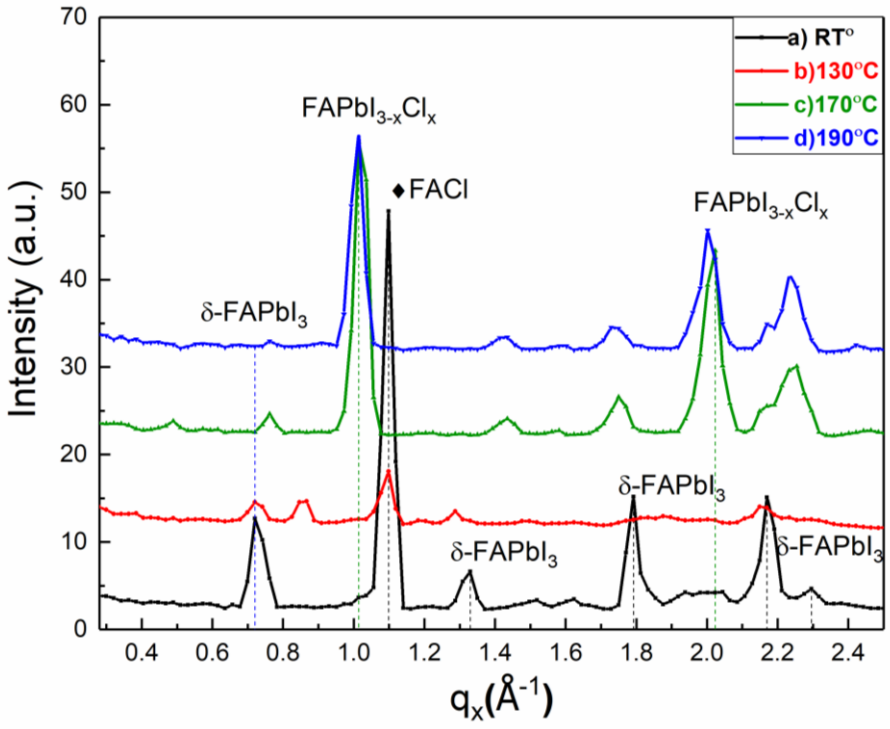

Figure 5.6 GI-WAXS patterns of $FAPbI_{3-x}Cl_X$ perovskite prepared at room temperature, RT (a), and annealed at 130°C (b), 170°C (c) and 190°C (d).

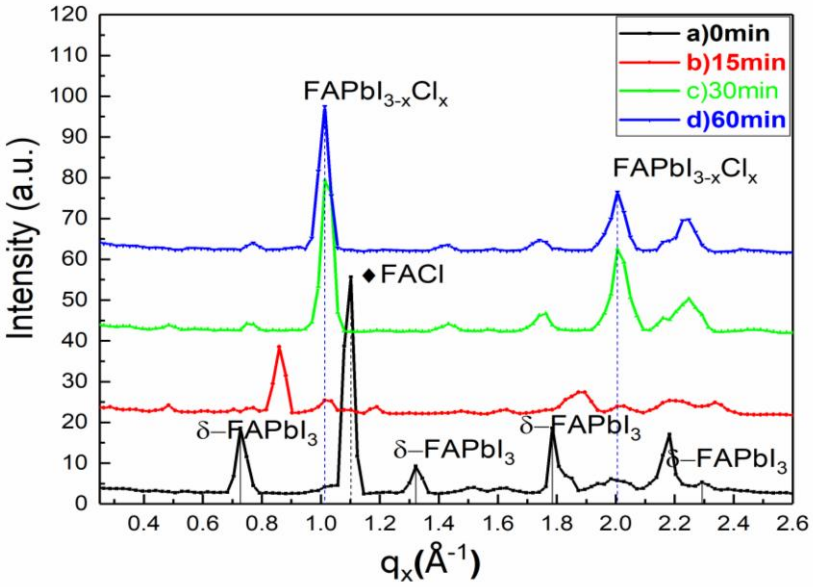

Figure 5.7: GI-WAXS patterns of $FAPbI_{3-x}Cl_X$ perovskite without annealing (a), and annealed at 170°C for 15min (b), 30min (c) and 60min (d).

5.2-2- Investigation of Surface Morphology of $FAPbI_{3-x}Cl_x$

The film of $FAPbI_{3-x}Cl_x$ perovskite before and after the thermal annealing was investigated by SEM to study the effects of the heat on the surface coverage. **Fig 5.8** compares the SEM images of the surfaces of the $FAPbI_{3-x}Cl_x$ films. Before annealing, the SEM image features clearly crystalline grains most of which have an approximately hexagonal shape embedded within a more homogeneous material.

In contrast, the surface coverage has significantly increased after annealing at 190°C for 30 min. The hexagonal grains have disappeared, which might indicate that the grains have decomposed completely. The morphology of the $FAPbI_{3-x}Cl_x$ film is further affected by the annealing times which indicate the homogeneous materials eventually acquired some texture. This is indicating that there may be crystalline materials embedded within it as also indicated by GI-WAXS data results in **Fig 5.7**.

The surface of $FAPbI_{3-x}Cl_x$ film annealed at 190°C at different annealing times (15, 30 and 60 min.) is shown in **Fig 5.9 (a**, **b, c)**. The remarkable increase in the coverage of the film's surface was observed with increase annealing time, which indicates the need to anneal for more than 15 min to form a smaller number of pinhole-sized pores in the film, which is desirable for high efficiency photovoltaic devices. This fact is corroborated by the GI-WAXS data shown in **Fig 5.7**, where the lower TWAXS signals indicate poor morphology at shorter annealing time (15 minutes). The surface converge calculated at 15 min annealing is 50% whereas is 85% when the annealing time doubled and the best converge is 94% after 60 minutes of annealing.

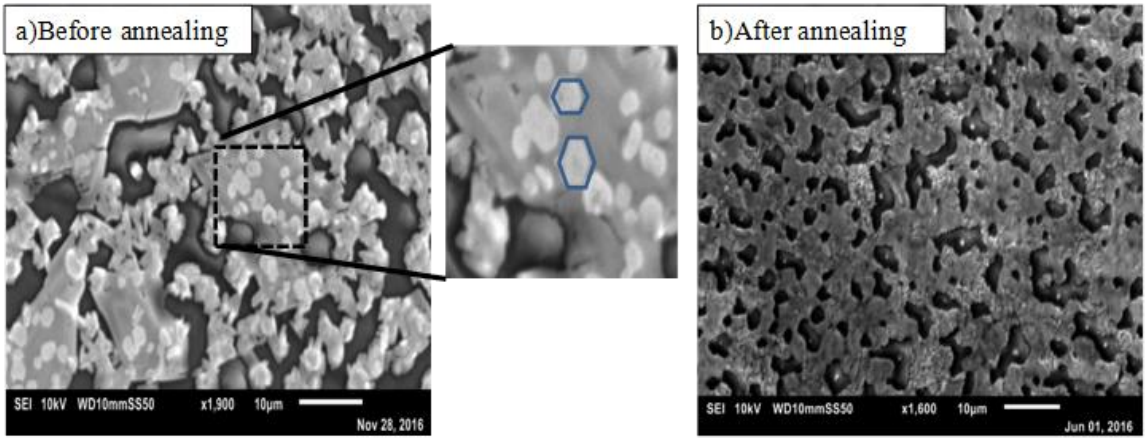

Figure 5.8: The surface of the solution is containing FAI, $PbCl_2$ and DMF solvent after spin coating, forming a wet film, the grains illustrate the hexagonal geometry, and the film after the thermal annealing is shown in (b).

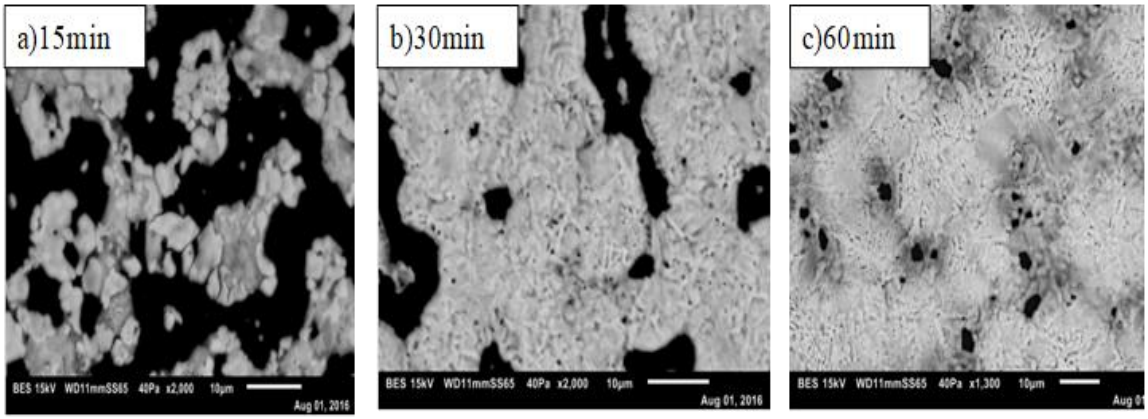

Figure 5.9 The surface of the annealed film to 170 °C for a) 15min., b) 30min. and c) 60 min

5.2-3 Changes in Perovskite Crystalline Structure of $FAPbI_{3-x}Cl_x$ Film After Thermal Annealing

The main differences between the T-WAXS profile of materials that produce the $FAPbI_{3-x}Cl_x$ film after spin coating and T-WAXS profile of the annealed $FAPbI_{3-x}Cl_x$ film is presented in **Fig 5.10 (a)**. Based on the thermal annealing condition that experimentally tested in the last section, after spin coating the film was annealed at 190^{o}C for 1 hour under ambient conditions.

After annealing, high intensity X-ray scattering peaks are observed at q=1 $Å^{-1}$and q=2.0 $Å^{-1}$. In addition, there are several weak scattering peaks between 0.8 $Å^{-1}$and 0.9 $Å^{-1}$ that are attributed to PbI_2, and the peak at 1.4 $Å^{-1}$originates from the substrate and $PbCl_2$. However, the group of scattering peaks associated to the hexagonal structure of δ-$FAPbI_3$ and the intermediate phase of FACl are no longer present.

The strong scattering peak around 0.99 A^{-1} that is assigned to perovskite phase, as reported before [4, 8]. The absence of the intermediate phase of FACl and the δ-$FAPbI_3$ phase indicate a positive role of the high temperature annealing to remove the residual or

to decompose these intermediate products. The need for this higher temperature annealing to assist the formation of $FAPbI_{3-x}Cl_x$ perovskite phase is associated with the completion of a reaction between FAI and $PbCl_2$, which thus forms a tetragonal structure of $FAPbI_{3-x}Cl_x$. However, there is a little evidence of initial crystallisation of $FAPbI_{3-x}Cl_x$ during the spin coating, as indicated by the weak scattering in the T-WAXS profile of a sample before annealing, as shown in **Fig 5.1(a)**, observed with the peak at q=0.99 $Å^{-1}$.

Fig 5.10 (b) illustrates the difference in 2D T-WAXS image collected before and after the thermal annealing of $FAPbI_{3-x}Cl_x$ film. Before annealing, groups of X-ray scattering rings can be seen with different degree of the intensity, that indicate the presence of δ-$FAPI_3$, at q=0.7 $Å^{-1}$ and at q=1.3 $Å^{-1}$, $FAPbI_{3-x}Cl_x$ at q=0.99 $Å^{-1}$ and FACl at q=1.1 $Å^{-1}$.

The high intense continuous X-ray scattering ring of the random order of orientation of δ-$FAPI_3$ at q=0.7 $Å^{-1}$ whereas the bright spots in the ring are caused by single larger crystals. This indicates that this is the dominant phase before the annealing process, whereas, the remarkable absence of the phase is noticed after annealing indicating thermal instability of this phase.

A weak scattering ring with irregular distribution of intensity around the ring of the perovskite phase that is observed at q=0.99 $Å^{-1}$ is present before annealing, and this confirms that some small amount of individual crystals of the perovskite have already formed during the spin coating stage.

The more uniform distribution of intensity around the ring at q=0.99 $Å^{-1}$ that attributed to $FAPbI_{3-x}Cl_x$ after annealing indicates that the crystals formed and randomly oriented.

The uniform distribution of intensity around the scattering ring associated with the FACl crystallites observed at q=1.1 $Å^{-1}$ indicates that they exhibit a high degree of random orientation and there are many crystallites present due to the high degree of T-WAXS intensity before annealing. This large presence of FACl requires high temperature to be removed, as was observed from 2D-TWAXS data in the left in **Fig 5.10 (b)**.

The feature at q=1.4 $Å^{-1}$ is remarkably reduced, showing only bright spots in 2D-TWAXS data after annealing that most likely correspond to large crystal of un-reacted $PbCl_2$.

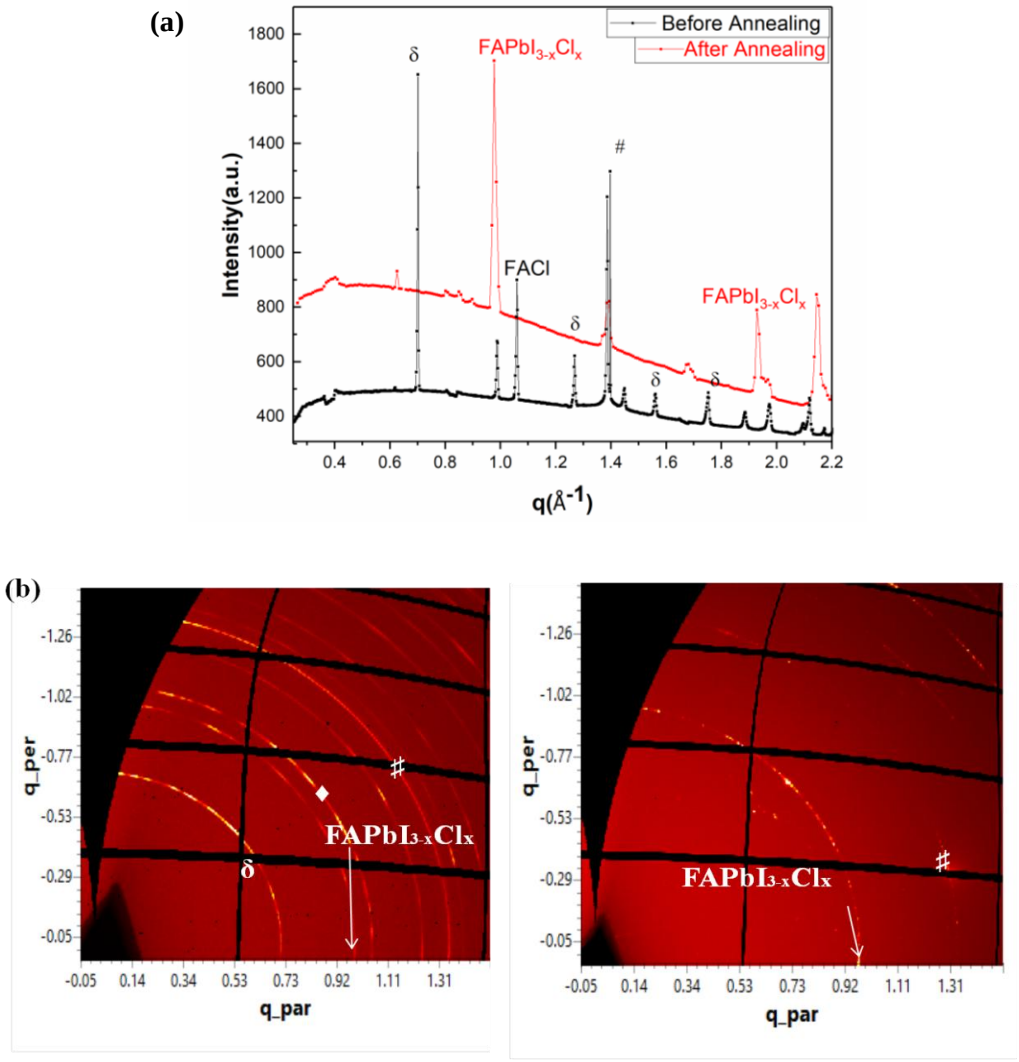

Figure 5.10: (a) The differences between T-WAXS profiles of the structure of $FAPbI_{3-x}Cl_x$ before and after thermal annealing. The 2D data T-WAXS provides the orientation of the crystalline structure of solution that makes (b) $FAPbI_{3-x}Cl_x$ before in (left) and after annealing in (right).

5.2-4 Degradation Study of $FAPbI_{3-x}Cl_x$ Film by T-WAXS

The degradation of the $FAPbI_{3-x}Cl_x$ film was studied by T-WAXS. Prior to the degradation study, a film was formed under ambient conditions and was annealed to 190^{o}C for one hour to form $FAPbI_{3-x}Cl_x$. It was placed inside the sample chamber which

was flushed with helium. T-WAXS images were collected using 5s exposures every 10 minutes for 9 hours to investigate the stability of the un-encapsulated $FAPbI_{3-x}Cl_x$ film.

Fig5.11 (a) plots the time dependent T-WAXS patterns during the degradation of the $FAPbI_{3-x}Cl_x$ film. Due to material degradation, the main observation is the gradual change in the T-WAXS intensity at the perovskite phase at q=0.99 $Å^{-1}$ from the higher intensity at the beginning of the measurement to the lower intensity at the end of measurement. This degradation also resulted in a growth in the peak intensity of the T-WAXS feature at 0.63Å that is defined as the background scattering from a complex that contains solvents in **Fig 5.1**. Furthermore, there is a slight increase in 0.86 $Å^{-1}$ that is closer value to 0.9 $Å^{-1}$ scattering feature of the lead as reported before [2, 9].

In **Fig 5.11(b)** the normalized intensity of three peaks that make difference in the T.WAXS pattern after 9 hours is plotted as a function of the time (min). The data suggests that the un-capsulated $FAPbI_{3-x}Cl_x$ film can be used for 5 hours (300min) before being decomposed into the lead and solvent contents which indicate that the preferable thermal stability of the annealed $FAPbI_{3-x}Cl_x$ film.

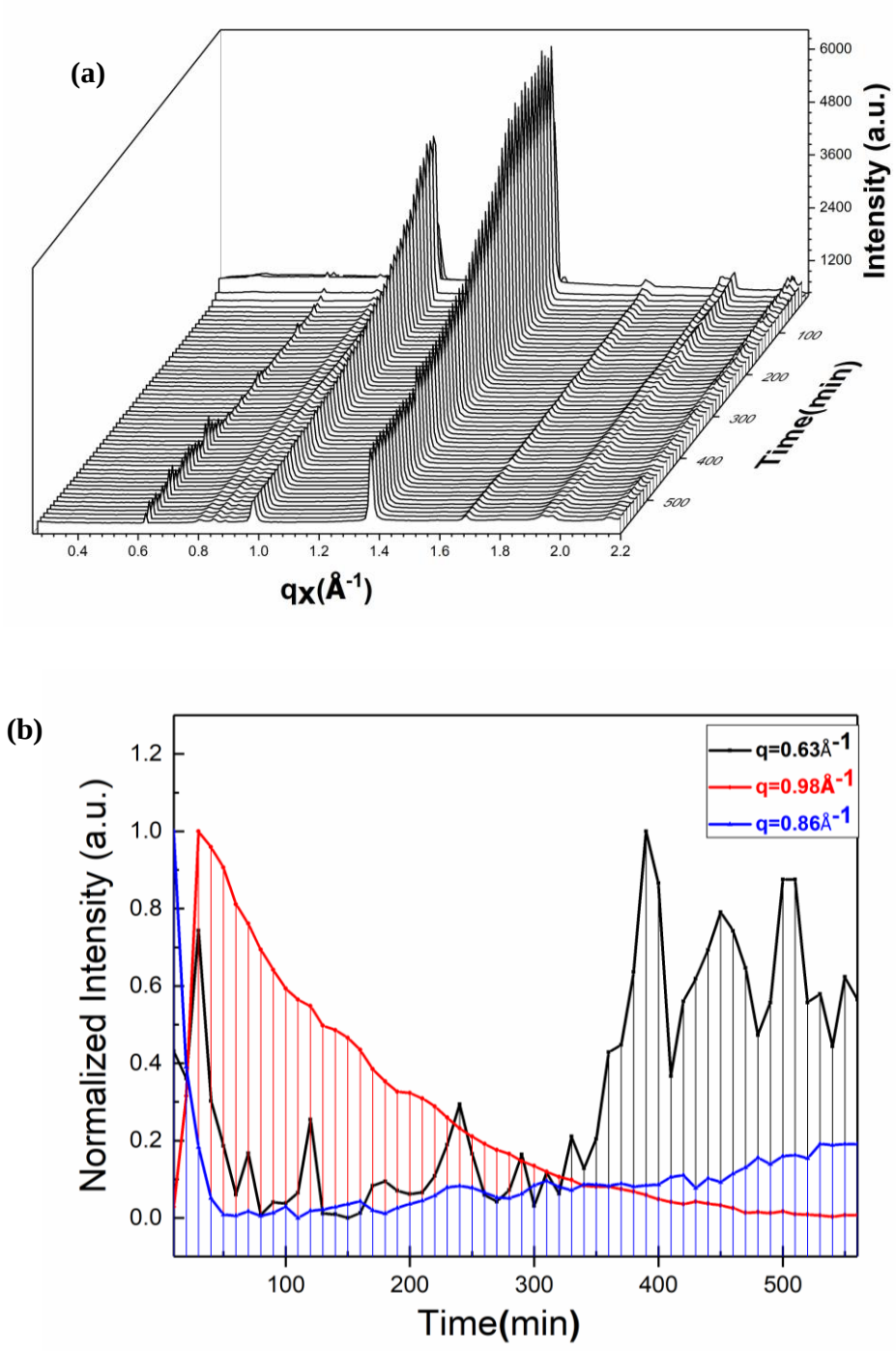

Figure 5.11: Time dependent T-WAXS profiles of an annealed $FAPbI_{3-x}Cl_x$ film over min.(a), and as a function of time over several hours of X-ray exposure (b).

5.3 Light Absorption Spectra of $FAPbI_{3-x}Cl_x$ Film

The UV-Vis absorption spectra of the $FAPbI_{3-x}Cl_x$ film are presented in **Fig 5.12 (a)** as a function of annealing temperature. Three different films were annealed at 190^{o}C, 170^{o}C, and 130^{o}C for one hour in air and the visible light absorption spectra were collected several times in different locations through the films.

The absorption edge at 840 nm can be observed in the cases where the anneal temperature is $>$ 130^{o} C, whereas only a flat line is present in spectra for films annealed at 130^{o} C. This means the semiconducting behaviour of the measured films is exhibited only at higher temperature than 130^{o}C. In the same manner, the GI-WAXS data illustrated in **Fig 5.6** in **Section 5.2.2** suggest that annealing temperatures of 130^{o}C and less are not optimal to form the preferable highly crystalline homogenous perovskite films.

The optical band gap of the $FAPbI_{3-x}Cl_x$ formed when the anneal temperature is over 130^{o} C is extracted from the light absorption spectra using the Tauc law, as detailed in **Chapter 3**. For the $FAPbI_{3-x}Cl_x$ film annealed at 190^{o}C for one hour, the optical band gap is evaluated by a linear fit at nearly 1.49 eV, a similar value to that reported in [4]. This value of the optical band gap of $FAPbI_{3-x}Cl_x$ is closer to the theoretical optimum band gap of 1.3 eV for solar cell applications, as discussed in **Chapter 1,** than the one for a $MAPbI_{3-x}Cl_x$ film, which is estimated to be 1.55 eV, as reported in the **Chapter 4**.

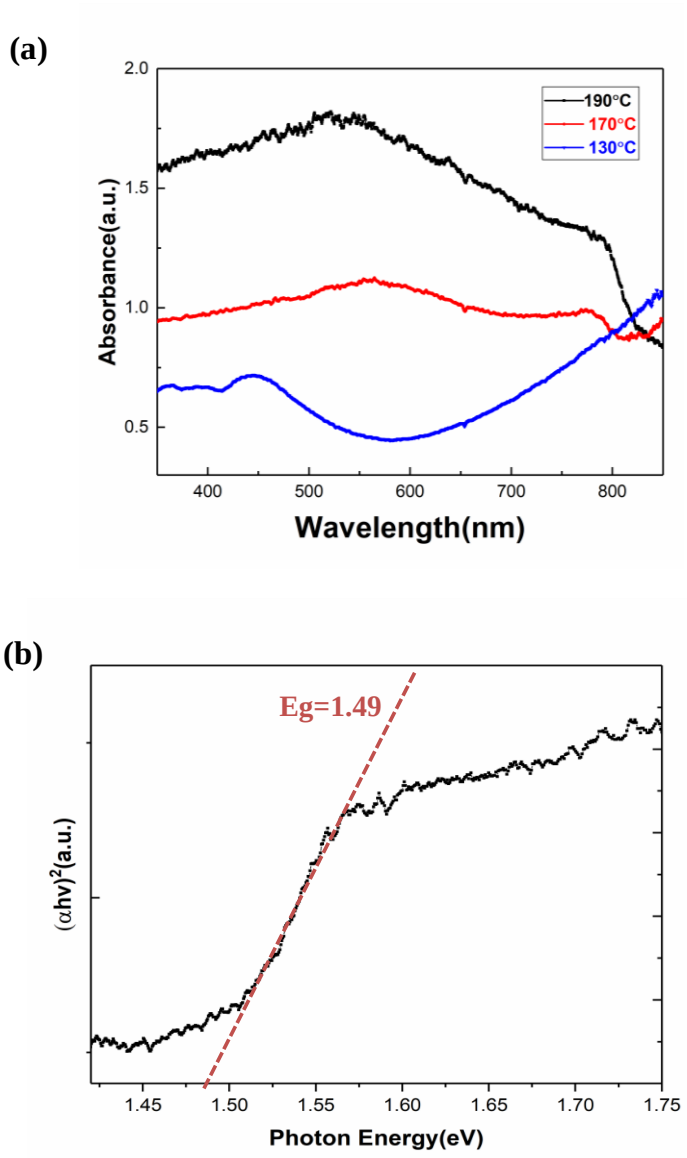

Figure 5.12: UV-Vis spectra of the $FAPbI_{3-x}Cl_x$ film as function of temperature (a) and the optical band gap extracted using Tauc law (b).

5.4 Conclusion

In this chapter the crystals forming of the $FAPbI_{3-X}Cl_X$ perovskite studied *in situ* during spin coating was presented, to best of our knowledge for the first time. The hexagonal structure of δ-$FAPbI_3$ and FACl are the main intermediate products formed directly during the spin coating before fully converting into the perovskite phase that formed at the third stage of crystals forming mechanism.

The T-WAXS experiments reveal that these intermediate products are completely removed or decompose after thermal annealing and a preferable pure tetragonal structure which is more thermodynamically stable is formed. However, an anneal temperature higher than 130^{o}C and duration longer than 15 min is required to convert the intermediate products fully into the perovskite, as ascertained from GI-WAXS experiments.

The direct observation of the formation of crystalline structures during the spin coating process has allowed a deeper understanding of the materials present in the as cast films before annealing to produce the perovskite film. The relative rates at which these conversions occur have been observed. From the annealing study it is clear that carefully selecting the annealing parameters is crucial to form high quality crystals in the desired morphology for the photoactive films, thereby potentially leading to higher PCE solar cell devices based on $FAPbI_{3-x}Cl_x$ materials. Furthermore, since a greater range of photon energies can be absorbed by $FAPbI_{3-x}Cl_x$ materials compared with most common perovskite materials higher current density generation is expected for $FAPbI_{3-x}Cl_x$ materials, as was suggested from the light absorption spectra and the optical band gap.

5.5 References

1. Chen, S., B. Chen, X. Gao, B. Dong, H. Hu, K. Yan, W. Wen, and D. Zou, Neutral-colored semitransparent solar cells based on pseudohalide (SCN−)-doped perovskite. Sustainable Energy & Fuels, 2017.
2. Numata, Y., Y. Sanehira, and T. Miyasaka, Impacts of Heterogeneous TiO2 and Al2O3 Composite Mesoporous Scaffold on Formamidinium Lead Trihalide Perovskite Solar Cells. ACS applied materials & interfaces, 2016. 8(7): p. 4608-4615.
3. Stoumpos, C.C., C.D. Malliakas, and M.G. Kanatzidis, Semiconducting tin and lead iodide perovskites with organic cations: phase transitions, high mobilities, and near-infrared photoluminescent properties. Inorganic chemistry, 2013. 52(15): p. 9019-9038.
4. Lv, S., S. Pang, Y. Zhou, N.P. Padture, H. Hu, L. Wang, X. Zhou, H. Zhu, L. Zhang, and C. Huang, One-step, solution-processed formamidinium lead trihalide ($FAPbI_{(3-x)}Cl_x$) for mesoscopic perovskite–polymer solar cells. Physical Chemistry Chemical Physics, 2014. 16(36): p. 19206-19211.
5. Aguiar, J.A., S. Wozny, T.G. Holesinger, T. Aoki, M.K. Patel, M. Yang, J.J. Berry, M. Al-Jassim, W. Zhou, and K. Zhu, In situ investigation of the formation and metastability of formamidinium lead tri-iodide perovskite solar cells. Energy & Environmental Science, 2016. 9(7): p. 2372-2382.
6. Lilliu, S., T. Agostinelli, E. Pires, M. Hampton, J. Nelson, and J.E. Macdonald, Dynamics of crystallization and disorder during annealing of P3HT/PCBM bulk heterojunctions. Macromolecules, 2011. 44(8): p. 2725-2734.
7. Renaud, G., R. Lazzari, and F. Leroy, Probing surface and interface morphology with grazing incidence small angle X-ray scattering. Surface Science Reports, 2009. 64(8): p. 255-380.
8. Yuan, D.-X., A. Gorka, M.-F. Xu, Z.-K. Wang, and L.-S. Liao, Inverted planar NH 2 CH [double bond, length as m-dash] NH 2 PbI 3 perovskite solar cells with 13.56% efficiency via low temperature processing. Physical Chemistry Chemical Physics, 2015. 17(30): p. 19745-19750.

9. Pool, V.L., B. Dou, D.G. Van Campen, T.R. Klein-Stockert, F.S. Barnes, S.E. Shaheen, M.I. Ahmad, M.F. Van Hest, and M.F. Toney, Thermal engineering of FAPbI3 perovskite material via radiative thermal annealing and in situ XRD. Nature Communications, 2017. 8.

Chapter 6: Crystal formation of Lead Free Materials Related to Perovskite Based on $A_3Bi_2I_9/A_3Bi_2I_9Cl_x$

The previous chapters discussed the dynamics of the crystallisation mechanisms of $MAPbI_{3-x}Cl_x$ and $FAPbI_{3-x}Cl_x$ films containing highly toxic lead compounds. In this chapter, lead free materials related to perovskite are characterised, proposing a new class of low toxicity photoactive materials. The primary focus is on replacing lead (Pb) with bismuth (Bi). In **Section 6.1** we discuss the crystallization of MAI cation materials when mixed with $BiCl_3$ to form $MA_3Bi_2I_9Cl_x$ in **Section 6.1.1.** The crystallization of $MA_3Bi_2I_9$ will be discussed in **Section 6.1.2**. In **Section 6.2** we replace MAI with FAI, to form $FA_3Bi_2I_9$ and their crystallization will be characterised.

6.1-Lead Free Materials based on Methylamine Iodide (MAI)

Unlike the ideal perovskite structure presented by ABX_3, halide bismuth perovskites have the chemical structure of $A_3Bi_2X_9$. The octahedral metal halide BX_6 in ABX_3 perovskite is replaced by bi-octahedral $(Bi_2I_9)^{3-}$ resulting in an $A_3Bi_2X_9$ perovskite [1].

6.1.1 Characterization of Methylammonium Bismuth Chloride ($MA_3Bi_2I_9Cl_x$) Materials

The discussion here will focus on three aspects of film characterisation: the crystalline structure, the morphology of the film, and the absorption spectra to determine the optical band gap. The structural properties of the materials were observed during spin coating and after thermal annealing to build sufficient understanding of the crystallised product.

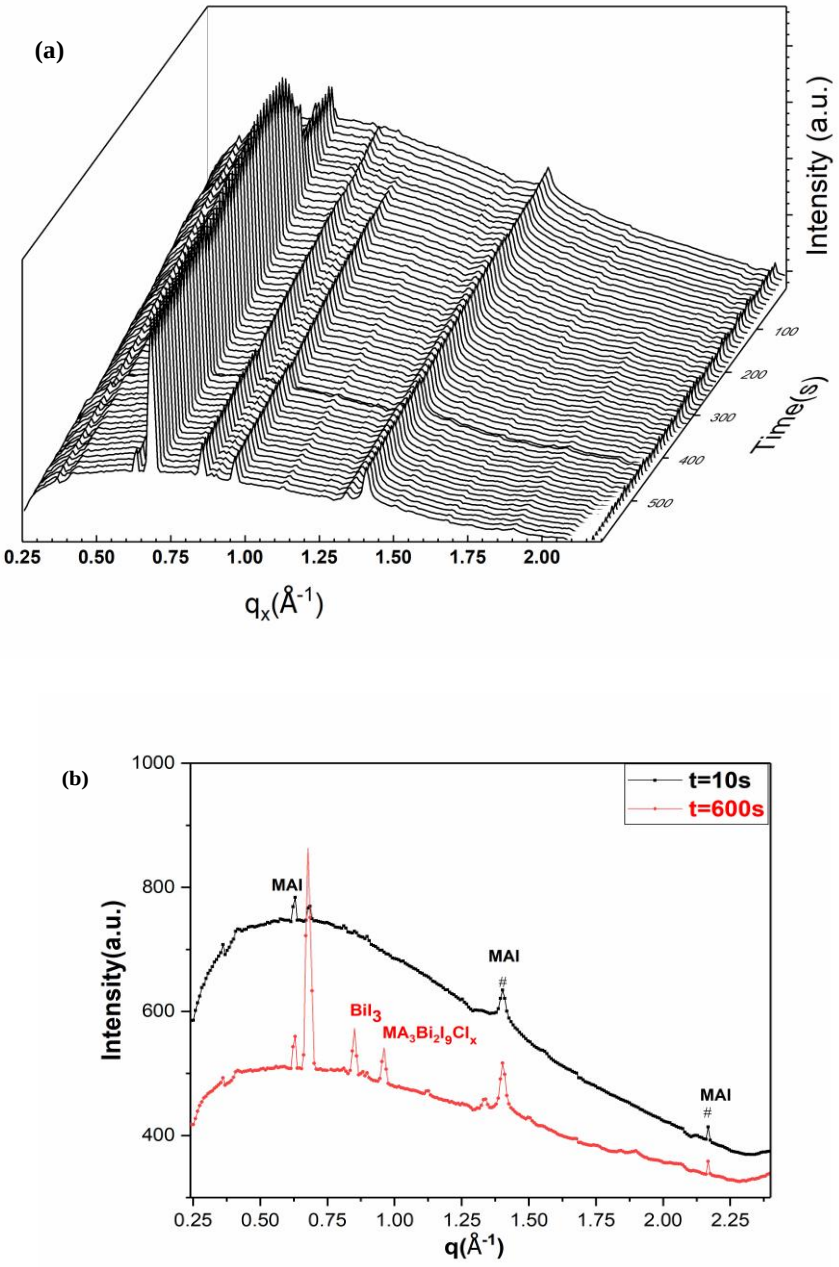

Figure 6.1: T-WAXS patterns of the solution containing MAI + $BiCl_3$ + DMF solvent proceeding $MA_3Bi_2I_9Cl_x$ measured during spin coating as a function of the time (a), the T-WAXS of films made from the same solution measured at the start and the end of the measurements with defined scattering peaks (b).

Fig 6.1(a) shows the time dependent T-WAXS pattern of a mixture of MAI and $BiCl_3$ dissolved in DMF forming $MA_3Bi_2I_9Cl_x$ formation over ten minutes. We following the formulation proceeded reported in [1], to produce $MA_3Bi_2I_9Cl_x$.

The general trend is dominated by intense X-ray scattering at q=0.7Å^{-1}and some features at q=0.62Å^{-1} q=0.86Å^{-1} and q=0.96Å^{-1} that form as illustrated in **Fig 6.1 (b).**

The features at q=0.62Å^{-1}, q=1.4Å^{-1} and around q=2.15Å^{-1} are attributed to the content of MAI, in agreement the investigation of the crystal structure of MAI, as reported previously[2]. The mica substrate also shows scattering around q=1.4Å^{-1} and 2.15Å^{-1} as indicated in **Chapter 4.**

The X-ray diffraction studies, using Cu Kα radiation λ=1.54Å, of the individual BiI_3 show features at 12.5^{o}, 26^{o}, 41.5^{o} as reported previously [3-5], that are equivalent to q=0.88 Å^{-1}, 1.8 Å^{-1}and 2.8 Å^{-1}, Annealed $MA_3Bi_2I_9Cl_x$ film exhibited XRD features at 12 ^{o}, 12.5 ^{o}, 25 ^{o} as was reported in[1]. The XRD features are in agreement with X-ray scattering values of 0.85 Å^{-1},0.88 Å^{-1}and 1.76Å^{-1}. Therefore, the scattering at q=0.86 Å^{-1} in **Fig 6.1** is most likely attributed to the formation of $MA_3Bi_2I_9Cl_x$.

The scattering value at 0.7 Å^{-1}is not in agreement with BiI structure or $MA_3Bi_2I_9Cl_x$ structure, therefore it is most likely corresponded to un-reacted MAI.

For further insight into the crystal structure of $MA_3Bi_2I_9Cl_x$, the data of T-WAXS patterns is plotted as a colour map of T-WAXS intensity in **Fig 6.2(a)**. Among the different sources of X-ray scattering present in the intensity map, included are the MAI, substrate, BiI_3 and $MA_3Bi_2I_9Cl_x$. The very high intensity at q=0.67Å^{-1} reflects the large

amount of BiI_3. In contrast, the $MA_3Bi_2I_9Cl_x$ crystals are gradually formed, as indicated by the lower intensity.

However, after annealing, the T-WAXS profile possesses scattering peaks around $0.95Å^{-1}$ and $0.2Å^{-1}$that indicates the presence of $MA_3Bi_2I_9Cl_x$ crystals, as was observed from and reported in [1] **Fig 6.2(b)**.

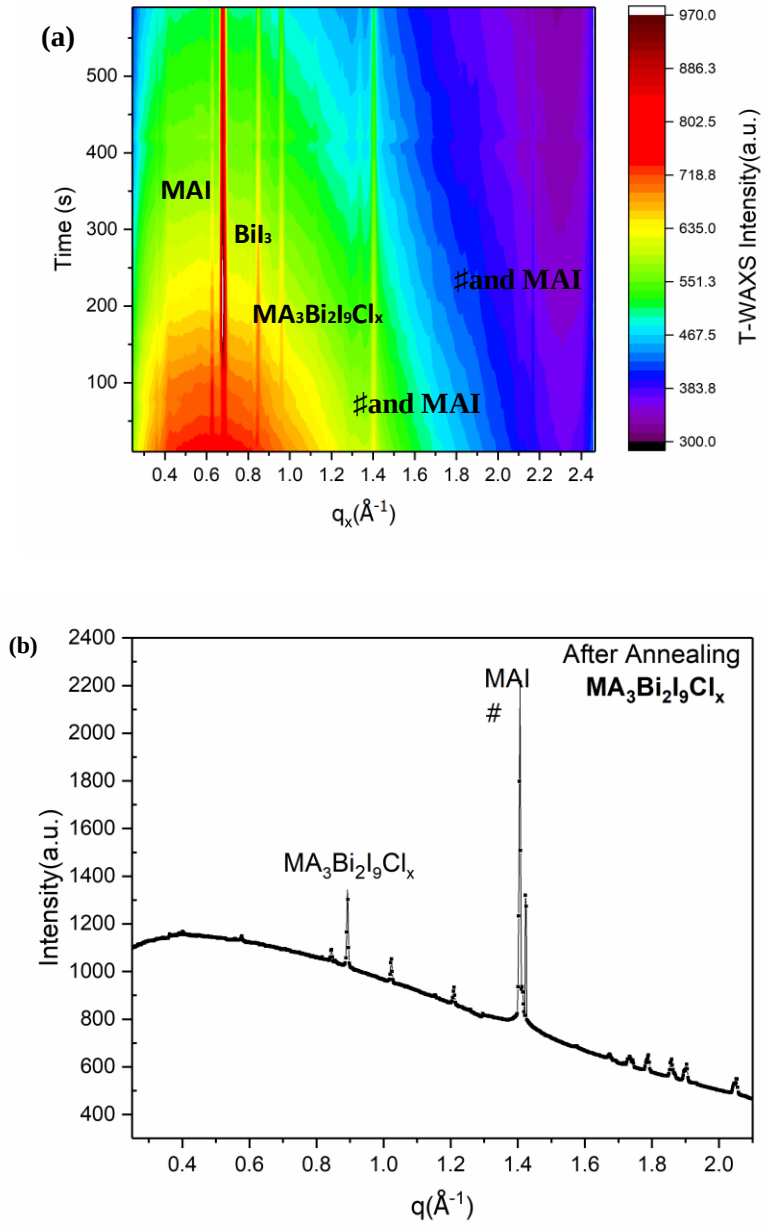

Figure 6.2: The contour plot of T-WAXS intensity showed in Fig 6.1(a) of $MA_3Bi_2I_9Cl_x$ perovskite films (a) and the main features of the T-WAXS profile after annealing (b).

The role of thermal annealing to decompose un-reacted materials and form the pure $MA_3Bi_2I_{9-x}Cl_X$ results in a perovskite with an orthorhombic structure that is similar to that reported in [6], and is corroborated by the SEM data in **Fig 6.3(a)**.

Replacing the lead chloride with bismuth chloride results in light absorption at a shorter wavelength at 600 nm, as UV-Vis spectra measurements as illustrated in **Fig 6.3(b).** The Tauc method is applied here to estimate the band gap, which was determined to be 2.05eV, which is a closer value to 2.1eV reported in previous study[7].

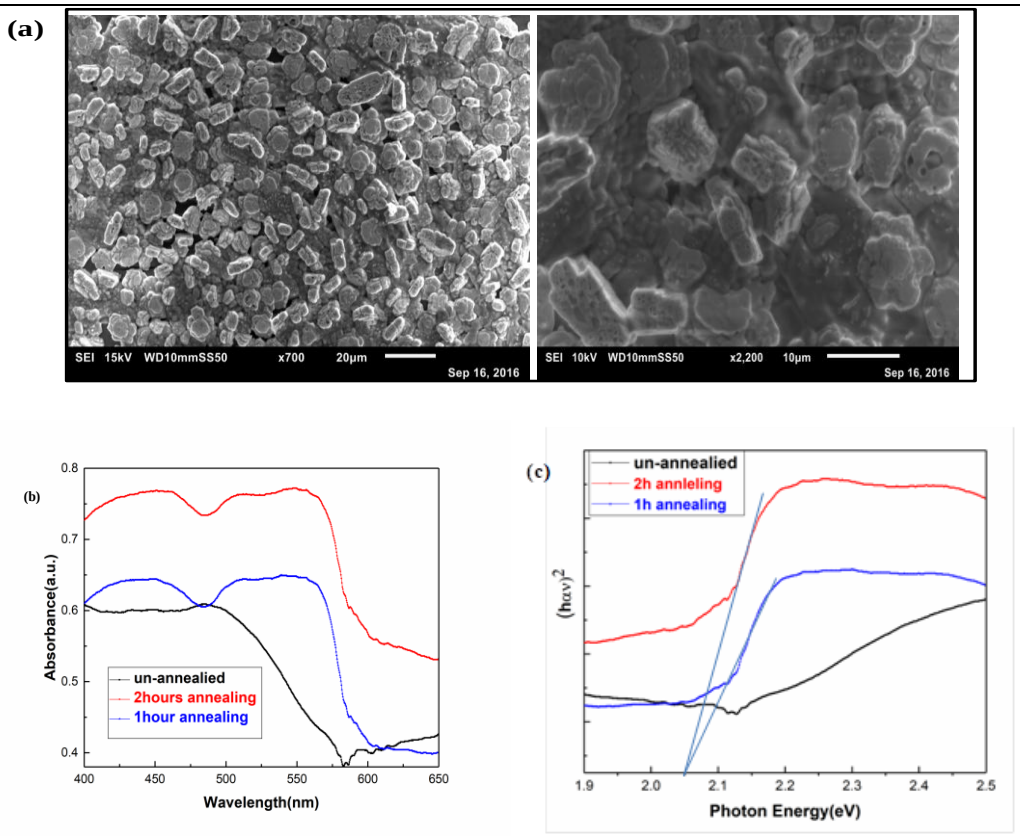

Figure 6.3: Surface of the film inspected by SEM with 20 µm on the left and 10µm on the right **(a),** the UV-Vis light absorption spectra (b) and the optical band gap extracted from Touc plot (c).

6.1.2 Characterization of Methylammonium Bismuth Iodide Materials ($MA_3Bi_2I_9$)

The mixture of MAI and BiI_3 dissolved in the same solvent DMF with 1:1 molar ratio was characterized by *in situ* spin coating T-WAXS techniques, and the results are plotted in **Fig 6.4(a).** Unlike the crystallisation mechanisms of the $MA_3Bi_2I_9Cl_x$ materials, faster and direct crystallisation of $MA_3Bi_2I_9$ is observed **(Fig 6.4(b)).**

In addition to the signs of BiI_3, MAI and the scattering from the mica substrates that was defined in the previous section, we detected X-ray scattering at around $0.85Å^{-1}$. This indicates a significant content of $MA_3Bi_2I_9$ [8, 9].

The colour of *in situ* T-WAXS intensity map of $MA_3Bi_2I_9$ as a function of the scattering vector q is illustrated in **Fig 6.5(a).** This exhibits individual colours of X-ray scattering at $q=0.85Å^{-1}$ and $q=0.88\ Å^{-1}$ from t=1 min to 10 min without any changes. This confirms the direct and fast crystallisation of $MA_3Bi_2I_9$without annealing. However, un-reacted components are still presented in particular BiI_3, as indicated by the line at $q=0.88\ Å^{-1}$ and the content of MAI as shown in the line at $q=0.6Å^{-1}$.

The role of annealing to remove the un-reacted components is less effective for $MA_3Bi_2I_9$ than for $MA_3Bi_2I_9Cl_x$, which could contribute to the existence of the MA and BiI after annealing as is observed in **Fig 6.5 (b).** This might be improved by using a higher annealing temperature or longer annealing time. The annealing condition was used is 90^oC for 120 minutes where DMF solvent was used as mentioned in the method chapter.

The T-WAXS profile of the $MA_3Bi_2I_9$ exhibits the hexagonal shaped crystals, as confirmed by SEM images in the inset image in **Fig 6.5(b)**. The poor surface coverage is observed that calculated to be only 50%.

UV-Vis spectra show light absorption at nearly 610 nm, a shorter wavelength compared to commonly used $MAPbI_{3-x}Cl_x$ perovskite. The optical band gap is 2.1eV based on the Tauc plot in **Fig 6.6(b)** which is in agreement with [10] and [1]. However, we found out that the duration of the annealing time affects the optical properties of the $MABiI_3$ where

annealing at 90°C for one hour removed the feature at 450 nm that originates from the un-reacted BiI_3 as was suggested in[5].

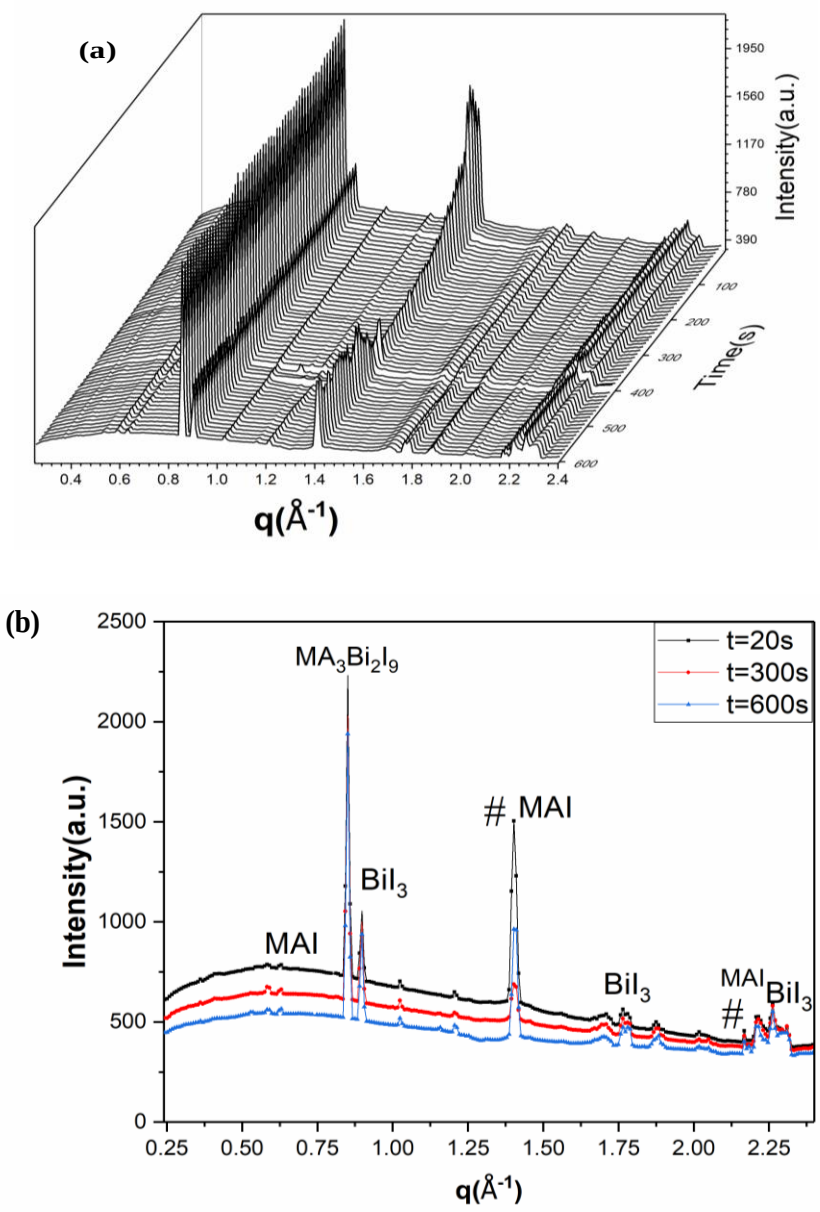

Figure 6.4: *in-situ* T-WAXS profiles of the solution preceding $MA_3Bi_2I_9$ (a) the same profiles re-plotted regarding different times (b).

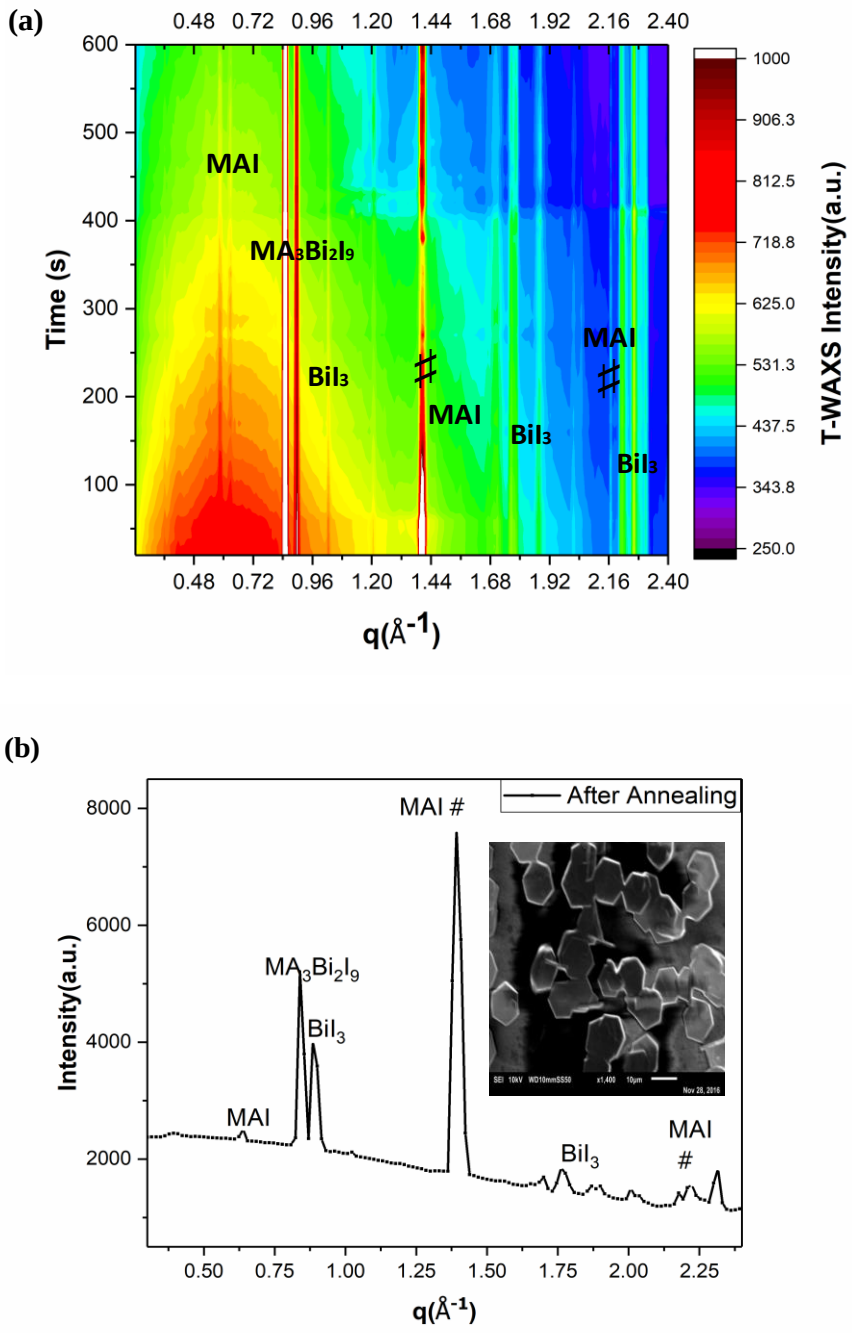

Figure 6.5: Contour plot of the intensity of X-ray scattering measured via in *in-situ* spin coating T-WAXS data of $MA_3Bi_2I_9$ (a), The T-WAXS recorded for the same measured materials which formed the annealed film (b).

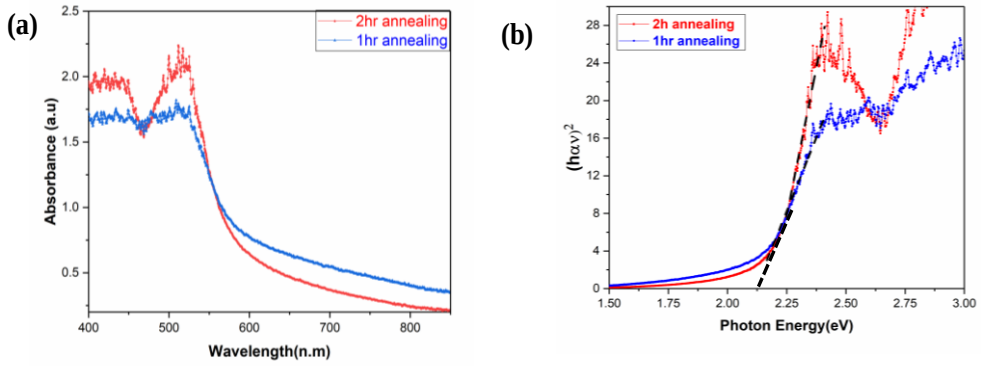

Figure 6.6: UV-Vis spectra of the $MA_3Bi_2I_9$ annealed film (a) Tauc plot to extract the optical band gap (b).

6.2 Crystal Structural and Optical Properties of $FA_3Bi_2I_9$

The effects of replacing the MA cation with an FA cation on the optical and structural properties of $FA_3Bi_2I_9$ materials are discussed for the first time in this section.

Fig 6.7 shows the results of T-WAXS of materials prepared using a one-step solution as described in **Chapter3**. The time dependent measurement of T-WAXS patterns reveals no changes in the T-WAXS features during the 10 min. measurement duration, indicating the fast and direct crystallisation of the materials **Fig 6.7 (a)**. In addition to the peaks identified as BiI_3 at around 0.88 $Å^{-1}$and 1.75 $Å^{-1}$, the high intensity T-WAXS feature at 0.835 $Å^{-1}$, as high as the BiI_3 peak at 0.88 $Å^{-1}$, is obtained during the spin coating. This scattering feature is most likely attributed to the content of the $FA_3Bi_2I_9$. Compared to the T-WAXS data of $MA_3Bi_2I_9$, the shift of the main scattering peak at q=0.85 $Å^{-1}$ into the

lower values of 0.83 $Å^{-1}$ in the $FA_3Bi_2I_9$ film is observed due to the change of the larger cation that requires a larger distance between the crystal lattice planes and thus smaller value of the q. This concept of a shift in the scattering vector to a lower value is similar to the shift in the diffraction angle that was also observed in an X-ray diffraction study of $MAPbI_3$ and $FAPbI_3$ materials [11].

After thermal annealing, the pattern of T-WAXS in **Fig 6.7(c)** exhibits peaks in the same positions before the annealing. However, the scattering peak of BiI_3 has almost disappeared and the $FA_3Bi_2I_9$ peak has grown in relative terms, which indicates conversion of most of the bismuth iodide phase into $FA_3Bi_2I_9$ phase. It should be mentioned here that the film was annealed to 190^oC for 1 hour which is different than the annealing condition that used in MA bismuth perovskite films. This condition was sufficient to remove most of the chemical residual of un-reacted BiI_3 and FAI as most of T-WAXS features disappear after annealing.

The SEM image of the $FA_3Bi_2I_9$ film after the annealing shows a hexagonal plate structure that is associated with T-WAXS profiles and good surface coverage (85%) as compared to the structure revealed in the SEM image of the $MA_3Bi_2I_9$. Based on this observation the $FA_3Bi_2I_9$ film is expected to be a more efficient absorber layer in perovskite solar cells.

For comparison, films of $FA_3Bi_2I_9$ and $MA_3Bi_2I_9$ annealed to 190°C for 1 hour and 90 °C for 2 hours, respectively, and measured by the UV-Vis spectrometer to determine the light absorption. We found that replacing the organic cation MA with FA creates a longer

wavelength absorption edge from approximately 610nm to 650nm as can be seen in **Fig 6.8(a).**

The optical band gap of the longer wavelength will be reduced from 2.1eV in $MA_3Bi_2I_9$ to 1.9 eV in $FA_3Bi_2I_9$, as extracted from Tauc plot in **Fig 6.8(b).**

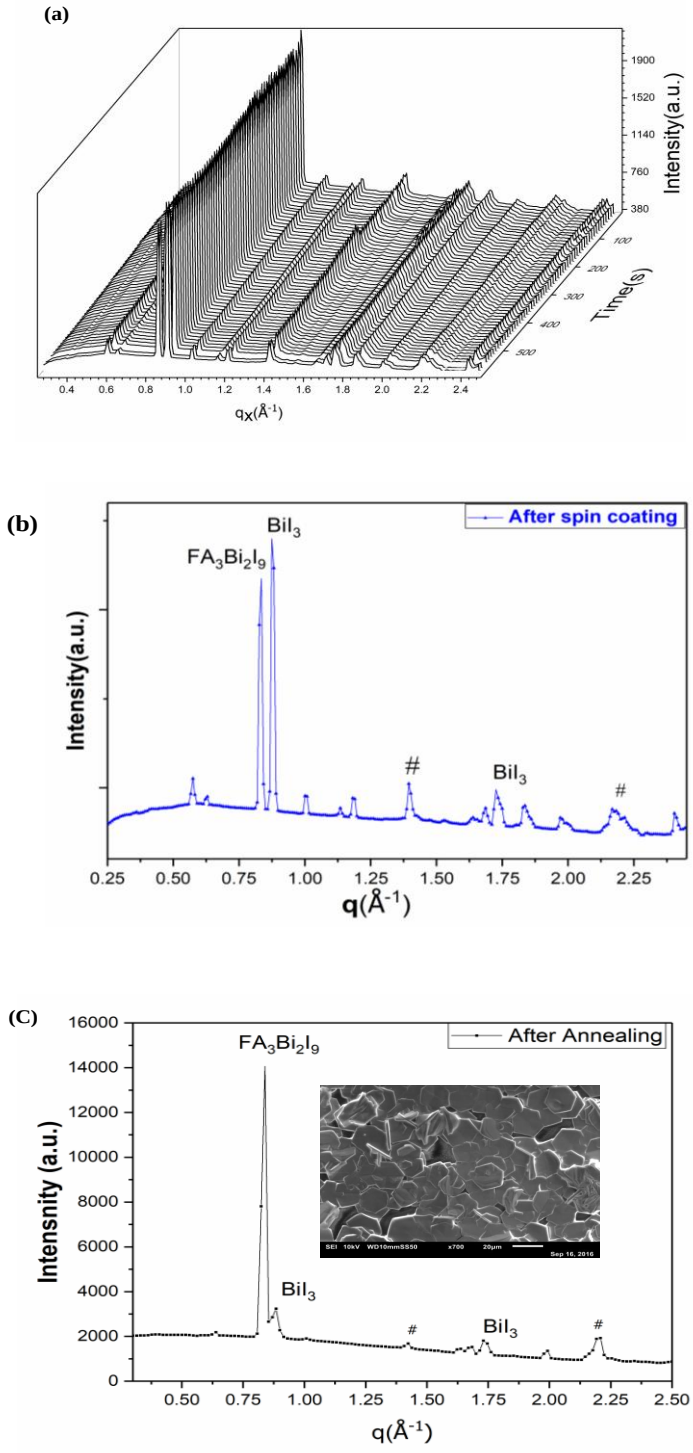

Figure 6.7: Summary of the T-WAXS data of solution proceeding $FA_3Bi_2I_9$ *in-situ* T-WAXS profiles during spin coating for 10 min (a), T-WAXS after the spin coating (b) after the thermal annealing (c).

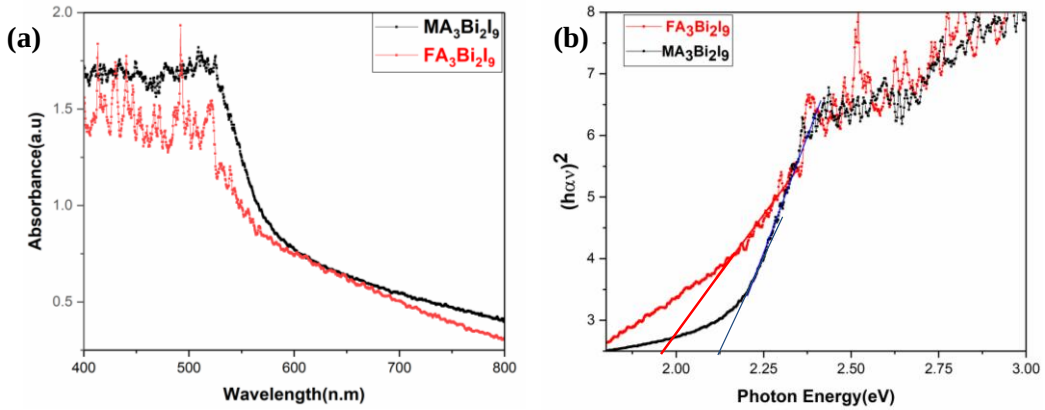

Figure 6.8: UV-Vis spectra of $FA_3Bi_2I_9$ and $MA_3Bi_2I_9$ (a) Tauc plot to determine the optical band gap.

In summary, the first direct observation of room temperature crystallization of $MA_3Bi_2I_9Cl_x$, $MA_3Bi_2I_9$ and $FA_3Bi_2I_9$ by *in situ* spin coating T-WAXS experiments has been presented here. Despite the fast and direct crystallisation of all three materials during spin coating, the significant large content of un-reacted MAI, BiI_3, FAI and $BiCl_3$ are observed. Unlike the lead perovskite materials, bismuth perovskite is distinguished by the direct crystallization within the solvent during spin casting where the final perovskite phase can form directly without the need of intermediate phase converting.

After annealing, T-WAXS profile of $MA_3Bi_2I_9Cl_X$ and $FA_3Bi_2I_9$ indicate that most of the residual components are dissolved. However, the ex-situ annealing of T-WAXS profile film of $FA_3Bi_2I_9$ shows the presence of un-reacted MAI and BiI_3 which suggested that more annealing times or higher temperature could improve the crystalline quality more.

We found that the hexagonal structure is the main structure of BiI_3 mixed with FA and MA, whereas the structure of the $BiCl_3$ with MAI has an orthorhombic structure.

The optical band gap of the materials was higher than the optimum optical band gap of solar cell materials. However, a solar cell device made from $FA_3Bi_2I_9$ is expected to give a higher PCE compared to $MA_3Bi_2I_9$, due to reducing the optical band gap, and better surface coverage as observed from SEM.

6.3 References

1. Park, B.W., B. Philippe, X. Zhang, H. Rensmo, G. Boschloo, and E.M. Johansson, Bismuth Based Hybrid Perovskites A3Bi2I9 (A: Methylammonium or Cesium) for Solar Cell Application. Advanced Materials, 2015. **27**(43): p. 6806-6813.
2. Jeon, N.J., J.H. Noh, Y.C. Kim, W.S. Yang, S. Ryu, and S.I. Seok, Solvent engineering for high-performance inorganic–organic hybrid perovskite solar cells. Nature materials, 2014. **13**(9): p. 897-903.
3. Boopathi, K.M., S. Raman, R. Mohanraman, F.-C. Chou, Y.-Y. Chen, C.-H. Lee, F.-C. Chang, and C.-W. Chu, Solution-processable bismuth iodide nanosheets as hole transport layers for organic solar cells. Solar Energy Materials and Solar Cells, 2014. **121**: p. 35-41.
4. Johansson, M.B., H. Zhu, and E.M. Johansson, Extended Photo-Conversion Spectrum in Low-Toxic Bismuth Halide Perovskite Solar Cells. The journal of physical chemistry letters, 2016. **7**(17): p. 3467-3471.
5. Ran, C., Z. Wu, J. Xi, F. Yuan, H. Dong, T. Lei, X. He, and X. Hou, Construction of Compact Methylammonium Bismuth Iodide Film Promoting Lead-Free Inverted Planar Heterojunction Organohalide Solar Cells with Open-Circuit Voltage over 0.8 V. The journal of physical chemistry letters, 2017. **8**(2): p. 394-400.
6. Szklarz, P., A. Pietraszko, R. Jakubas, G. Bator, P. Zieliński, and M. Gałazka, Structure, phase transitions and molecular dynamics of [C (NH2) 3] 3 [M2I9], M= Sb, Bi. Journal of Physics: Condensed Matter, 2008. **20**(25): p. 255221.

7. Kwak, C.K., A.T. Barrows, A.J. Pearson, D.G. Lidzey, and A.D. Dunbar, An X-ray scattering and electron microscopy study of methylammonium bismuth perovskites for solar cell applications. Journal of Materials Research, 2017. **32**(10): p. 1888-1898.
8. Abulikemu, M., S. Ould-Chikh, X. Miao, E. Alarousu, B. Murali, G.O.N. Ndjawa, J. Barbé, A. El Labban, A. Amassian, and S. Del Gobbo, Optoelectronic and photovoltaic properties of the air-stable organohalide semiconductor (CH 3 NH 3) 3 Bi 2 I 9. Journal of Materials Chemistry A, 2016. **4**(32): p. 12504-12515.
9. Eckhardt, K., V. Bon, J. Getzschmann, J. Grothe, F.M. Wisser, and S. Kaskel, Crystallographic insights into (CH 3 NH 3) 3 (Bi 2 I 9): a new lead-free hybrid organic–inorganic material as a potential absorber for photovoltaics. Chemical Communications, 2016. **52**(14): p. 3058-3060.
10. Lyu, M., J.-H. Yun, M. Cai, Y. Jiao, P.V. Bernhardt, M. Zhang, Q. Wang, A. Du, H. Wang, G. Liu, and L. Wang, Organic–inorganic bismuth (III)-based material: A lead-free, air-stable and solution-processable light-absorber beyond organolead perovskites. Nano Research, 2016. **9**(3): p. 692-702.
11. Yuan, D.-X., A. Gorka, M.-F. Xu, Z.-K. Wang, and L.-S. Liao, Inverted planar NH 2 CH [double bond, length as m-dash] NH 2 PbI 3 perovskite solar cells with 13.56% efficiency via low temperature processing. Physical Chemistry Chemical Physics, 2015. **17**(30): p. 19745-19750.

Chapter7: Conclusion

Halide perovskite materials have made considerable progress as absorber materials in solar cells devices with efficiency 22% having been reported[1]. Perovskite solar cells are distinguished by ease and lower cost of fabrication processes that are attractive criteria for their commercialization. The majority of the studies on the perovskite solar cells are focused on $MAPbI_3$ and $MAPbI_{3-x}Cl_x$ perovskite. However, some barriers related to this particular perovskite material hinder the commercialization of their solar cells, including the fast degradation causes short life times. Furthermore, the toxicity issue of perovskite that is caused by of the lead component (Pb) remains a problem. Therefore, using alternative materials is crucial to overcome these commercialization barriers. Deeper understanding of crystallization and morphological behaviour of films made from alternative perovskite materials is important to use them in solar cell devices.

Different perovskite films that are based on two material modifications were characterised. First was characterization of the formamidinium (FA) based perovskite films which substitutes for the most common organic cation methylammonium (MA) in $MAPbI_{3-x}Cl_x$. The efficiency of the perovskite solar cells based on FA are reported to be 20%[2]. However, with better understanding of the $FAPbI_{3-x}Cl_x$ film formation it may be possible to achieve further improvements. For replacement of the highly toxic materials, we investigated bismuth (Bi) perovskite materials, which is less toxic than lead. We characterized the bismuth halide perovskite films including $MA_3Bi_2I_9$, $MA_3Bi_2I_9Cl_x$ and $FA_3Bi_2I_9$.

The methods used in the thesis to understand the formation of perovskite films were *in-situ* T-WAXS, ex-situ T-WAXS, and ex-situ GI-WAXS after annealing, in addition to SEM and UV-Vis spectroscopy.

Inspection of the film during spin coating at room temperature helped track film formation after deposition, to follow the crystallization produce while the materials dried.

The results of the observation of *in-situ* spin coating T-WAXS experiments of $MAPbI_{3-x}Cl_x$ and $FAPbI_{3-x}Cl_x$ films are summarized in **Fig 7.1**.The *in-situ* T-WAXS profiles of the perovskite ink that produces $MAPbI_{3-x}Cl_x$ showed fast crystallization of the intermediate product $MA_{x+y}PbI_{2+x}Cl_y$ after 2 minutes of processing. However, complete phase of perovskite requires heating for 2 hours at 100^oC to complete the reaction between the PbCl and MAI. In contrast, the slower crystallization of the intermediate products δ-$FAPbI_3$ were observed in solution and preceded $FAPbI_{3-X}Cl_X$ as was explained in **Chapter 5.** Besides δ-$FAPbI_3$, the FACl intermediate product formed after the solvent loss at a later time of more than 400s. The most notable observation for this solution was the direct crystallization of the complete perovskite phase $FAPbI_{3-X}Cl_X$ at $q=1Å^{-1}$ and $q=2Å^{-1}$ after two minutes from the start of processing. This coincided with the formation of FACl.

The bismuth halide perovskite structure was directly crystallized in the solution stage as was suggested by the variation time with intensity of TWAXS of $MA_3Bi_2I_9Cl_x$ $MA_3Bi_2I_9$, $FA_3Bi_2I_9$ and indicated in **Fig 6.1**, **Fig 6.4**and **Fig 6.7** in **Chapter 6**.

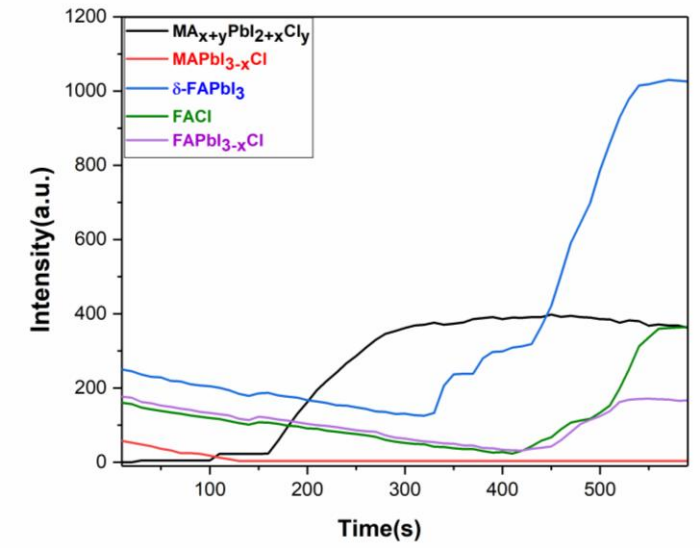

Figure7.1: Summary of time variation of crystallization of inks producing $MAPbI_{3-x}Cl_x$,$MA_{x+y}PbI_{2+x}Cl_y$, δ-$FAPbI_3$ FACl and $FAPbI_{3-x}Cl_x$ during the spin coating.

After thermal annealing, the ex-situ T-WAXS data (**Fig 7.2)** showed the similarity between the $FAPbI_{3-x}Cl_x$ and $MAPbI_{3-x}Cl_x$ perovskite structure, in which both presented the tetragonal structure with peaks at q=1$Å^{-1}$ and 2$Å^{-1}$. The slight change in $FAPbI_{3-x}Cl_x$ film at q=0.98$Å^{-1}$ from the q=1$Å^{-1}$ is attributed to the larger size of FA=0.19Å compared to 0.18Å as was illustrated in **Chapter 2,** which requires a greater distance to fit the space between molecular, thereby causing the slight decrease in q. This slight similarity was also observed in the T-WAXS pattern of the $FA_3Bi_2I_9$ film and $MA_3Bi_2I_9$ where both presented the hexagonal structure at q= 0.84$Å^{-1}$ and 0.85$Å^{-1}$.

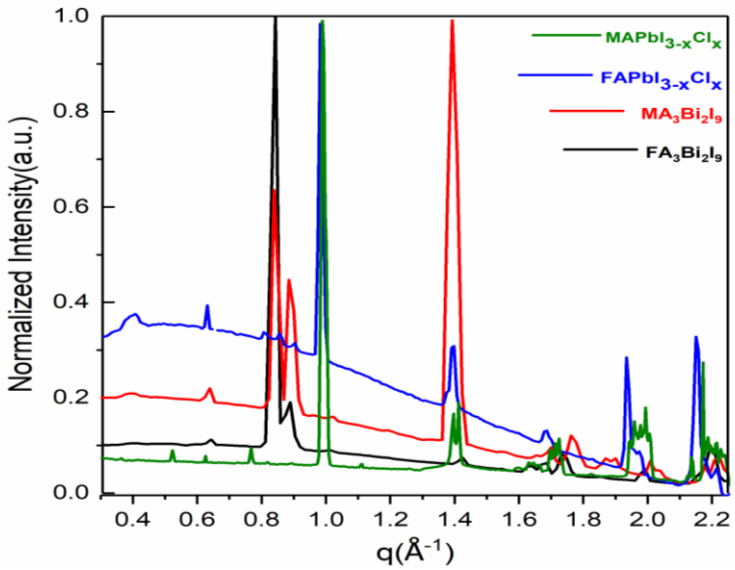

Figure7.2: T-WAXS radial profile of the annealed films of Pb- based perovskite and Bi perovskite.

The $FAPbI_{3-x}Cl_x$ perovskite film was annealed at 190^{o}C for an hour as the crystallization quality of the film was tested by ex-situ GI-WAXS. The data of ex-situ GI-WAXS revealed that the temperature of more than 170^{o}C and annealing time of more than 15 minutes is the optimal condition to form pure a perovskite phase as indicated by strength of the perovskite peaks relative to the other peaks in the T-WAXS data. These results are associated to the morphology inspection of the film surface, which showed the better surface coverage at higher temperature. The T-WAXS radial profile of the annealed $FAPbI_{3-x}Cl_x$ film was measured for more than 9 hours **Fig 5.10** in **Chapter 5**.There is no significant degradation for the first 5 hours, meaning that there is a reasonable window of time in which to prepare and encapsulate these materials before they degrade. This result is considered another promising feature of $FAPbI_{3-x}Cl_x$ film.

The surfaces of all perovskite films were investigated by the SEM to inspect the shape of the crystals and the surface coverage of the films. The image is shown with 20 µm scale

in **Fig 7.3.** The films of $FA_3Bi_2I_9$ perovskite and $MA_3Bi_2I_9$ films showed a similar hexagonal shape with better surface coverage in $FA_3Bi_2I_9$ at 85% compared to 50% for $MA_3Bi_2I_9$. The films of $MA_3Bi_2I_9Cl_x$ showed a different, orthorhombic shape of the crystals and 75% coverage. Lead chloride perovskite materials showed 60% for $MAPbI_{3-x}Cl_x$ and 55% $FAPbI_{3-x}Cl_x$.

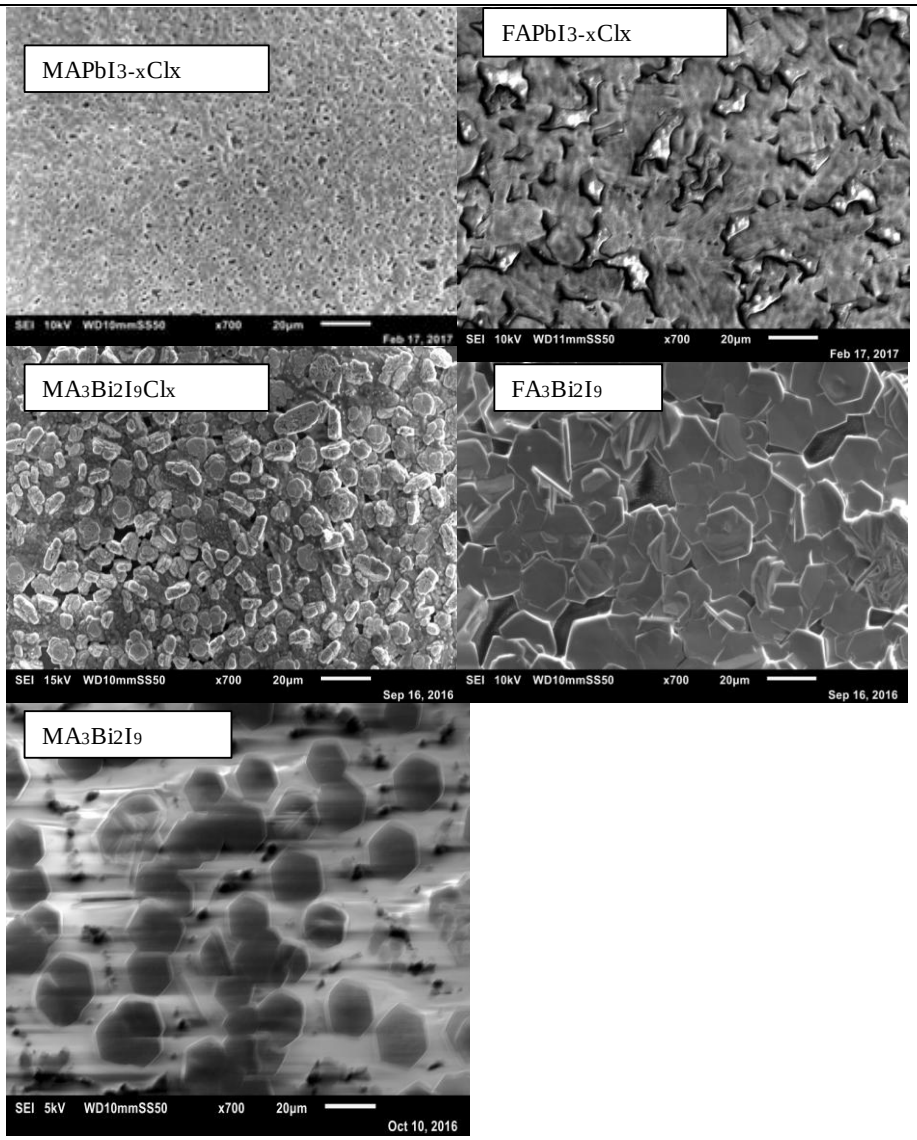

Figure7.3: SEM images of the perovskite film where the scale bar is 20 µm

The light absorption of the perovskite materials was investigated in this project, where each film exhibited different spectra. Among all perovskite films, the wider spectra of the light absorption were observed for $FAPbI_{3-x}Cl_x$ (840nm) film, suggesting that the most promising absorber is obtained by the combination the organic cation FAI and $PbCl_2$. In contrast, $MA_3Bi_2I_9$ and $MA_3Bi_2I_9Cl_x$ films showed shorter light absorption maxim (610nm, 600nm).

In this thesis we contributed to overcoming this issue by, for the first time, using the combination of the FA as larger cation size and the BiI_3. This modification causes wider light absorption spectra at 650nm of $FA_3Bi_2I_9$. Furthermore, the better surface coverage obtained as was seen in SEM images.

The band gaps were extracted from each material, and as listed in **Table 7.1** for comparison. The Lead chloride perovskite has a closer band gap to the optimum band gap in solar cell over just of 1.3eV. The bismuth perovskite, whereas, showed larger E_g reaching 2.11eV, 2.05eV and 1.9eV in $MA_3Bi_2I_9$, $MA_3Bi_2I_9Cl_x$ and $FA_3Bi_2I_9$ respectively.

Perovskite Materials	**Optical Band gap (eV)**
$MAPbI_{3-x}Cl_x$	1.5
$FAPbI_{3-x}Cl_x$	1.48
$MA_3Bi_2I_9$	2.11
$FA_3Bi_2I_9$	1.9
$MA_3Bi_2I_9Cl_x$	2.05

Table 7.1: Summary of the band gap of perovskite materials measured in this project.

Future work for this project can be divided into several directions based on the related data. First, the optical band gap measurements of the perovskite materials suggest that using lead chloride could be more suitable for single junction perovskite solar cells; whereas, the larger band gap of the Bi perovskite materials will be more suitable for use in the tandem solar cell, where the solar spectrum can be extended by larger band gap absorber materials.

Further work related to the *in-situ* T-WAS measurement of $MA_3Bi_2I_9$ in **Chapter 6** suggests that thermal annealing can be further investigated to address the issue of the solubility, and this can also be addressed by changing the solvent. In situ thermal annealing can help to define the most suitable temperature and the annealing time to form a pure $MA_3Bi_2I_9$ phase and improve surface coverage only 55%.

In terms of the investigation of the perovskite films of $FA_3Bi_2I_9$, the results suggest that making $FA_3Bi_2I_9$ solar cells device would be more efficient than MA materials. Because of the better surface coverage that observed in $FA_3Bi_2I_9$ and wider absorption spectra where Eg 1.9eV.

Both data in **Chapter 4** and **Chapter 5** can be suggesting that using these materials in the fabrication of solar cell devices as an individual absorber layer in single solar cells or both layers together in tandem solar cells is feasible.

In summary, the thesis has presented an experimental study of dynamic crystallisation during the spin coating of different ranges of perovskite, including different organic cation A; formamidinium (FA) and methylammonium (MA); lead perovskite, and free lead perovskite. For comparison purposes, annealed films of the same materials were

measured using the same technique. Furthermore, a morphological study and light absorption measurements for all perovskite materials have been discussed in this thesis.

The findings of the research are summarised in the following points: First, the faster crystallization of the intermediate product of $MA_{x+y}PbI_{2+x}Cl_y$ was observed, whereas the intermediate products of FACl and δ-$FAPbI_3$ took longer.

The complete perovskite phase of $FAPbI_{3-x}Cl_x$, on the other hand, formed faster before annealing, and after 15 min annealing, most of the intermediate products were removed. In contrast, in order to remove the intermediate product $MA_{x+y}PbI_{2+x}Cl_y$ 2hours were needed for it to decompose into the complete perovskite phase. This indicates the preferable stability feature of perovskite in the case of MA being replaced by FA. Besides that, the band gap reduces in $FAPbI_{3-x}Cl_x$ (1.48eV) to absorb more photons than in $MAPbI_{3-x}Cl_x$ (1.5eV).

Finally, the data related to lead free, based on bismuth perovskite, showed a hexagonal structure different to the tetragonal structure in lead perovskite materials. The band gap measurement showed a higher band gap compared to lead perovskite. However, the FA free lead perovskite materials showed a reduction in band gap and better surface converge compared to MA free lead perovskite. The data suggests that FA cation can be used as preferable organic cation to modify lead free perovskite.

References

1. NERL, https://www.nrel.gov/ncpv/images/efficiency_chart.jpg. 2017.
2. Yang, W.S., J.H. Noh, N.J. Jeon, Y.C. Kim, S. Ryu, J. Seo, and S.I. Seok, High-performance photovoltaic perovskite layers fabricated through intramolecular exchange. Science, 2015. **348**(6240): p. 1234-1237.